

Effects of 3D Ideal MHD Equilibrium Geometry on Neoclassical Properties in Tokamaks: Exploring Bootstrap Current and Impurity Accumulation

THÈSE N° 8078 (2018)

PRÉSENTÉE LE 26 JANVIER 2018
À LA FACULTÉ DES SCIENCES DE BASE
SPC - THÉORIE
PROGRAMME DOCTORAL EN PHYSIQUE

ÉCOLE POLYTECHNIQUE FÉDÉRALE DE LAUSANNE

POUR L'OBTENTION DU GRADE DE DOCTEUR ÈS SCIENCES

PAR

Madhusudan RAGHUNATHAN

acceptée sur proposition du jury:

Prof. V. Savona, président du jury
Dr J. Graves, Dr W. A. Cooper, directeurs de thèse
Dr X. Garbet, rapporteur
Dr C. Ham, rapporteur
Dr B. Duval, rapporteur



ÉCOLE POLYTECHNIQUE
FÉDÉRALE DE LAUSANNE

Suisse
2018

All we have to believe with is our senses, the tools we use to perceive the world: our sight, our touch, our memory. If they lie to us, then nothing can be trusted. And even if we do not believe, then still we cannot travel in any other way than the road our senses show us; and we must walk that road to the end.

American Gods, Neil Gaiman

Abstract

This thesis concentrates on investigating the presence of 3D ideal MHD instabilities, particularly a saturated 1/1 ideal internal kink, on neoclassical phenomena such as the bootstrap current and heavy impurity transport. The MHD equilibria are generated using the ideal MHD equilibrium solver VMEC under free-boundary conditions and is used as a basis for the neoclassical calculations performed. The bootstrap current and the parallel flows are examined using the Shaing-Callen 3D neoclassical formulation[Shaing et al., 2015]. The examination of equilibria with ideal response to 3D perturbations such as toroidal field ripple and resonant magnetic perturbations (RMPs) is performed. It is found that RMPs and toroidal ripple produce a weak 3D response leading to a bootstrap current profile indistinguishable from axisymmetry. Any additional effects are further obscured by the presence of numerical resonances on q -rational surfaces. It is found, however, that a non-resonant 1/1 ideal internal kink which avoids the $q = 1$ resonance, is well-suited for computation of the bootstrap current density. The bootstrap current is observed to be strongly augmented in the helical core region of the 1/1 internal kink before returning to match the axisymmetric values in the near-axisymmetric region outside the helical core. Explanations for the augmentation of the bootstrap current are provided in an analytical derivation. A similar augmentation is observed for background ion flows as well, including the presence of a finite poloidal flow. Heavy impurities such as tungsten face friction because of the impurity particles colliding with the background ions, and therefore the magnitude of this flow becomes of paramount importance. The VENUS-LEVIS orbit-following code is used to follow the impurity particles with additional effects provided by the centrifugal and Coriolis forces while colliding them in the correct frame of the background ion distribution. This is successfully benchmarked with known results in neoclassical theory concerning impurity transport. Without flows in axisymmetry, an on-axis peaked impurity distribution is observed. With flows, an off-axis peaking of impurities is observed, following known neoclassical expressions. Furthermore, it is found that the impurity accumulation was strongly increased for the combined case of helical core with flows, leading again to a near-axis peaked density profile. The results are compared heuristically with a known peaking formula incorporating the presence of a finite poloidal flow with toroidal flows, and a reasonable agreement is observed.

Key words: MHD equilibria, Neoclassical theory, Plasma Flows, Bootstrap current, Impurity transport.

Résumé

Cette thèse porte sur l'étude d'instabilités MHD 3D idéales, en particulier du mode "internal kink" 1/1 saturé, et sur des phénomènes néoclassiques tels que le courant de "bootstrap" et le transport d'impuretés lourdes. L'équilibre MHD est généré en utilisant le code d'équilibre MHD idéale VMEC et en considérant des conditions aux bords libres. Cet équilibre est utilisé comme base pour les simulations néoclassiques. Le courant de bootstrap et les flux parallèles sont examinés en utilisant la formulation 3D néoclassique de [Shaing et al., 2015]. L'étude de la réponse idéale de l'équilibre à l'application de perturbation 3D telles que des ondulations du champ toroïdal et de perturbations magnétiques résonantes (RMPs) a été effectuée. Il s'avère que les RMPs et les ondulations toroïdales conduisent à une faible réponse 3D qui débouche sur un profil du courant de bootstrap indistinguable du profil axisymétrique. Les effets supplémentaires sont davantage dissimulés par la présence de résonance numérique sur les surfaces q rationnelles. En revanche, un mode non-résonant "internal kink" 1/1 évitant la résonance $q = 1$ convient au calcul de la densité de courant de bootstrap. On observe que le courant de bootstrap est fortement accru dans la région hélicoïdale du coeur du mode "internal kink" 1/1 et est réduit à une valeur égale aux valeurs axisymétriques dans la région quasi-axisymétrique en dehors du coeur hélicoïdal. Les raisons de cette accroissement du courant de bootstrap sont fournies dans une dérivation analytique. Une augmentation similaire est également observée pour le flux d'ions d'arrière plan, incluant la présence d'un flux poloidal fini. Les impuretés lourdes telles que le Tungstène subissent une friction via leur collision avec les ions d'arrière plan, par conséquent l'importance de ce flux devient primordiale. Le code de suivi d'orbites VENUS-LEVIS est utilisé pour suivre les impuretés. Il inclut à présent les effets additionnels de la force centrifuge ou de Coriolis ainsi que les collisions en considérant une distribution correcte des ions d'arrière-plan. Le nouveau modèle a été validé avec l'aide de résultats connus de théorie néoclassique traitant de la distribution des ions d'arrière-plan. Sans flux axisymétrique, un pic dans la distribution des impuretés sur l'axe est observée. Avec les flux, ce pic est observé en dehors de l'axe, en accord avec les expressions néoclassique MHD Gleichgewichtes établies. De plus, on observe une accumulation d'impuretés fortement augmentée pour le cas combiné du coeur hélicoïdal avec flux, résultant à nouveau en un profil de densité piqué proche de l'axe. Ces résultats sont comparés de manière heuristique avec une formule piquée intégrant la présence d'un flux poloidal fini avec des flux toroïdaux. Un accord raisonnable est observé.

Mots clefs : équilibre MHD, théorie néoclassique, flux de plasma, courant de Bootstrap, trans-

port d'impuretés

Zusammenfassung

Diese Dissertation befasst sich mit der Erforschung von idealen 3D Instabilitäten, insbesondere von gesättigten idealen 1/1 internen Kink-Moden, neoklassischen Phänomenen wie dem Bootstrap-Strom und Transport, verursacht durch schwere Verunreinigungen. Die MHD Gleichgewichte werden mit Hilfe des idealen MHD Codes VMEC unter der Bedingung einer frei beweglichen Plasmaberandung erzeugt. Sie sind die Grundlage für die neoklassischen Berechnungen. Der Bootstrap-Strom und die parallelen Strömungen werden anhand der neoklassischen Shaing-Callen 3D Formulierung [Shaing et al., 2015] bestimmt. Eine Untersuchung von Gleichgewichten mit idealer Reaktion zu 3D Störungen wie toroidale Magnetfeldwellen (toroidal field ripples) und resonante magnetische Störungen (RMPs) wird durchgeführt. Wir beobachten, dass RMPs und toroidal field ripples eine schwache 3D Reaktion hervorrufen, die ununterscheidbar von Axisymmetrie ist. Andere, zusätzliche Effekte werden weiter verschleiert durch die Präsenz von numerischen Resonanzen auf rationalen q Flussoberflächen. Jedoch wird beobachtet, dass eine nichtresonante ideale 1/1 interne Kink-Mode, die $q = 1$ Resonanz meidet, gut für die Berechnung der Bootstrap-Stromdichte ist. Es wird beobachtet, dass der Bootstrap-Strom in der spiralförmigen Region des Plasmakerns der internen 1/1 Kink-Mode stark erhöht ist, bevor die axisymmetrischen Werte in der axisymmetrisch-nahen Region ausserhalb des spiralförmigen Kerns erreicht werden. Erklärungen für die Erhöhung des Bootstrap-Stroms werden anhand von analytischen Herleitungen geliefert. Eine ähnliche Erhöhung wird auch für Hintergrundionen-Strömungen, einschliesslich der Anwesenheit endlicher poloidaler Ströme, beobachtet. Schwere Verunreinigungen, z.B. Wolfram sind aufgrund der Kollisionen mit den Hintergrundionen Reibung ausgesetzt und daher ist die Grössenordnung dieser Strömung von höchster Wichtigkeit. Der VENUS-LEVIS Code zum Verfolgen von Teilchenorbits wird verwendet um die Trajektorien der Teilchen der Verunreinigungen nachzuvollziehen. Dies geschieht unter Berücksichtigung zusätzlicher Effekte durch die Zentrifugal- und Corioliskraft während die Teilchen im korrekten Bezugssystem der Hintergrundionen zusammenstossen. Dies wurde anhand von bekannten Ergebnissen aus der neoklassischen Theorie hinsichtlich Transport von Verunreinigungen überprüft. Ohne Strömungen in Axisymmetrie werden Verunreinigungsverteilungen mit Höchstwert auf der magnetischen Achse beobachtet. Mit Strömungen befindet sich der Höchstwert der Verunreinigungsverteilung abseits der magnetischen Achse, gemäss bekannten neoklassischen Ausdrücken. Weiterhin stellt sich heraus, dass die Ansammlung von Verunreinigungen stark erhöht ist für den Fall von kombiniertem spiralförmigen Kern mit Strömungen. Dies führt erneut zu einem Dichteprofil mit Höchstwert nahe der magnetischen Achse. Die Ergebnisse werden verglichen mit

einer bekannten heuristischen Formel, die Anwesenheit einer endlichen poloidialen Strömung mit toroidialen Strömungen berücksichtigt und eine angemessene Übereinstimmung ist vorhanden.

Stichwörter: MHD Gleichgewichte, Neoklassische Theorie, Plasmaströmung, Bootstrap-Strom, Verunreinigungstransport.

Contents

Abstract in English, French and German	i
Contents	vii
List of figures	xi
List of tables	xv
1 General Introduction	1
1.1 Historical background of 3D tokamaks	1
1.2 Recent Research in 3D Geometry of Plasmas	4
1.3 Outline of the Thesis	6
2 Equilibrium Theory, Guiding-Center Orbits and Neoclassical Theory with Flows	7
2.1 Ideal Axisymmetric MHD equilibrium with Zeroth-Order Plasma Rotation . . .	7
2.2 VMEC and the Variational Formulation with Flows	10
2.2.1 Equilibrium Without Flows	11
2.2.2 Axisymmetric Equilibrium with Purely Toroidal Flows	14
2.2.3 Limitations of 3D Equilibria with Purely Toroidal Flows	16
2.3 Plasma Flows and Ordering	17
2.3.1 Lowest-Order Flows \mathbf{U}_0	18
2.4 Higher-order Flow \mathbf{U}_1	18
2.5 Guiding-Center formulation	20
2.5.1 Implementation of the Guiding-Center Equations in VENUS-LEVIS . . .	23
2.5.2 Quasi-neutrality corrections in case of plasma rotation	25
2.5.3 Equivalence with the Traditional Expression for Drifts	27
2.6 Introduction to bootstrap current	29
2.7 Bootstrap Current Models and Approach to Simulation	30
2.7.1 Sauter Model	31
2.7.2 Shaing-Callen Model	32
2.7.3 Axisymmetric Comparison of the Sauter and the Shaing-Callen Formulations	33
2.7.4 Numerical resonance mitigation	34
2.7.5 Self-Consistent Computation of The Toroidally-Averaged Bootstrap Current	35

Contents

2.8	Neoclassical Physics of the Background Plasma and Impurities	37
2.8.1	Recovery of Known Neoclassical Results in a Rotating Axisymmetric Equilibrium	38
2.9	Summary of the General Theory Background	39
3	Effects of 3D on Bootstrap Current	41
3.1	Edge Pedestal with Weak 3D effects: Toroidal Field Ripple and RMPs	42
3.1.1	Benchmark with an axisymmetric MAST equilibrium	44
3.1.2	Bootstrap Current for a 3D Equilibrium with Toroidal Field Ripple	46
3.1.3	Bootstrap Current for a 3D Equilibrium with RMPs	54
3.1.4	Summary of Bootstrap Current in Axisymmetry with RMPs and Toroidal Ripple	55
3.2	Internal Pressure Barriers with Strong 3D effects: Saturated 1/1 internal kink	55
3.2.1	Bootstrap Current for a Saturated 1/1 Internal Kink	56
3.2.2	Comparison of the Sauter and Shaing-Callen Formulations: Particle Trapping and Geometry	62
3.2.3	Summary of Bootstrap Current in 1/1 Helical Geometry	65
3.3	Summary and Outlook	67
4	Effect of 3D on Impurities	69
4.1	Introduction	69
4.2	Impurity Trajectories with Collisions	71
4.2.1	Centrifugal Effects	71
4.2.2	Neoclassical Effects	73
4.3	Neoclassical properties of Axisymmetric and Helical-core Equilibria	74
4.4	Simulations of Tungsten Neoclassical Transport	78
4.4.1	Benchmark for a Non-Rotating Axisymmetric Equilibrium	80
4.4.2	Benchmark for Axisymmetry with Plasma Rotation	82
4.4.3	Simulations for 1/1 Saturated Internal Kink with Rotation	86
4.5	Conclusions	90
5	Outlook and Future Work	93
5.1	Exploring the Impurity Screening Effects of Temperature Gradients	93
5.2	More Accurate Computation of Higher-Order Potential Φ_1 and 3D Flows	93
5.3	Extension into Different Collisional Regimes	94
5.4	Extending the Scope of the MHD equilibrium	94
5.5	Modeling of Experiments in JET	95
6	Summary and Conclusions	97
6.1	Summary of the Thesis	97
6.2	Final Words	98

Bibliography	104
---------------------	------------

Contents

Acknowledgments	105
Curriculum Vitae	107

List of Figures

1.1	A schematic representation of a tokamak. The D-shaped coils provide the toroidal magnetic field. The central solenoid (inner poloidal field coil) provides the current drive and the main poloidal magnetic field. The horizontal circular coils are poloidal coils that help with the shaping of the plasma. Courtesy of the EUROfusion website.	2
1.2	A visible length photograph of the MAST tokamak. Courtesy of the CCFE website.	3
1.3	A cross-section of the JET vessel with visible length photograph of the JET tokamak plasma. Courtesy of Wikipedia.	3
1.4	A schematic representation of the W7-X stellarator. One can notice the discretized coils responsible for producing a complex 3D magnetic field geometry. Courtesy of the EUROfusion website.	4
2.1	The surfaces of constant pressure (colourbar in Pa) in the same equilibrium with and without flow. It can be noticed that the constant pressure surfaces with toroidal flow shift towards the low field side and do not align with the magnetic flux surfaces (black curves) anymore. The supersonic Mach number is chosen $\mathcal{M}_j^2 = 10$ is chosen for illustrative purposes.	9
2.2	An example of a JET like helical core equilibrium obtained with VMEC. The contours are surfaces of constant pressure, and the shade refers to the magnetic field intensity B . Notice how the axis is helically distorted in comparison to the last closed flux surface.	11
2.3	The mode spectrum for the helical core obtained in Fig. (2.2). The colour scale is logarithmic with respect to the largest mode-value. One can see that the spectrum is converged and does not need more modes for resolving the 1/1 mode.	12
2.4	The guiding-center orbit (red) as compared to full Lorentz (green) orbit. It follows closely to each other within the first-order guiding-center approximation. Again, the Mach number is chosen to be $\mathcal{M}_0^2 = 20$ for illustration purposes.	27
3.1	The pressure profile is chosen so as to generate a VMEC equilibrium a steep edge pressure pedestal. Notice the pressure barrier staring at $s = 0.8$	43
3.2	The temperature profile is chosen so as to generate a VMEC equilibrium a steep edge pressure pedestal. The temperature profile flattens at $s > 0.8$ corresponding to the pedestal in pressure.	44

List of Figures

3.3	The safety factor q -profile for the simulations for the chosen initial current and pressure profiles.	45
3.4	Profiles of the parallel bootstrap current density $\langle \mathbf{J}_{BS} \cdot \mathbf{B} \rangle$ obtained according to the <i>Sauter</i> formula (the black curve) and the <i>Shaing-Callen</i> formula (red '+' points).	46
3.5	Plot of <i>Sauter</i> parallel bootstrap current density $\langle \mathbf{J}_{BS} \cdot \mathbf{B} \rangle$ for each iteration of the bootstrap procedure. The profile for each n^{th} iteration is the input for the VMEC equilibrium calculation of the $(n + 1)^{th}$ iteration.	47
3.6	Plot of the total current profile $\langle \mathbf{J} \cdot \nabla \Phi \rangle$ for each iteration of the bootstrap procedure. The profile for each n^{th} iteration is the input for the VMEC equilibrium calculation of the $(n + 1)^{th}$ iteration.	47
3.7	Comparison of the <i>Shaing-Callen</i> formula and the <i>Sauter</i> formula for bootstrap current densities after the first iteration.	48
3.8	A side-by-side comparison of the <i>Sauter</i> and <i>Shaing-Callen</i> bootstrap current densities with the q -profile. It can be seen that the spikes on the edge bootstrap current correspond to rational values of q on the profile.	49
3.9	The parallel <i>Shaing-Callen</i> bootstrap current density $\langle \mathbf{J}_{BS} \cdot \mathbf{B} \rangle$ for different values of detuning factor Δ . The dashed black line in the background is the <i>Sauter</i> bootstrap current. The bootstrap current density curve for $\Delta = 10^{-7}$ overlaps with the curve for $\Delta = 10^{-4}$	50
3.10	Diagram depicting coil placement in MAST. The doughnut shaped figure is a plot of the magnetic field strength the last closed flux-surface of the equilibrium. The toroidal field coils are shown in orange, and the RMP coils are shown in red.	51
3.11	The effect of increasing TF-coil numbers on the parallel <i>Shaing-Callen</i> bootstrap current densities. The resonance detuning factor is fixed at $\Delta = 10^{-4}$. The black dashed curve represents the <i>Sauter</i> bootstrap current density for the same Δ	52
3.12	A plot of the bootstrap current density, for the case of 32 TF coils, for increasing sampling in radial variable s . We have especially zoomed in between the near-edge region $s = 0.8 - 1.0$. It is immediately noticeable that the increase in the sampling produces neither a significant amelioration of the numerical resonance, nor do the non-resonant portions differ significantly.	53
3.13	The parallel <i>Shaing-Callen</i> bootstrap current density $\langle \mathbf{J}_{BS} \cdot \mathbf{B} \rangle$ as calculated for 12 TF-coils for a MAST 3D equilibrium with varying RMP currents. The black dashed curve represents the <i>Sauter</i> bootstrap current. The resonance detuning factor is set to $\Delta = 10^{-4}$. Note in particular the higher (m, n) mode number resonances caused in the mid-radius.	54
3.14	The rotational transform ι profile chosen to generate a helical core.	56
3.15	The chosen density profile in order to produce a helical core equilibrium. We can see that in the helical core-region up to $s = 0.2$, there is a steep density (and hence, pressure) gradient, providing a weak internal pressure barrier.	57

3.16	The helical core equilibrium obtained from VMEC for the specified ι -profile and pressure profile. One surface from inside the helical core ($s = 0.1$), one from near the internal axisymmetric boundary ($s = 0.25$) and the last from the edge ($s = 1$) are shown here for reference.	58
3.17	A comparison of toroidal cross-sections of (s, u, v) coordinate grids for the helical core equilibrium and its axisymmetric sister-state. The magenta coloured lines are lines of constant poloidal angle variable u . The helical core region is represented by green coloured lines of constant s , and the axisymmetric mantle is represented by blue coloured lines of constant s	59
3.18	The bootstrap current densities calculated for the axisymmetric analogue equilibrium for the chosen helical core parameters.	60
3.19	We choose a q -profile which avoids major resonant surfaces in the helical-core region. The figure above represents the bootstrap current profiles specified by the <i>Sauter</i> and <i>Shaing-Callen</i> formulations respectively and the figure below shows the chosen ι -profile.	61
3.20	A comparison between the exactly calculated trapped fraction f_t and the trapped fraction calculated under axisymmetric conditions for the vacuum form of the magnetic field $f_{t,approx}$ for the helical core case.	64
3.21	The geometrical factor G_b for the <i>Shaing-Callen</i> model. The geometrical factor goes to zero on the magnetic axis, and it exhibits the resonances observed in the axisymmetric mantle.	65
3.22	A focus on the bootstrap current density in the helical core region. Also plotted are the trapped fractions and the geometrical factor in order to compare the variations of the <i>Sauter</i> and <i>Shaing-Callen</i> bootstrap current prescriptions against the causal factors.	66
4.1	The distributions in the rest frame.	74
4.2	The distributions in the frame moving with the background ions.	75
4.3	The selected profiles used for generating the helical and axisymmetric branches of the VMEC equilibria.	76
4.4	Toroidal cuts of the VMEC equilibria for a helical core and its axisymmetric sister state. Notice how the constant pressure surfaces are shifted by the saturated internal kink.	77
4.5	The computed values of the parallel velocity $U_{1\parallel,i}$	79
4.6	The associated value of the poloidal flow velocity $U_{1\theta,i}$ for the helical core.	79
4.7	The density profile of the impurity with time for an axisymmetric JET-like equilibrium without rotation. Notice the slow but constant inward drift of the density, leading to heavy impurity peaking on the axis.	81
4.8	Plot of the predicted and numerically obtained impurity density for an axisymmetric equilibrium without flow. The black dashed curve represents the one plotted from Eq. (2.164). We find that they are in good agreement.	81

List of Figures

4.9	Density plot for the axisymmetric equilibrium without flow at $t = 2s$. As we expect, the tungsten impurities concentrate on the axis with the density following the predicted density.	82
4.10	The time progression of the density profile for an axisymmetric equilibrium case with 20kHz rotation.	83
4.11	Plots of density of tungsten for the axisymmetric equilibrium with 20kHz rotation. We notice that the impurities, deeply trapped on the low field side, saturate off-axis	83
4.12	Plot of the predicted and numerically obtained impurity density for an axisymmetric equilibrium with 20kHz plasma flow. The dashed black curve represents the saturated state obtained from Eq. (4.5). We find that they are in reasonable agreement, with the off-axis peaking reasonably predicted well.	85
4.13	The plots of the density profile for a helical core equilibrium with 20kHz rotation (zoomed in from $s = 0.05 - 0.3$).	87
4.14	Plots of density of tungsten on various toroidal cuts for a helical core case with 20kHz rotation, assuming a value of the geometrical factor G_b consistent with the equilibrium. One can notice that the impurities for this case are pinched much closer towards the axis, following the axis of the helical core.	88
4.15	Plot of intensity of density peaking for axisymmetry and helical core without flow and helical core with flow. The figure is zoomed to $\rho_{tor} = 0.35$ for convenience of comparison.	89
4.16	Comparison of obtained density with density predicted from Eq. 2.163.	90

List of Tables

4.1	Values of essential parameters used in the equilibrium generation for a JET-like case	78
-----	---	----

1 General Introduction

Nuclear fusion will be a viable source of clean energy for the future where energy needs from alternative sources will become important due to the decrease in availability of fossil fuels. Additionally fusion also is a solid candidate of a central power source in a power grid that consists of a hybrid centralized-decentralized power grids.¹ Fusion, as compared to fission, is different in that it involves fusing smaller nuclear together to form a heavier nucleus, the mass defect in which is converted to energy. An advantage of fusion over fission is also the significantly reduced quantities of long-lived nuclear waste. There are several proposed methods to perform fusion in devices with a controlled release of energy: magnetic-confinement fusion, electrostatic confinement, inertial fusion, and electromagnetic pinch approaches[Wikipedia, 2017]. The field in which this thesis is oriented is that of magnetic confinement - an area of research spanning 70 years. Magnetic-confinement fusion involves the creation of a magnetic fields in which a high-temperature plasma can be contained and heated to the point which the collisions among the ions will lead to their fusing. However, such fusion comes with challenges of its own, particularly the confinement and the heating of the confined particles. Further challenges come from the design idiosyncrasies of the machine which add additional complexities to an already difficult problem. We now describe the current leading machine type for fusion power, i.e. the Tokamak.

1.1 Historical background of 3D tokamaks

For nuclear fusion, the main contenders for reaching net positive energy output today are two classes of machines: Tokamaks and Stellarators.

Tokamaks are a class of magnetic confinement fusion device that consist of a toroidal magnetic field coupled with a small poloidal magnetic field to create the confining magnetic fields necessary for the confinement of plasma. Literally, the word Tokamak is an acronym for the

¹Nuclear fusion also is a good candidate of energy and propulsion exhaust for large-sized manned spacecrafts for long deep-space journeys where starlight does not constitute an adequate source of energy. For the long-term future of humanity, such spacecrafts will become an absolute necessity.

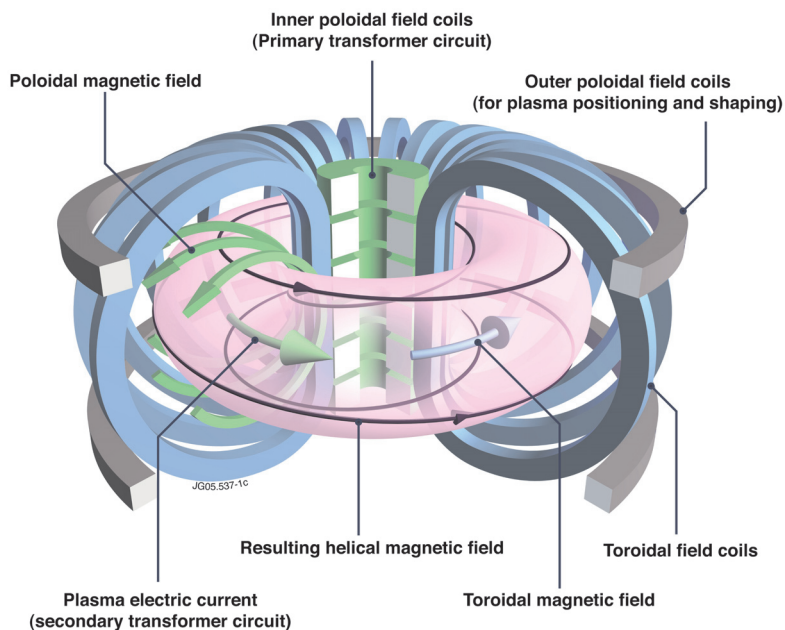


Figure 1.1 – A schematic representation of a tokamak. The D-shaped coils provide the toroidal magnetic field. The central solenoid (inner poloidal field coil) provides the current drive and the main poloidal magnetic field. The horizontal circular coils are poloidal coils that help with the shaping of the plasma. Courtesy of the EUROfusion website.

Russian name of the machine which translates to, ‘Toroidal Chamber with axial magnetic coils.’ By design, it was intended to confine plasma in an axially-symmetric, or axisymmetric fashion. However, it was soon realized that the plasma can assume deviations from such a symmetry, and exhibit magnetic structures in 3D. Such deviations may arise from several factors. Intrinsically, they may arise from the coil geometry. For example, a toroidal field ripple exists because the toroidal field coils are discrete and not continuous. 3D deviations in the core, such as the 1/1 internal kink, arises due to the nature of the field-plasma interaction, and is intrinsic to the self-organising nature of plasma behaviour and will exist even in perfect magnetic toroidal symmetry of confining coils. Examples of tokamaks include the Mega-Ampere Spherical Tokamak (MAST, pictured in Fig. 1.2) and the Joint European Torus (JET, shown in Fig. 1.3), and the future tokamaks ITER (under construction) and DEMO (design in progress). Tokamaks have been demonstrated to have good confinement properties, barring effects causing confinement degradation, such as neoclassical tearing modes, edge localized modes (ELMs) and disruptions[Wesson and Campbell, 2011].

The second class of machines, called Stellarators, are intrinsically 3D in nature with a sophisticated magnetic coil geometry which leads to the formation of fully-3D magnetic field structure. The concept of Stellarators was first proposed by Lyman Spitzer in 1951 in an internal Project Matterhorn report later declassified in 1958[Spitzer, 1958]. By design, such machines do not face some of the physical limitations of tokamaks such as disruptions, and can automatically operate in steady-state. However, particle confinement and plasma heating capability

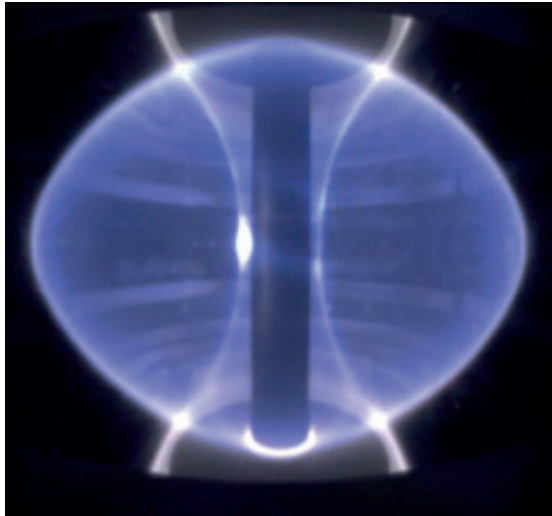


Figure 1.2 – A visible length photograph of the MAST tokamak. Courtesy of the CCFE website.

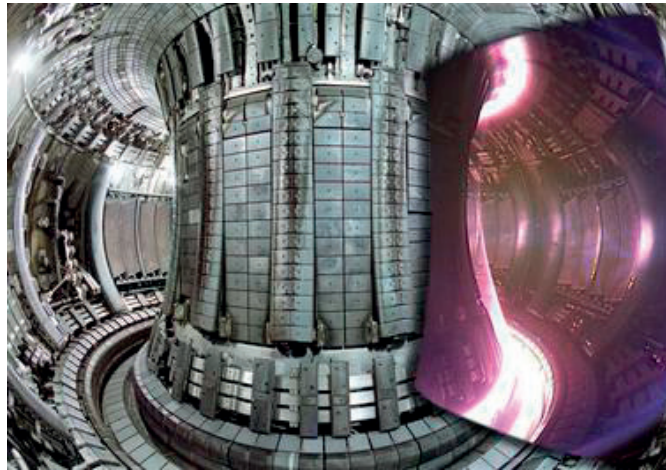


Figure 1.3 – A cross-section of the JET vessel with visible length photograph of the JET tokamak plasma. Courtesy of Wikipedia.

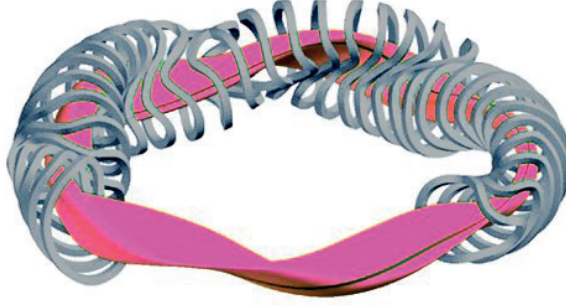


Figure 1.4 – A schematic representation of the W7-X stellarator. One can notice the discretized coils responsible for producing a complex 3D magnetic field geometry. Courtesy of the EUROfusion website.

is poor for such machines currently, and high-performance has been barely demonstrated. In this thesis, we do not consider any stellarator application cases. Nevertheless, some 3D magnetic structures in tokamaks however, such as the 1/1 internal kink, exhibit stellarator-like properties with reduced plasma performance. The neoclassical physics research of such magnetic geometries in tokamaks overlaps considerably with the neoclassical physics for stellarators[Shaing et al., 2015], and is of considerable interest. Examples of stellarators include the Large Helical Device (LHD) and the Wendelstein 7-X (W7-X, pictured in Fig. 1.4). Stellarators can in principle operate in steady-state and do not face disruptions. However, confinement properties are yet to be demonstrated.

In the current thesis, we confine ourselves to the study of tokamaks operating with strongly 3D plasmas. This will include the studying of the effects of the saturated 1/1 internal kink and other 3D effects on certain properties of the tokamaks such as the bootstrap current and heavy impurity accumulation.

1.2 Recent Research in 3D Geometry of Plasmas

Both bootstrap current and impurity transport are inherently neoclassical phenomena, and thus require a treatment that bridges 3D MHD equilibria and neoclassical theory of non-axisymmetric systems. Neoclassical transport theory is needed, in addition to classical thermodynamic transport, in order to account for the magnetic field structure in a tokamak. The curved toroidal and poloidal magnetic fields result in new orbit structures, such as trapped banana orbits on the low-field side of the machine, which interact with the “passing” particles resulting in collisional effects which are not accounted for in classical theory. Such an interaction of trapped and passing orbits is found to have a profound effect on the plasma behaviour[Hinton and Hazeltine, 1976, Helander and Sigmar, 2005]. Furthermore, the introduction of non-axisymmetric fields in the toroidal direction further adds one more dimension to all transport processes[Helander, 2014]. The bootstrap current is a self-generated current in the plasma which occurs because of a small fraction of particles near

the trapped-passing boundary being released into passing orbits which carry current. For the bootstrap current, neoclassical theory has been developed in 3D for various collisional regimes [Shaing et al., 2015], formulae and scalings of which are used as a backbone for our computations. For impurity transport, it is necessary to model correctly the interaction between the heavy impurity species and the background ions. In the trace density limit, where we can safely neglect self-interaction of the impurities, we need a consistent neoclassical description of the background plasma, i.e. the flows and the fluxes faced by the background plasma. Neoclassical theory in 3D, and especially the description of background flows, is taken from existing literature [Helander, 2014, Shaing et al., 2015].

A saturated 1/1 internal kink is an MHD instability that is stable over relatively long periods of the plasma experiment. Saturated 1/1 internal kinks manifest themselves as Long-Lived Modes (LLMs) in MAST [Chapman et al., 2010, Chapman et al., 2014], and are also known informally as continuous modes in JET. These modes are expected to be observed in ITER and other future tokamaks where they will play an important role in plasma operation. In this thesis, we consider a saturated 1/1 internal kink with a low-shear q -profile which avoids a resonance at the $q = 1$ rational surface. Such modes have been shown to exist in Ref. [Brunetti et al., 2014] and the references therein. Confinement of fast ions generated by neutral beam injection (NBI) has previously been demonstrated to strongly be affected by the 3D internal kink [Pfefferlé et al., 2014b, Pfefferlé, 2015].

For tokamaks with pressure pedestals near the edge, as found in H-mode operations, the bootstrap current acquires a large value, significantly reducing the dependence on current drive. In TCV, operation of the tokamak with 100% bootstrap current has been demonstrated [Coda et al., 2007], leading to hopes that future tokamaks can achieve high bootstrap-current fractions. This thesis investigates the effect of relatively steep pressure gradients in the core region, just outside of the low q -shear region (and just outside of the 1/1 kinked magnetic field). It is shown that the helical core can strongly affect the bootstrap current and plasma flows associated with the steep pressure gradients associated to the 1/1 internal kink.

Another effect observed in plasma experiments with a saturated 1/1 modes with plasma flow is the increased accumulation of impurities [Graves et al., 2000]. Normally this effect is weaker in tokamaks with carbon-based walls, and the impurities are usually not in such a high concentration so as to affect the plasma performance itself. Therefore, charge-exchange reactions with carbon are often used as a diagnostic to learn about the flows of the background plasma. However, future tokamaks like ITER and DEMO are designed to have tungsten walls. Tungsten, possessing a very high number of ionisation states, leads to a drain on the heat of the core plasma even when present in a relative concentration as 10^{-3} of the plasma density, leading to a radiative collapse. In the thesis, we explore the neoclassical physics surrounding an ideal 1/1 internal kink, plasma rotation and impurity accumulation.

1.3 Outline of the Thesis

The thesis is organized as follows:

In Chapter 2, we provide a detailed description of the physical models that go into the applications considered. This first includes a description of the equilibrium model in 2D and 3D with strong toroidal plasma flows, including the limitations of current 3D MHD models with rotation. Then we describe how the particle orbits can be derived under strong flows using a guiding-center model that accurately reproduces the conservation properties. Plasma flows in various orders and of different origins are described as well. These flows can be used for looking at heavy impurity test-particle interactions with the plasma. A brief description of the frictional effects of such flows on the heavy impurities is then provided. In regards to the bootstrap current calculations, the Sauter and Shaing-Callen models are described, the former being a fit-based approximation valid for axisymmetry and the second being an analytical approximation valid in both 2D and 3D.

In Chapter 3, we take a detailed look at the bootstrap current in 2D and 2D magnetic field configurations. As mentioned before, we compare the Sauter[Sauter et al., 1999] and Shaing-Callen[Shaing and Callen, 1983] models of bootstrap current. The Sauter model is an axisymmetric numerical approximation and the Shaing-Callen model is a neoclassical model valid self-consistently for 3D. First examine a near-axisymmetric equilibrium with a strong edge-pedestal, including small perturbations provided at the edge by RMP coils. We use this case to benchmark the two models. Then, we investigate the predictions of the two models on a 3D equilibrium with a saturated 1/1 internal kink and provide explanations for the observed effects. One aim of this chapter is to demonstrate the viability of the non-resonant 1/1 internal kink as a good candidate for the current thesis.

Chapter 4 is dedicated to a novel investigation into the effect of plasma flows on heavy-impurity-accumulation in 2D and 3D magnetic fields. We first benchmark the peaking observed in axisymmetry through inclusion of neoclassical effects without flows. Then we observe the effects of strong plasma flow in an axisymmetric plasma and a plasma with a saturated 1/1 internal kink. We also perform comparisons with known analytic approximations for the density peaking. This chapter aims to see how a 1/1 internal kink affects impurity accumulation and provides explanations for impurity accumulation during continuous 1/1 mode activity in tokamaks.

In Chapter 5, we summarize the thesis and provide possible ways to expand on the work performed in the current thesis.

2 Equilibrium Theory, Guiding-Center Orbits and Neoclassical Theory with Flows

This chapter describes the basic known theory of the physics involved in the thesis. No new results are shown, and this chapter serves to lay the foundation on which further chapters rest. Since the basis for work in the thesis is given by the availability of 3D ideal MHD equilibria, the next section describes a model of 3D equilibria with flow and the constraints faced by 3D equilibria. Then we describe the guiding-center physics involved in tracking particle orbits through flowing plasmas. We also describe the neoclassical physics that come in through particle-background collisions and describe the physics in various collisional regimes of the plasma. Finally, we explain the two cases where these building blocks form clear applications. The first is the calculation of the background plasma bootstrap current in the banana regime (or the $\sqrt{\nu}$ -collisionless regime). The second application is the effect of background plasma flows and 3D equilibrium on heavy impurity accumulation.

2.1 Ideal Axisymmetric MHD equilibrium with Zeroth-Order Plasma Rotation

We first begin with the set of equations that define the ideal MHD model with flows at equilibrium (i.e. $\partial/\partial t = 0$). They are given as follows[Maschke and Perrin, 1980]:

$$-\mu_0 \nabla p + \mathbf{J} \times \mathbf{B} - \mu_0 \rho \mathbf{U}_{0,j} \cdot \nabla \mathbf{U}_{0,j} = 0 \quad (2.1)$$

$$\mathbf{E} + \mathbf{U}_{0,j} \times \mathbf{B} = 0 \quad (2.2)$$

$$\nabla \cdot (\rho \mathbf{U}_{0,j}) = 0 \quad (2.3)$$

$$\nabla \cdot \mathbf{B} = 0 \quad (2.4)$$

$$\nabla \cdot \mathbf{E} = 0 \quad (2.5)$$

$$\nabla \times \mathbf{B} = \mu_0 \mathbf{J} \quad (2.6)$$

$$\frac{d}{dt}(\rho p^\Gamma) = 0 \quad (2.7)$$

$$\mathbf{B} \cdot \nabla S_j = 0 \quad (2.8)$$

Chapter 2. Equilibrium Theory, Guiding-Center Orbits and Neoclassical Theory with Flows

where \mathbf{E} and \mathbf{B} are the electric and magnetic fields respectively, \mathbf{J} is the current density, $\mathbf{U}_{0,j}$ is the zeroth-order plasma flow for the species j , $p = p_i + p_e$ is the total pressure, ρ is the mass density, and Γ the adiabatic index. Equation (2.1) is the ideal MHD force balance equation with flows, equation (2.2) is the Ohm's law under ideal conditions, equation (2.3) is the continuity equation, equations (2.5) and (2.4) are the Gauss' laws for electric and magnetic fields, equation (2.6) is the Faraday law, equation (2.7) is the adiabatic closure expression for ideal MHD, and finally Eq. (2.8) is the entropy conservation condition, which shows that the entropy S_j is a flux-surface quantity. Together with adiabaticity of the plasma consistent with kinetic theory[Helander, 2014], this leads to the isothermal condition

$$\mathbf{B} \cdot \nabla T_j = 0, \quad (2.9)$$

i.e., the temperature remains a flux-surface function, $T_j \equiv T_j(\psi)$. Using the ideal Ohm's law and Faraday's law, we obtain

$$\nabla \times (\mathbf{U}_{0,j} \times \mathbf{B}) = 0, \quad (2.10)$$

which on expanding and taking the $\nabla\phi$ component, one obtains

$$\mathbf{B} \cdot \nabla U^\phi = B^\phi \nabla \cdot \mathbf{U} + \mathbf{U} \cdot \nabla B^\phi. \quad (2.11)$$

where the superscript index refers to the contravariant representation of the vector fields (and where the subscript would refer to the covariant representation). In conjunction with the continuity equation, we find

$$\mathbf{B} \cdot \nabla U^\phi = \frac{B^\phi}{\rho} \nabla \rho \cdot \mathbf{U} + \mathbf{U} \cdot \nabla B^\phi. \quad (2.12)$$

On imposing a toroidal flow of the form $\mathbf{U} = U^\phi \mathbf{e}_\phi$, we find for axisymmetric conditions, the terms in the RHS of Eq. (2.12) vanish, and we finally obtain

$$\mathbf{B} \cdot \nabla U^\phi = 0, \quad (2.13)$$

implying that for axisymmetric toroidal flow, the flow velocity $U^\phi = \Omega(\psi)$ is a flux-surface function as well, through which the flow field can be represented as $\mathbf{U} = \Omega \mathbf{e}_\phi = R^2 \Omega \nabla \phi$. Using this flow in the MHD force balance relation, and that $\Omega \mathbf{e}_\phi \cdot \nabla \Omega \mathbf{e}_\phi = \Omega^2 \nabla(R^2/2)$, we find

$$-\mu_0 \nabla p + \mathbf{J} \times \mathbf{B} - \mu_0 \rho \Omega^2 R \nabla R = 0, \quad (2.14)$$

on taking the parallel component leads to

$$\left. \frac{\partial p}{\partial R} \right|_\psi = -\rho \Omega^2 R. \quad (2.15)$$

2.1. Ideal Axisymmetric MHD equilibrium with Zeroth-Order Plasma Rotation

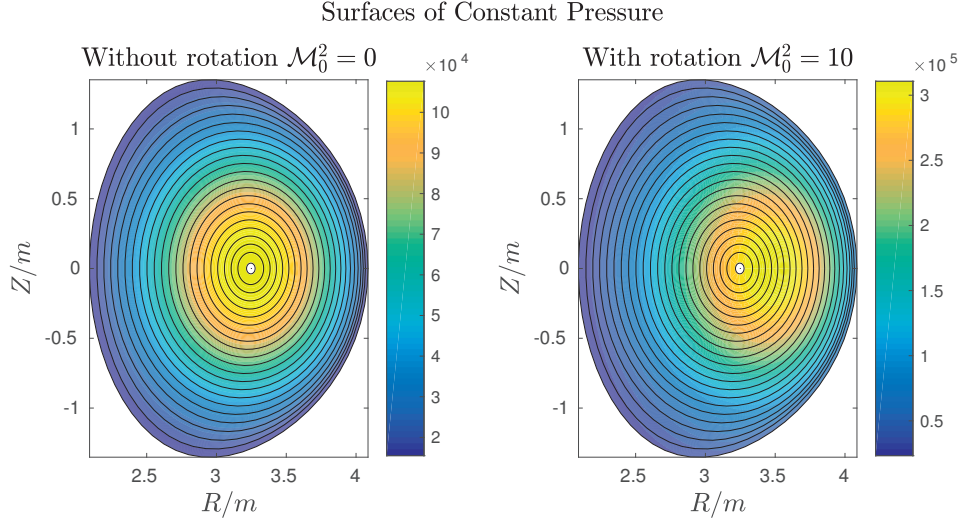


Figure 2.1 – The surfaces of constant pressure (colourbar in Pa) in the same equilibrium with and without flow. It can be noticed that the constant pressure surfaces with toroidal flow shift towards the low field side and do not align with the magnetic flux surfaces (black curves) anymore. The supersonic Mach number is chosen $\mathcal{M}_0^2 = 10$ is chosen for illustrative purposes.

From this, assuming $T_i = T = T_e$, and using $p = 2\rho T(\psi)$, one can obtain the pressure to be of the form

$$p(\psi, R) = p_0(\psi) \exp \frac{m_i \Omega(\psi)^2 R^2}{4T(\psi)}, \quad (2.16)$$

i.e., the pressure is composed of a leading-order surface quantity $p_0(\psi)$ and a R -dependent profile correction to account for the flow field. Thus the surfaces of constant pressure are shifted with respect to the flux-surfaces, as illustrated in Fig. 2.1. Furthermore, the quantity

$$\mathcal{M}_0^2 = \frac{m_i \Omega_0^2 R_0^2}{2T_0} = \left(\frac{\Omega R_0}{v_{th}} \right)^2, \quad (2.17)$$

where $v_{th} = \sqrt{2T/m_i}$ is the thermal velocity of the background ions, is the Mach number of the flow.

Now, on taking the $\nabla\psi$ component of the force balance equation, we obtain

$$-\mu_0 \nabla p \cdot \nabla \psi + (\nabla \times \mathbf{B}) \times \mathbf{B} \cdot \nabla \psi - \mu_0 \rho \Omega^2 R \nabla R \cdot \nabla \psi = 0 \quad (2.18)$$

which on taking the axisymmetric magnetic field in the form $\mathbf{B} = B_\phi \nabla \phi + \nabla \phi \times \nabla \psi$ reduces to

$$-|\nabla \psi|^2 \left\{ \nabla \cdot (|\nabla \phi|^2 \nabla \psi) + \mu_0 \frac{\partial p}{\partial \psi} \Big|_R + |\nabla \phi|^2 B_\phi \frac{\partial B_\phi}{\partial \psi} \right\} - (\nabla R \cdot \nabla \psi) \mu_0 \left\{ \frac{\partial p}{\partial R} \Big|_\psi + \rho \Omega R^2 \right\} = 0. \quad (2.19)$$

Chapter 2. Equilibrium Theory, Guiding-Center Orbits and Neoclassical Theory with Flows

We can see, from Eq. 2.15, that the coefficient of the $\nabla R \cdot \nabla \psi$ term in the Eq. 2.20 is zero, leading to a Grad-Shafranov equation modified for rotation of the form

$$\nabla \cdot (|\nabla \phi|^2 \nabla \psi) + \mu_0 \left. \frac{\partial p}{\partial \psi} \right|_R + |\nabla \phi|^2 B_\phi \frac{\partial B_\phi}{\partial \psi} = 0. \quad (2.20)$$

Since $|\nabla \phi| = 1/R$, we have

$$\nabla \cdot \left(\frac{\nabla \psi}{R^2} \right) + \mu_0 \left. \frac{\partial p}{\partial \psi} \right|_R + \frac{B_\phi}{R^2} \frac{\partial B_\phi}{\partial \psi} = 0. \quad (2.21)$$

One can solve the Grad-Shafranov equation to obtain axisymmetric equilibria under some limitations, such as a Solov'ev equilibrium with fixed aspect ratio at the boundary [Maschke and Perrin, 1980]. We do not use a Grad-Shafranov solver to obtain or equilibria, as we use the general 3D equilibrium code VMEC, described in the next section.

2.2 VMEC and the Variational Formulation with Flows

The Variational Moments Equilibrium Code (VMEC) can be used to obtain a myriad of 2D and 3D ideal MHD equilibria [Hirshman and Whitson, 1983, Hirshman et al., 1986]. The code has been successfully used to compute and obtain the fields for an axisymmetric equilibrium with fixed boundary and free boundary conditions with purely toroidal flows. It has also been used to compute a 3D equilibrium with a saturated ideal internal kink mode and saturated external harmonic modes. The fields obtained can be used to develop particle orbits and study linear stability of ideal MHD modes. This comes at a disadvantage of not being able to include resistive effects and magnetic structures such as magnetic islands. The advantage of VMEC, as compared to time-dependent MHD field solvers is that the equilibria converges very quickly. Therefore, VMEC continues to remain a robust equilibrium solver which delivers equilibria quickly, which can then be used to study effects of such equilibria on various physical situations such as fast particle dynamics and neoclassical physics. An example can be seen in the Fig. (2.2), where a JET-like 3D equilibrium with a strong saturated 1/1 internal kink mode is shown, with the convergence of a time-invariant $m = 1, n = 1$ mode can be seen in the mode-number maps in Fig. (2.3).

We describe the variational MHD model used by VMEC to compute the MHD equilibria and show its equivalence to the ideal MHD model described in the previous section. This variational MHD equilibrium model has recently been used to compute axisymmetric equilibria with toroidal flow [Cooper et al., 2014], and also has been used to compute 3D helical-core equilibria without flows [Cooper et al., 2015]. It is put in text here as a reference for future students.

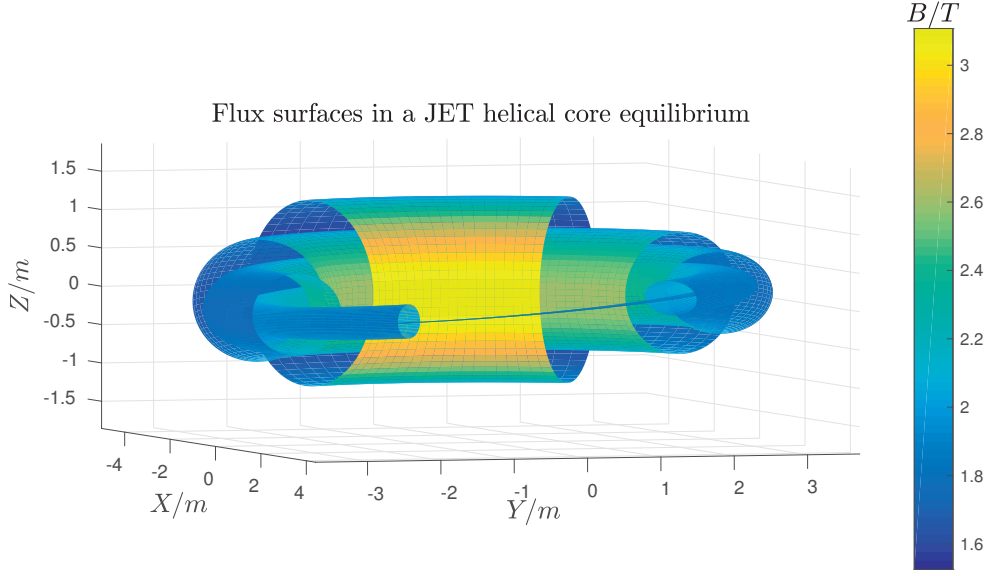


Figure 2.2 – An example of a JET like helical core equilibrium obtained with VMEC. The contours are surfaces of constant pressure, and the shade refers to the magnetic field intensity B . Notice how the axis is helically distorted in comparison to the last closed flux surface.

2.2.1 Equilibrium Without Flows

To obtain an ideal MHD equilibrium without flows, one starts by varying the MHD free energy with respect to an artificial time parameter t . The energy functional W is given by

$$W = \int \int \int ds du dv \sqrt{g} \left(\frac{B^2}{2} + \frac{\mu_0 p(s)}{\Gamma - 1} \right) \quad (2.22)$$

where (s, u, v) are the radial and angular flux-coordinates varied in VMEC, B is the modulus of the magnetic field, $p \equiv p(s)$ is the pressure varying only with the radial variable s , and Γ is the adiabatic index. The coordinates (s, u, v) represent the VMEC magnetic flux coordinates, which are not straight-field like coordinates. Instead the variables are chosen to provide adequate resolution in the radial and angular directions to aid spectral decomposition techniques. In essence, VMEC numerically solves for a 1 – 1 mapping between (R, Z, ϕ) and (s, u, v) , and for that reason $v \equiv \phi$. VMEC coordinates are flux-coordinates meaning that the lines of magnetic field and current lie on the surfaces with constant s .

Because of the form of the adiabatic closure condition on MHD $d/dt(p\rho^\Gamma) = 0$, one can prescribe the pressure to be of the form

$$p(s) = \frac{f(s)}{\langle f(s) \rangle^\Gamma} \quad (2.23)$$

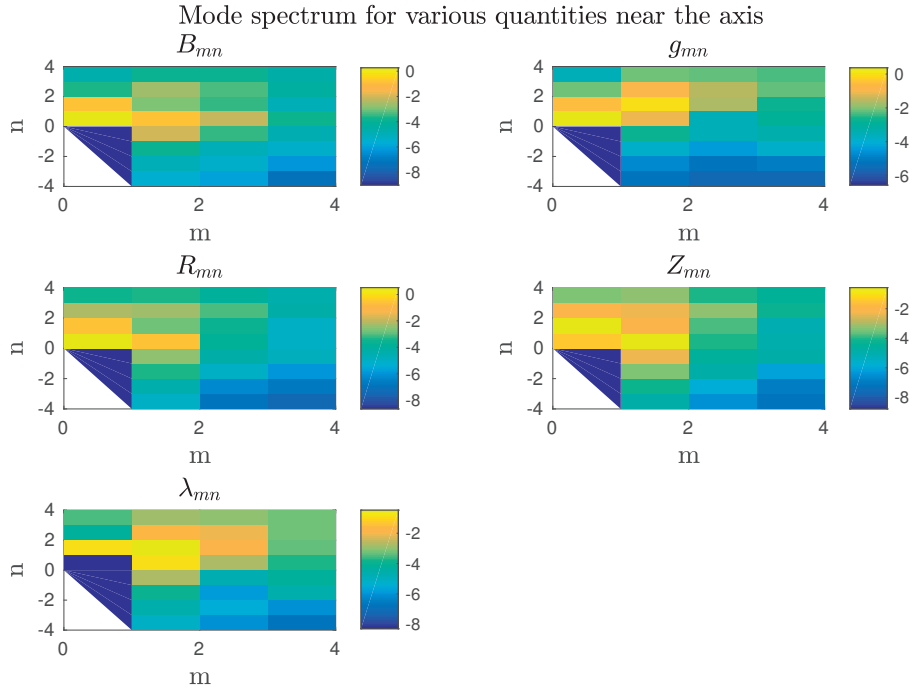


Figure 2.3 – The mode spectrum for the helical core obtained in Fig. (2.2). The colour scale is logarithmic with respect to the largest mode-value. One can see that the spectrum is converged and does not need more modes for resolving the 1/1 mode.

2.2. VMEC and the Variational Formulation with Flows

where the angle brackets $\langle \rangle$ represent a flux-surface average $\langle f(s) \rangle = \int \int dudv \sqrt{g} f(s)$. With this choice of the form of pressure, on varying the energy functional against an artificial time parameter t , one obtains a first variation of the form

$$\frac{dW}{dt} = \int \int \int ds dudv \frac{\partial}{\partial t} \left(\frac{\sqrt{g} B^2}{2} \right) - \mu_0 \int ds \frac{f(s)}{\langle f(s) \rangle^\Gamma} \int \int dudv \frac{\partial \sqrt{g}}{\partial t}. \quad (2.24)$$

where λ is the generating function which defines the transformation of the angular coordinates to VMEC coordinates. Firstly, $\tilde{\lambda}$ is a modified magnetic flux, periodic in u and v , defined as

$$\tilde{\lambda}(s, u, v) = -\Psi'(s)v + \Phi'(s)u + \lambda(s, u, v) \quad (2.25)$$

where Ψ' and ϕ' are magnetic potentials, such that the magnetic Gauss' law $\nabla \cdot \mathbf{B} = 0$ can be satisfied as follows

$$\sqrt{g} B^u = -\frac{\partial \tilde{\lambda}}{\partial v}, \quad \sqrt{g} B^v = \frac{\partial \tilde{\lambda}}{\partial u}, \quad (2.26)$$

which implies

$$\sqrt{g} B^u = \Psi'(s) - \frac{\partial \lambda}{\partial v}, \quad \sqrt{g} B^v = \Phi'(s) + \frac{\partial \lambda}{\partial u}. \quad (2.27)$$

After the calculation of the derivative terms inside the integral, one can express the first variation as

$$\begin{aligned} \frac{dW}{dt} &= - \int \int \int ds dudv \left(\mu_0 F_R \frac{\partial R}{\partial t} + \mu_0 F_Z \frac{\partial Z}{\partial t} + \mu_0 F_\lambda \frac{\partial \lambda}{\partial t} \right) \\ &\quad - \int \int_{s=1} dudv R \left(\mu_0 p + \frac{B^2}{2} \right) \left(\frac{\partial R}{\partial u} \frac{\partial Z}{\partial t} - \frac{\partial Z}{\partial u} \frac{\partial R}{\partial t} \right) \end{aligned} \quad (2.28)$$

where the second integral is the free-energy term in the boundary. For a chosen fixed-boundary, the second-term is zero, but for magnetic fields arising from coil specifications, this is a non-zero term contributing to total variation on the energy functional W . The minimization towards an energy state is obtained by advancing

$$\frac{\partial R}{\partial t} = \mu_0 F_R, \quad \frac{\partial Z}{\partial t} = \mu_0 F_Z, \quad \frac{\partial \lambda}{\partial t} = \mu_0 F_\lambda, \quad (2.29)$$

for which the energy functional remains negative definite. The forces $\mu_0 F_R$, $\mu_0 F_Z$ and F_λ are

Chapter 2. Equilibrium Theory, Guiding-Center Orbits and Neoclassical Theory with Flows

as follows

$$\begin{aligned}\mu_0 F_R &= \frac{\partial}{\partial s} \left[\left(\mu_0 p + \frac{B^2}{2} \right) R \frac{\partial Z}{\partial u} \right] - \frac{\partial}{\partial u} \left[\left(\mu_0 p + \frac{B^2}{2} \right) R \frac{\partial Z}{\partial s} \right] \\ &+ \frac{\partial}{\partial u} [\sqrt{g} B^u (\mathbf{B} \cdot \nabla R)] + \frac{\partial}{\partial v} [\sqrt{g} B^v (\mathbf{B} \cdot \nabla R)] \\ &+ \frac{\sqrt{g}}{R} \left[\mu_0 p + \frac{B^2}{2} - R^2 (B^v)^2 \right],\end{aligned}\tag{2.30}$$

$$\begin{aligned}\mu_0 F_Z &= \frac{\partial}{\partial u} \left[\left(\mu_0 p + \frac{B^2}{2} \right) R \frac{\partial R}{\partial s} \right] - \frac{\partial}{\partial s} \left[\left(\mu_0 p + \frac{B^2}{2} \right) R \frac{\partial R}{\partial u} \right] \\ &+ \frac{\partial}{\partial u} [\sqrt{g} B^u (\mathbf{B} \cdot \nabla Z)] + \frac{\partial}{\partial v} [\sqrt{g} B^v (\mathbf{B} \cdot \nabla Z)],\end{aligned}\tag{2.31}$$

$$\mu_0 F_\lambda = \frac{\partial B_v}{\partial u} - \frac{\partial B_u}{\partial v}.\tag{2.32}$$

The latter equation is the condition that the currents lie on flux-surfaces.

One can show, following the ideal MHD force balance equation

$$\mu_0 \mathbf{F} = \mu_0 \nabla p - (\nabla \times \mathbf{B}) \times \mathbf{B},\tag{2.33}$$

one can straightforwardly show that the force balance in the radial direction $\mu_0 \mathbf{F} \cdot \nabla v \times \nabla Z$, in the azimuthal direction $\mu_0 \mathbf{F} \cdot \nabla R \times \nabla v$ and along the magnetic geodesics $\mu_0 \sqrt{g} \mathbf{F} \cdot \mathbf{B} \times \nabla s / B^2$ correspond to the terms $\mu_0 F_R$, $\mu_0 F_Z$ and $\mu_0 F_\lambda$ obtained in the equation above.

2.2.2 Axisymmetric Equilibrium with Purely Toroidal Flows

Following [Maschke and Perrin, 1980], one can generalize the energy functional in axisymmetry by extending the pressure to have a dependence on R in addition to the radial variable s , as seen in Eq. (2.16)

$$W = \int \int \int ds du dv \left(\frac{B^2}{2} + \frac{\mu_0 p(s, R)}{\Gamma - 1} \right).\tag{2.34}$$

We note that this is an exact model for axisymmetry where the energy functional corresponds exactly to ideal MHD with flows in axisymmetry. One can notice that the variational form of the pressure is similar to the one obtained earlier in Eq. (2.16). Continuing along this model,

the form of the pressure is chosen to be

$$p(s, R) = \frac{f(s, R)}{\langle f(s, R) \rangle^\Gamma} \quad (2.35)$$

with the averaging being in the same fashion as before. On calculating the first variation, compared to Eq. (2.28) we will now have an additional term arising from the radial dependence of f

$$\begin{aligned} \frac{dW}{dt} &= \int \int \int ds du dv \frac{\partial}{\partial t} \left(\frac{\sqrt{g} B^2}{2} \right) \\ &- \mu_0 \int ds \frac{f(s, R)}{\langle f(s, R) \rangle^\Gamma} \int \int du dv \frac{\partial \sqrt{g}}{\partial t} \\ &- \mu_0 \int \int \int ds du dv \sqrt{g} \frac{\langle f(s, R) \rangle^\Gamma}{\langle f(s, R) \rangle^\Gamma} \frac{\partial p}{\partial R} \frac{\partial R}{\partial t}. \end{aligned} \quad (2.36)$$

Only the radial force term $\mu_0 F_R$ would be affected by the third term in the integral, taking the form

$$\begin{aligned} \mu_0 F_R &= \frac{\partial}{\partial s} \left[\left(\mu_0 p + \frac{B^2}{2} \right) R \frac{\partial Z}{\partial u} \right] - \frac{\partial}{\partial u} \left[\left(\mu_0 p + \frac{B^2}{2} \right) R \frac{\partial Z}{\partial s} \right] \\ &+ \frac{\partial}{\partial u} [\sqrt{g} B^u (\mathbf{B} \cdot \nabla R)] + \frac{\partial}{\partial v} [\sqrt{g} B^v (\mathbf{B} \cdot \nabla R)] \\ &+ \frac{\sqrt{g}}{R} \left[\mu_0 p + \frac{B^2}{2} - R^2 (B^v)^2 + R \frac{\partial p}{\partial R} \right] \end{aligned} \quad (2.37)$$

with the other two force terms not being affected by the inclusion the radially dependent pressure term. Imposing the pressure to be of the form $p \equiv p(s, R)$, we proceed to calculate the contribution of the additional term in $\mu_0 F_R$. The radial force can be written as:

$$\mu_0 F_R = \mu_0 F_R|_{static} + \frac{\sqrt{g}}{R} \left(R \frac{\partial p}{\partial R} \right) \quad (2.38)$$

and where

$$\frac{\sqrt{g}}{R} \left(R \frac{\partial p}{\partial R} \right) \rightarrow \frac{\sqrt{g}}{R} \left(\frac{m_i \Omega^2 R^2}{2T} p(s, R) \right). \quad (2.39)$$

Recalling that $p = 2nT$, and $\rho = m_i n$, we have

$$\frac{\sqrt{g}}{R} \left(R \frac{\partial p}{\partial R} \right) \rightarrow \frac{\sqrt{g}}{R} (\rho \Omega^2 R^2). \quad (2.40)$$

Chapter 2. Equilibrium Theory, Guiding-Center Orbits and Neoclassical Theory with Flows

Therefore, the radial force balance is of the form

$$\mu_0 F_R = \mu_0 F_R|_{static} + \frac{\sqrt{g}}{R} (\rho \Omega^2 R^2). \quad (2.41)$$

The second term in the RHS is equivalent to the $\mu_0 \nabla v \times \nabla Z$ component of $\rho \mathbf{U}_0 \cdot \nabla \mathbf{U}_0 = \mu_0 \rho R \Omega^2 \nabla R$, thus satisfying the axisymmetric version of the force balance equation. Thus, the axisymmetric equilibrium obtained through variational principle is completely consistent with the ideal MHD with flows.

2.2.3 Limitations of 3D Equilibria with Purely Toroidal Flows

The equilibrium obtained in the previous sections are either valid for 3D without flows or axisymmetry with flows. But it has been seen in the past as an approximately valid model for 3D with flows when the ideal MHD response to 3D perturbations is weak [Cooper et al., 2014, Cooper et al., 2015]. We now set out to look at the validity of the model for 3D magnetic geometries with purely toroidal flows. We assume here that the axisymmetric energy functional Eq. 2.34 is valid for 3D while imposing toroidal flow. Assuming Ω is flux-surface function or equivalently, assuming that the flow is chosen to be purely toroidal, the force balance equation arising from the flow becomes

$$\mu_0 \rho \mathbf{U} \cdot \nabla \mathbf{U} = \mu_0 \rho R \Omega^2 \nabla R + \mu_0 \rho R^2 g^{s\phi} \Omega \Omega' \mathbf{e}_\phi \quad (2.42)$$

where R now has a 3D dependence. As we have observed, on a radial projection $\mu_0 \rho \mathbf{U} \cdot \nabla \mathbf{U} \cdot \nabla v \times \nabla Z$, we reproduce the extra term in the radial force balance equation above. However, the second term in the RHS cannot be obtained from the form of the energy functional used. Therefore, the restriction on the equilibrium becomes

$$\begin{aligned} \Omega'(s) &\sim 0, \text{ where } R^2 g^{s\phi} \neq 0, \text{ strongly 3D regions} \\ R^2 g^{s\phi} &\sim 0, \text{ where } \Omega' \neq 0, \text{ for high flow shear regions.} \end{aligned}$$

These constraints can be nearly satisfied for a rotating equilibrium with a saturated 1/1 internal kink, of the flow in the helical region is unsheared.

However, a more important limitation of the equilibrium is the incompressibility condition $\nabla \cdot \mathbf{U}_0 = 0$ which must be satisfied. With the purely toroidal flow, from the continuity equation, it is required that

$$U^\phi R^2 g^{s\phi} \frac{\partial B_\phi}{\partial \phi} = 0 \quad (2.43)$$

must also be satisfied. In regions of strong 3D, where the metric element $g^{s\phi} \neq 0$, the variation in the toroidal field with the toroidal angle ϕ is generally non-negligible. That is, the flow itself

must be zero in case of strong 3D. In the case of a saturated helical core with strong radial displacements, this condition is not satisfied.

For pragmatic reasons, we must also take into account that, for a tokamak like JET, the Mach number of the background plasma is relatively low, and hence the centrifugal effects on the main ions are weak. Therefore, for testing cases with 3D, we can choose to use an MHD equilibrium without the flow, as it won't differ significantly in terms of magnetics from a 3D MHD equilibrium incorporating flow. This is a caveat central to this thesis. We will, however, include centrifugal effects on the heavy impurity ions.

2.3 Plasma Flows and Ordering

In this section, we describe the general theory of plasma flows, as is also applicable to 3D magnetic geometries [Helander, 2014, Shaing et al., 2015]. The major flows in the plasma, for the species j , can be expressed as follows following the Larmor radius ordering

$$\mathbf{U}_j = \mathbf{U}_{0,j} + \mathbf{U}_{1,j}, \quad (2.44)$$

where these flows can be separated into their parallel and perpendicular components

$$\mathbf{U}_{\perp,j} = \mathbf{U}_{0\perp,j} + \mathbf{U}_{1\perp,j}, \quad (2.45)$$

$$\mathbf{U}_{\parallel,j} = \mathbf{U}_{0\parallel,j} + \mathbf{U}_{1\parallel,j}. \quad (2.46)$$

The zeroth order flow $\mathbf{U}_{0,j}$ arises from the presence of a zeroth-order electric potential Φ_0 and the first order flow arises from the presence of pressure gradients ∇p_j and the first-order electric potential Φ_1 . The perpendicular components can be written as

$$\mathbf{U}_{0\perp,j} = \frac{\mathbf{E}_0 \times \mathbf{B}}{B^2} \quad (2.47)$$

$$\mathbf{U}_{1\perp,j} = \frac{\mathbf{B} \times \nabla p_j}{n_j Z_j e B^2} + \frac{\mathbf{E}_1 \times \mathbf{B}}{B^2}. \quad (2.48)$$

where $\mathbf{E}_0 = \nabla \Phi_0$ and $\mathbf{E}_1 = \nabla \Phi_1$. The flows are considered to be incompressible at all orders, therefore we have the constraints

$$\nabla \cdot \mathbf{U}_{0,j} = 0 = \nabla \cdot \mathbf{U}_{1,j}. \quad (2.49)$$

Thus the parallel flows at all orders can be obtained from the solution to the continuity equation. However, it can be noticed that additional constraints are required to determine the respective parallel flows completely.

Chapter 2. Equilibrium Theory, Guiding-Center Orbits and Neoclassical Theory with Flows

2.3.1 Lowest-Order Flows \mathbf{U}_0

For the zeroth order flow $\mathbf{U}_{0,j}$, we start from the following expressions of constraints

$$\mathbf{b} \cdot \nabla T_j = 0 \quad (2.50)$$

$$\nabla \cdot (n_j \mathbf{U}_{0,j}) = 0 \quad (2.51)$$

$$\mathbf{U}_{0,j} \cdot \nabla \left(\ln n_j - \frac{3}{2} \ln T_j \right) = 0 \quad (2.52)$$

$$\mathbf{b} \cdot \nabla \mathbf{U}_{0,j} \cdot \mathbf{b} - \frac{1}{3} \nabla \cdot \mathbf{U}_{0,j} = 0, \quad (2.53)$$

$$\mathbf{b} \cdot \left(\nabla \ln n_j + \frac{e \nabla \Phi_1}{T} + \frac{m}{T} \mathbf{U}_{0,j} \cdot \nabla \mathbf{U}_{0,j} \right) = 0. \quad (2.54)$$

These neoclassical constraints arise from the quasi-stationary solution of the drift-kinetic equation with plasma flows [Hinton and Hazeltine, 1976]. Equation (2.50) is the isothermal condition, which states that the temperature is a flux-surface function $T_j \equiv T_j(\psi)$. Assuming n_j is a flux-surface function, equation (2.51) reduces to the continuity equation. The equations (2.52-2.54) relate the flows to the magnetic geometry. For axisymmetry, it can be shown that the lowest-order poloidal velocity vanishes, $U_{0\theta,j} = 0$, and the flow is purely toroidal of the form:

$$\mathbf{U}_{0,j} = \partial_\psi \Phi_0 \mathbf{e}_\phi = \partial_\psi \Phi_0 R^2 \nabla \phi \quad (2.55)$$

where the radial potential gradient $\partial_\psi \Phi_0$ can be considered as the toroidal angular velocity. For 3D, the application of the constraints leads to a flow which lies along the intersection of the contours of the flux-surfaces and the contours of magnetic field strength B [Helander, 2014]

$$\mathbf{U}_{0,j} = \partial_\psi \Phi_0 \frac{\nabla B \times \nabla \psi}{\mathbf{B} \cdot \nabla B}. \quad (2.56)$$

2.4 Higher-order Flow \mathbf{U}_1

Moving on to the first-order flows, $\mathbf{U}_{1,j}$, we reframe this flow and drop the $\nabla \Phi_1$ dependent flow term for two reasons. Firstly, as will be seen later, we only consider the higher-order flow to provide the correct difference in velocities between the impurity particle and background ions, for the $\nabla \Phi_1$ component remains the same for both species. Secondly, the component is dependent generally on (ψ, θ, ϕ) for 3D equilibria and the inversion with such a 3D dependence is beyond the scope of this thesis and can be considered as an avenue to extend the work.

We again start from the perpendicular flow component $\mathbf{U}_{1\perp,i}$ of Eq. (2.48), dropping the contribution from Φ_1 for reasons given above.

$$\mathbf{U}_{1\perp,i} = \frac{\mathbf{B} \times \nabla p_i}{n_i Z_i e B^2}. \quad (2.57)$$

This perpendicular component can be recognized as the diamagnetic flow. The parallel component can again be obtained by solution of the continuity equation $\nabla \cdot \mathbf{U}_{1,j} = 0$. We start by assuming that the pressure p_i to the leading-order is a flux-surface function, such that

$$\nabla \cdot (\mathbf{U}_{1\parallel,i} + \mathbf{U}_{1\perp,i}) = 0 \implies \nabla \cdot \left(\frac{U_{1\parallel,i} \mathbf{B}}{B} \right) = -\nabla \cdot \left(\frac{\mathbf{B} \times \nabla \psi}{B^2} \frac{p'_i}{n_i Z_i e} \right). \quad (2.58)$$

Using chain rule on both sides of the equation, and using the expressions for the magnetic Gauss' law $\nabla \cdot \mathbf{B} = 0$, the Faraday law $\nabla \times \mathbf{B} = \mu_0 \mathbf{J}$ and that the lines of current lie along the flux-surface $\mathbf{J} \cdot \nabla \psi = 0$, we transform the expression above into

$$\mathbf{B} \cdot \nabla \left(\frac{n_i Z_i e}{p'_i} \frac{U_{1\parallel,i} B}{B^2} \right) = \mathbf{B} \times \nabla \psi \cdot \nabla \left(\frac{1}{B^2} \right). \quad (2.59)$$

With a difference in a constant of integration, a flux-surface function yet to be defined, the above equation can be reformulated as

$$\mathbf{B} \cdot \nabla \left(\frac{g_2}{B^2} \right) = \mathbf{B} \times \nabla \psi \cdot \nabla \left(\frac{1}{B^2} \right). \quad (2.60)$$

With the condition that $\langle g_2 B \rangle = 0$ [Hinton and Hazeltine, 1976, Helander, 2014], the solution to the above equation will yield the Pfirsch-Schlüter return flows [Nakajima and Okamoto, 1992, Helander, 2014]. Additional averaged flows, such as the bootstrap flows can be included to provide the full flow description, which leads to the solution for the parallel flows being

$$U_{1\parallel,i} = - \left(\frac{g_2}{B} - \frac{B}{\langle B^2 \rangle} \langle g_2 \rangle \right) \frac{p'_i}{Z_i e n_i} + \frac{B}{\langle B^2 \rangle} \langle U_{1\parallel,i} B \rangle. \quad (2.61)$$

Expression (2.60) is fairly straightforward to solve for g_2 if the magnetic field were specified in straight field-line coordinates. (E.g., one can make a Fourier transform of both the sides of the equation and obtain the $\mathbf{B} \cdot \nabla = \nabla_{\parallel}$ parameter as $m\Psi' - n\Phi'$, if (Ψ, Θ, Φ) are in Boozer coordinates).

The bootstrap flow velocity $\langle U_{1\parallel,i} B \rangle$ could be obtained by a neoclassical code such as SFINCS [Landreman et al., 2015, Mollén et al., 2014], which is computationally expensive however. A simpler analytical prescription for the bootstrap flow velocity $\langle U_{1\parallel,i} B \rangle$ for 3D magnetic geometry can be obtained through the Shaing-Callen model as well [Shaing et al., 2015] in different regimes, depending on which the background plasma is in. The expression for the parallel velocity in different regimes is given by

$$\frac{\langle U_{1\parallel,i} B \rangle}{\langle B^2 \rangle} = -G(\psi) \frac{T_i}{e_i \langle B^2 \rangle} \left(\frac{\partial}{\partial \psi} \ln p_i + \frac{\mu_{2i}}{\mu_{1i}} \frac{\partial}{\partial \psi} \ln T_i \right) \quad (2.62)$$

where $G(\psi)$ is a geometrical factor in the relevant regime of concern. The geometrical factor $G \equiv G(\psi)$ is calculated through averaging over the entire 3D field. The coefficients μ_{1i} and μ_{2i} are analytically determined in terms of the neoclassical viscosity tensor coefficients. The ratio

Chapter 2. Equilibrium Theory, Guiding-Center Orbits and Neoclassical Theory with Flows

μ_{2i}/μ_{1i} is approximately equal to -1.17 in the collisionless banana regime and to 1.69 in the Pfirsch-Schlüter regime.

We proceed to state the geometrical factors $G(\psi)$ for the banana regime and the Pfirsch-Schlüter regime. The geometrical factor $G_b(\psi)$ is computed in the $1/\nu$ (collisionless) regime as

$$G_b(\psi) = \frac{1}{f_t} \left\{ \langle g_2 \rangle - \frac{3}{4} \frac{\langle B^2 \rangle}{B_{max}^2} \int_0^1 \frac{\langle g_4 \rangle}{\langle g_1 \rangle} \lambda d\lambda \right\}. \quad (2.63)$$

This expression will be used in the computation of the bootstrap current later. The same factor can be used to describe the background common flow, as the geometrical scaling remains the same. $G_{PS}(\psi)$ is a geometrical factor in the Pfirsch-Schlüter regime [Shaing and Callen, 1983, Shaing et al., 1986a, Watanabe et al., 1992, Johnson et al., 1999]

$$G_{PS}(\psi) = \langle g_2 \rangle - \frac{\langle B^2 \rangle}{\langle (\hat{b} \cdot \nabla B)^2 \rangle} \left\langle \frac{(\hat{b} \cdot \nabla B)(\hat{b} \cdot \nabla g_2)}{B^2} \right\rangle, \quad (2.64)$$

where g_1 , g_2 and g_4 are defined later in equations (2.132-2.133). As one can notice, the geometrical factor is slightly smaller in the Pfirsch-Schlüter regime than in the banana regime. Correspondingly, the electron bootstrap current is also negligible in the Pfirsch-Schlüter regime [Shaing et al., 2015]. With this, the description of the higher-order flows is complete. The treatment of flows arising from the presence of a higher-order electric-field $\nabla \Phi_1$, which is not a flux-surface function in general, as mentioned before, is beyond the scope of the current thesis.

2.5 Guiding-Center formulation

Particle orbits in an MHD equilibrium as described by the previous sections can be developed with the help of the guiding-center formulation. In this thesis, we will follow the orbits of impurity ions in the presence of collisions. Since plasma rotation is of fundamental importance to this thesis, the formulation must also allow for drifts induced by the toroidal flow of the plasma. For this reason, we follow the guiding-center prescription suggested by Ref. [Brizard, 1995], decomposing the particle guiding center velocity \mathbf{V}_{gc} into flow and thermal components in the following manner:

$$\mathbf{V}_{gc,j} = \mathbf{U}_{0,j} + \mathbf{w}_j, \quad (2.65)$$

where $\mathbf{U}_{0,j}$ is the total leading-order ensemble flow velocity of the particle, and \mathbf{w}_j is the thermal component of the velocity of the particle of species j . The advantage of the formulation in Ref. [Brizard, 1995], over guiding-center formulations which explicitly solve for the orbits in the rotating frame [Peeters et al., 2009] is that this formulation allows us to incorporate a shear in the flow profile, which is essential for modeling cases which correspond closely to actual experimental conditions. (In the scope of the thesis, however, we do not apply a sheared

flow). Most importantly, the collisions which come through a collision operator need to be in the rest frame. Another advantage of this velocity decomposition is that the collisions can be directly imposed on the thermal part of the velocities, which are, by definition, in the rest frame of the plasma. Furthermore, the parallel and perpendicular dynamics can be resolved by further splitting the species flow and the thermal velocity into its parallel ($U_{0\parallel,j}, w_{\parallel,j}$) and perpendicular ($\mathbf{U}_{0\perp,j}, \mathbf{w}_{\perp,j}$) components.

The independent phase-space variables are chosen to be $(\mathbf{X}, \rho_{\parallel,j}, \mu_j)$, where \mathbf{X} is the guiding-center position, $\mu = mw_{\perp,j}^2/2B$ is the magnetic moment, and $\rho_{\parallel,j}$, the parallel gyroradius is defined as

$$\rho_{\parallel,j} = \frac{m_j}{Z_j e} \frac{w_{\parallel,j}}{B}. \quad (2.66)$$

The redefinition of the parallel variable in terms of $\rho_{\parallel,j}$ instead of $w_{\parallel,j}$ makes the guiding-center derivation more convenient. The charge-normalized Hamiltonian and Lagrangian are given by

$$\frac{\mathcal{H}_{gc}}{Z_j e} = h = \Phi + \frac{\mu}{Z_j e} B + \frac{1}{2} \frac{m_j}{Z_j e} \left(\mathbf{U}_{0,j} + \frac{Z_j e}{m_j} \rho_{\parallel,j} \mathbf{B} \right)^2, \quad (2.67)$$

and

$$\frac{\mathcal{L}_{gc}}{q} = l = \mathbf{A}^* \cdot \dot{\mathbf{X}} - h, \quad (2.68)$$

where we define a modified vector potential \mathbf{A}^* as

$$\mathbf{A}^* = \mathbf{A} + \frac{m_j}{Z_j e} \mathbf{U}_{0,j} + \rho_{\parallel,j} \mathbf{B}. \quad (2.69)$$

This consequently leads to the definition of a modified magnetic field \mathbf{B}^*

$$\mathbf{B}^* = \nabla \times \mathbf{A}^* = \mathbf{B} + \rho_{\parallel,j} \nabla \times \mathbf{B} + \frac{m_j}{Z_j e} \nabla \times \mathbf{U}_{0,j}. \quad (2.70)$$

These * modified potentials and flows ensure the conservation of the drift-kinetic plasma distribution function to the first-order [Brizard, 1995, Littlejohn, 1983]. One can now obtain the canonical equations of motion through the formal solution of the minimization of the variation of the Hamiltonian [Littlejohn, 1983, Brizard, 1995, Cary and Brizard, 2009]. The final expression is

$$\dot{z}^\alpha = [\Omega^{-1}]^{\alpha\beta} (\partial_\beta h + \partial_t A_\beta^*), \quad (2.71)$$

where z is used to denote the independent phase-space variables, where also (α, β) can be any of the independent phase-space variables $(\mathbf{X}_j, \rho_{\parallel,j}, \mu_j)$. The Lagrange bracket $\Omega_{\alpha\beta}$ is defined

Chapter 2. Equilibrium Theory, Guiding-Center Orbits and Neoclassical Theory with Flows

to be

$$\Omega_{\alpha\beta} = \partial_\alpha A_\beta^* + \partial_\beta A_\alpha^*, \quad (2.72)$$

which can be shown to be

$$\Omega_{\alpha\beta} = \begin{pmatrix} 0 & B_q \\ -B_p & \sqrt{g} B^{*r} \epsilon_{rpq} \end{pmatrix}, \quad (2.73)$$

where (p, q, r) is used to denote the configuration space components of \mathbf{X} . ϵ_{rpq} refers to the Levi-Civita tensor. The inverse of $\Omega_{\alpha\beta}$ is

$$[\Omega^{-1}]^{\alpha\beta} = \frac{1}{B_p B^{*p}} \begin{pmatrix} 0 & -B^{*q} \\ B^{*q} & \frac{B_r}{\sqrt{g}} \epsilon^{rpq} \end{pmatrix}. \quad (2.74)$$

From Eq. (2.71)-(2.74), we get

$$\partial_{\rho_{\parallel,j}} h = U_{0\parallel,j} B + \frac{Z_j e}{m_j} \rho_{\parallel,j} B^2 \quad (2.75)$$

and

$$\partial_p h = -E_p^* = -E_p + \left(\frac{\mu}{Z_j e} + \frac{Z_j e}{m_j} \rho_{\parallel,j}^2 B \right) \partial_p B + \frac{m_j}{Z_j e} \partial_p (U_{0,j}^2) + \rho_{\parallel,j} \partial_p (U_{0\parallel,j} B), \quad (2.76)$$

respectively, where E_p^* is the electric field with thermal and centrifugal corrections. The modified electric field \mathbf{E}^* can be written in vector form as

$$\mathbf{E}^* = \mathbf{E} - \left(\frac{\mu}{Z_j e} + \frac{Z_j e}{m_j} \rho_{\parallel,j}^2 B \right) \nabla B - \frac{1}{2} \frac{m_j}{Z_j e} \nabla (U_{0,j}^2) - \rho_{\parallel,j} \nabla (\mathbf{U}_{0,j} \cdot \mathbf{B}), \quad (2.77)$$

where $\mathbf{E} = -\nabla \Phi_0 - \nabla \Phi_1$. Φ_0 is the electric potential responsible for driving the toroidal flow, and Φ_1 is the higher-order centrifugal correction as explained shortly below. The equations of motion are obtained by substituting equations (2.74)-(2.75) in equation (2.71),

$$\begin{pmatrix} \rho_{\parallel,j} \\ X_j^p \end{pmatrix} = \frac{1}{B_p B^{*p}} \begin{pmatrix} 0 & -B^{*q} \\ B^{*q} & \frac{B_r}{\sqrt{g}} \epsilon^{rpq} \end{pmatrix} \begin{pmatrix} U_{0\parallel,j} B + \frac{Z_j e}{m_j} \rho_{\parallel,j} B^2 \\ -E_q^* \end{pmatrix}. \quad (2.78)$$

Finally, the relevant guiding-center equations are

$$\rho_{\parallel,j} \dot{=} \frac{B^{*q} E_q^*}{B_p B^{*p}} = \frac{\mathbf{E}^* \cdot \mathbf{B}^*}{\mathbf{B} \cdot \mathbf{B}^*} \quad (2.79)$$

$$\begin{aligned} \dot{X}_j^p &= \left(U_{0\parallel,j} + \frac{Z_j e}{m_j} \rho_{\parallel,j} B \right) \frac{B B^{*p}}{B_p B^{*p}} + \frac{\epsilon^{pqr}}{\sqrt{g}} \frac{B_r E_q^*}{B_p B^{*p}} \\ &= \left[\left(U_{0\parallel,j} + \frac{Z_j e}{m_j} \rho_{\parallel,j} B \right) \frac{\mathbf{B}^*}{\mathbf{B} \cdot \mathbf{B}^*} + \frac{\mathbf{E}^* \times \mathbf{b}}{\mathbf{B} \cdot \mathbf{B}^*} \right]^p. \end{aligned} \quad (2.80)$$

We can see that the effects of plasma rotation are now incorporated in the guiding-center equations, which are coded into VENUS-LEVIS. VENUS-LEVIS solves Eqns. (2.80) using the 4th-order Runge-Kutta (RK4) algorithm with a heuristic adaptative time-stepping scheme [Pfefferlé et al., 2014a]. The adaptative RK4 scheme has been shown to preserve the energy and toroidal momentum (for axisymmetric equilibria) to machine precision. We proceed to describe in detail the individual terms implemented in VENUS-LEVIS.

2.5.1 Implementation of the Guiding-Center Equations in VENUS-LEVIS

In this subsection, we describe the implementation of the guiding-center equations used in VENUS-LEVIS. First, we start by choosing a form for the toroidal flow $\mathbf{U}_{0,j}$. The most general solution for $\mathbf{U}_{0,j}$ is obtained by inverting the continuity equation $\nabla \cdot \mathbf{U}_{0,j} = 0$ and can be written, assuming the lowest order electric potential Φ_0 is a flux-surface function, in the Pfirsch-Schlüter regime [Shaing and Callen, 1983] as

$$\mathbf{U}_{0,i} = \left\{ - \left(\frac{g_2}{B} - \frac{B}{\langle B^2 \rangle} \langle g_2 \rangle \right) - \frac{B}{\langle B^2 \rangle} G_{PS} + \frac{B}{\langle B^2 \rangle} U_{0\parallel,i,bc} \right\} \Phi_0' \mathbf{b} + \frac{\mathbf{B} \times \nabla \psi}{B^2} \Phi_0', \quad (2.81)$$

where $U_{0\parallel,i,bc}$ is the boundary condition. This expression is valid for 3D magnetic geometry in general. Note however, that $U_{0\parallel,i,bc}$ is zero in the case of axisymmetric magnetic fields [Shaing and Callen, 1983]. Currently, we choose a value of $U_{0\parallel,i,bc}$ to impose a purely toroidal flow. The leading-order flow is then imposed as

$$\mathbf{U}_0 = \Omega \mathbf{e}_\phi = \Omega(\psi) R^2 \nabla \phi, \quad (2.82)$$

where $\Omega(\psi)$ is the angular velocity. This makes the computations of gradients of the flow in Eq. (2.80) much simpler. (Again, It is important to note that the leading-order flow in its most general form is not purely toroidal for 3D equilibrium fields, but actually lies along the intersection of the contours of ψ and B [Helander, 2014]. The treatment of a complex flow of such nature is out of the scope of the current thesis, and poses a possible way to extend the work further.)

Under the imposition of a purely toroidal ensemble flow, the guiding-center definitions for

Chapter 2. Equilibrium Theory, Guiding-Center Orbits and Neoclassical Theory with Flows

the modified fields, Eqs. (2.69), (2.70) and (2.77) can be expressed as

$$\mathbf{A}^* = \mathbf{A} + \rho_{\parallel,j} \mathbf{B} + \frac{m_j}{Z_j e} \mathbf{U}_{0,j}, \quad (2.83)$$

$$\mathbf{B}^* = \mathbf{B} + \rho_{\parallel,j} \nabla \times \mathbf{B} + \frac{m_j}{Z_j e} \nabla \times \mathbf{U}_{0,j}, \text{ and} \quad (2.84)$$

$$\mathbf{E}^* = \mathbf{E} - \left(\frac{\mu_j}{Z_j e} + w_{\parallel,j} \rho_{\parallel,j} \right) \nabla B - \frac{1}{2} \frac{m_j}{Z_j e} \nabla (U_{0,j}^2) - \rho_{\parallel,j} \nabla (U_{0,j} B). \quad (2.85)$$

One can see that there are some extra terms in presence of the flow that are not found in the flow-free stationary frame guiding-center equations. Using the form for the flow above, we now proceed to compute those terms. The term $\nabla \times \mathbf{U}_0$ is given by

$$\begin{aligned} \nabla \times \mathbf{U}_{0,j} &= \nabla \times (R^2 \Omega \nabla \phi) \\ &= -\frac{R^2 \Omega}{\sqrt{g}} \left(\frac{1}{\Omega} \frac{\partial \Omega}{\partial \psi} + \frac{2}{R} \frac{\partial R}{\partial \psi} \right) \mathbf{e}_\theta + \frac{2R\Omega}{\sqrt{g}} \frac{\partial R}{\partial \theta} \mathbf{e}_\psi. \end{aligned} \quad (2.86)$$

This expression gives the $\nabla \times \mathbf{U}_0$ in the contravariant form and, if needed, the covariant form can be obtained by vector multiplication with the contravariant metric g^{pq} . The expression (2.86) can be substituted into Eq. (2.70) to complete the description for \mathbf{B}^* .

We expand the terms required to complete the description for \mathbf{E}^* . The electric field is expressed as

$$\mathbf{E} = -\nabla \Phi_0 - \nabla \Phi_1 \quad (2.87)$$

where $-\nabla \Phi_0$ refers to the leading-order electric field responsible for the toroidal flow. From Ohm's law, $\nabla \Phi_0$ can be written as

$$\nabla \Phi_0 = \mathbf{U}_{0,j} \times \mathbf{B} = \sqrt{g} \Omega R^2 \{ (B^\theta g^{\phi\phi} - B^\phi g^{\theta\phi}) \nabla \psi + B^\phi g^{\psi\phi} \nabla \theta - B^\theta g^{\psi\phi} \nabla \phi \} \quad (2.88)$$

where \sqrt{g} is the Jacobian of the coordinate transformation. Next, we have, $|\mathbf{U}_0| = R\Omega$, therefore, we can calculate ∇U_0^2 to be

$$\begin{aligned} \nabla U_{0,j}^2 &= \nabla R^2 \Omega^2 \\ &= 2R^2 \Omega^2 \left[\left(\frac{1}{\Omega} \frac{\partial \Omega}{\partial \psi} + \frac{1}{R} \frac{\partial R}{\partial \psi} \right) \nabla \psi + \frac{1}{R} \frac{\partial R}{\partial \theta} \nabla \theta + \frac{1}{R} \frac{\partial R}{\partial \phi} \nabla \phi \right]. \end{aligned} \quad (2.89)$$

The term $\nabla U_{0,j} B$ can be written as $\nabla (\mathbf{U}_{0,j} \cdot \mathbf{B})$ which can be written as

$$\begin{aligned} \nabla (\mathbf{U}_{0,j} \cdot \mathbf{B}) &= \nabla (\Omega R^2 \nabla \phi \cdot \mathbf{B}) = \nabla \Omega R^2 B^\phi \\ &= R^2 B^\phi \frac{\partial \Omega}{\partial \psi} \nabla \psi + 2\Omega R B^\phi \left(\frac{\partial R}{\partial \psi} \nabla \psi + \frac{\partial R}{\partial \theta} \nabla \theta + \frac{\partial R}{\partial \phi} \nabla \phi \right) + \Omega R^2 \nabla B^\phi. \end{aligned} \quad (2.90)$$

With these calculated values, we may again express the modified fields as

$$\mathbf{A}^* = \mathbf{A} + \rho_{\parallel,j} \mathbf{B} + \frac{m_j}{Z_j e} R^2 \Omega \nabla \phi, \quad (2.91)$$

$$\mathbf{B}^* = \mathbf{B} + \rho_{\parallel,j} \nabla \times \mathbf{B} - \frac{m_j}{Z_j e} \frac{R^2 \Omega}{\sqrt{g}} \left(\frac{1}{\Omega} \frac{\partial \Omega}{\partial \psi} + \frac{2}{R} \frac{\partial R}{\partial \psi} \right) \mathbf{e}_\theta + \frac{m_j}{Z_j e} \frac{2R\Omega}{\sqrt{g}} \frac{\partial R}{\partial \theta} \mathbf{e}_\psi, \text{ and} \quad (2.92)$$

$$\begin{aligned} \mathbf{E}^* = & -\nabla \Phi_1 - \sqrt{g} \Omega R^2 \{ (B^\theta g^{\phi\phi} - B^\phi g^{\theta\phi}) \nabla \psi + B^\phi g^{\psi\phi} \nabla \theta - B^\theta g^{\psi\phi} \nabla \phi \} \\ & - \left(\frac{\mu_j}{Z_j e} + w_{\parallel,j} \rho_{\parallel,j} \right) \nabla B - \frac{m_j \Omega^2 R^2}{Z_j e} \left[\left(\frac{1}{\Omega} \frac{\partial \Omega}{\partial \psi} + \frac{1}{R} \frac{\partial R}{\partial \psi} \right) \nabla \psi + \frac{1}{R} \frac{\partial R}{\partial \theta} \nabla \theta + \frac{1}{R} \frac{\partial R}{\partial \phi} \nabla \phi \right] \\ & - \rho_{\parallel,j} R^2 B^\phi \frac{\partial \Omega}{\partial \psi} \nabla \psi - 2\rho_{\parallel,j} \Omega R B^\phi \left(\frac{\partial R}{\partial \psi} \nabla \psi + \frac{\partial R}{\partial \theta} \nabla \theta + \frac{\partial R}{\partial \phi} \nabla \phi \right) - \rho_{\parallel,j} \Omega R^2 \nabla B^\phi \end{aligned} \quad (2.93)$$

With all the terms calculated, we may implement the new corresponding guiding center equations. VENUS-LEVIS only requires the descriptions for \mathbf{A}^* , \mathbf{B}^* and \mathbf{E}^* ; it computes the dot and cross products required to form the guiding-center forces shown in Eq. (2.80). We can notice, from Fig. 2.4, that the guiding-center motion of a particle follows its full-Lorentz motion very closely within the order of the approximation. Note that For simulations with a large number of trapped particles, as can be expected for supersonic Mach numbers for heavy impurity species, the full-Lorentz orbits are computationally much slower (up to five times slower) than the guiding-center orbits, making guiding-center approach more feasible. Notice that from Eqs. (2.80) and (2.100), the effects of $\nabla \Phi_1$ yield contributions to the guiding-center equations similar to the centrifugal effects just considered, as is explained in the next section.

2.5.2 Quasi-neutrality corrections in case of plasma rotation

The centrifugal force resulting from the leading-order electric field $-\nabla \Phi_0$ is mass sensitive, and significantly displaces the main ions as compared to the electrons. This resulting charge separation results in a higher-order electric field correction $-\nabla \Phi_1$ which aims to bring the two species together. To calculate this compensating potential and its corresponding field, we assume a local Maxwellian for the ion and electron species of the plasma and then minimize the charge separation. Single particles of species j in the rotating frame have the energy

$$E_{rot,j} = \frac{1}{2} m_j w_{\parallel,j}^2 + \mu_j B - \frac{1}{2} m_j \Omega^2 R^2 + Z_j e \Phi_1. \quad (2.94)$$

The particle distribution can now be locally expressed as the Maxwellian by integrating over the velocities $w_{\parallel,j}$ and $w_{\perp,j}$

$$F_j(\psi) = \frac{\bar{n}_j(\psi)}{[2\pi T_j(\psi)]^{3/2}} \exp \left(-\frac{E_{rot}}{T_j(\psi)} \right). \quad (2.95)$$

Chapter 2. Equilibrium Theory, Guiding-Center Orbits and Neoclassical Theory with Flows

Integrating for the number density $n_j(\psi, \theta)$, one can derive the relation

$$n_j(\psi, \theta) = \bar{n}_j(\psi) \exp \left(\frac{m_j \Omega^2 R^2}{2T_j} - \frac{Z_j e \Phi_1}{T_j} \right). \quad (2.96)$$

On preserving the quasi-neutrality between ions and electrons (subscripts i and e respectively) through

$$\sum_{j=\{i,e\}} n_j(\psi, \theta) Z_j e = 0, \quad (2.97)$$

assuming $\bar{n}_i = \bar{n}_e$ and , and neglecting the centrifugal shift on electrons, we have

$$\exp \left(\frac{m_i \Omega^2 R^2}{2T_i} - \frac{e \Phi_1}{T_i} \right) - \exp \left(\frac{e \Phi_1}{T_e} \right) = 0 \quad (2.98)$$

and on approximating the potentials to first order

$$\left(\frac{m_i \Omega^2 R^2}{2T_i} - \frac{e \Phi_1}{T_i} \right) - \left(\frac{e \Phi_1}{T_e} \right) = 0 \quad (2.99)$$

we obtain Φ_1 as

$$\Phi_1(\psi, \theta) = \frac{m_i \Omega^2 R^2}{2e} \frac{T_e}{T_i + T_e}. \quad (2.100)$$

This is the form of Φ_1 that will appear in the guiding-center equations (2.113) and (2.114). If we assume that both the ions and the electrons have the same temperature, one can see that the potential Φ_1 is half the value in magnitude to the energy contributed by the centrifugal term. This term for ions reduces some of the displacement caused by the rotation by a factor of $\mathcal{M}_{*,i}^2$, and for electrons increases it by the same factor $\mathcal{M}_{*,e}^2$. The densities for species j then becomes

$$n_j(\psi, \theta) = \bar{n}_j(\psi) \exp \mathcal{M}_{*,j}^2, \quad (2.101)$$

where $\mathcal{M}_{*,j}^2$ is

$$\mathcal{M}_{*,j}^2 = \left(m_j - \frac{m_i T_e}{T_i + T_e} \right) \frac{\Omega^2 R^2}{2T_j} \quad (2.102)$$

In doing so, it brings the ions and electrons densities together, thus satisfying quasi-neutrality. Therefore, one can see that the effect of the centrifugal force trying to violate the quasi-neutrality is mitigated by the lower-order potential. The resultant modified electric field then

Plots of GC(red) and FL(green) for $\lambda_0=0.8$ and $s_0=0.25$ for 10^{-5} s with strong plasma rotation.

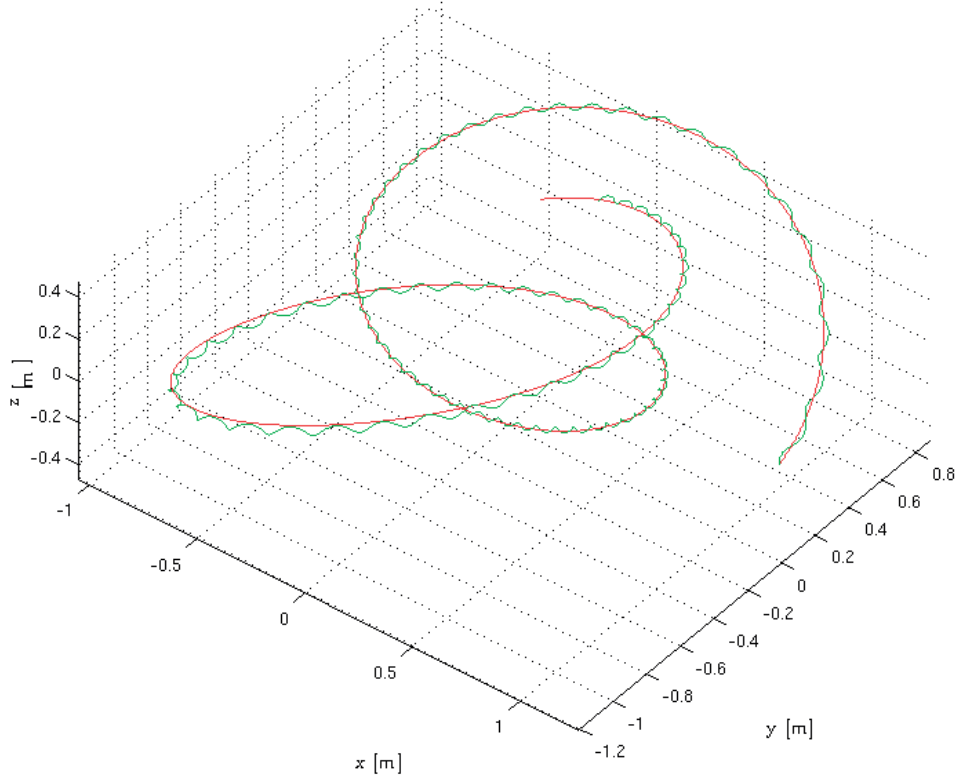


Figure 2.4 – The guiding-center orbit (red) as compared to full Lorentz (green) orbit. It follows closely to each other within the first-order guiding-center approximation. Again, the Mach number is chosen to be $\mathcal{M}_0^2 = 20$ for illustration purposes.

becomes

$$\begin{aligned} \mathbf{E}^* = & -\sqrt{g}\Omega R^2 \{ (B^\theta g^{\phi\phi} - B^\phi g^{\theta\phi}) \nabla\psi + B^\phi g^{\psi\phi} \nabla\theta - B^\theta g^{\psi\phi} \nabla\phi \} \\ & - \left(\frac{\mu_j}{Z_j e} + w_{\parallel,j} \rho_{\parallel,j} \right) \nabla B - \left(m_j - \frac{m_i T_e}{T_i + T_e} \right) \frac{\Omega^2 R^2}{Z_j e} \left[\left(\frac{1}{\Omega} \frac{\partial \Omega}{\partial \psi} + \frac{1}{R} \frac{\partial R}{\partial \psi} \right) \nabla\psi + \frac{1}{R} \frac{\partial R}{\partial \theta} \nabla\theta + \frac{1}{R} \frac{\partial R}{\partial \phi} \nabla\phi \right] \\ & - \rho_{\parallel,j} R^2 B^\phi \frac{\partial \Omega}{\partial \psi} \nabla\psi - 2\rho_{\parallel,j} \Omega R B^\phi \left(\frac{\partial R}{\partial \psi} \nabla\psi + \frac{\partial R}{\partial \theta} \nabla\theta + \frac{\partial R}{\partial \phi} \nabla\phi \right) - \rho_{\parallel,j} \Omega R^2 \nabla B^\phi \quad (2.103) \end{aligned}$$

where the centrifugal force term has been reduced by a factor comparable to the centrifugal force.

2.5.3 Equivalence with the Traditional Expression for Drifts

In this section, we transform the guiding-center equations (2.80) in order to compare its form with the guiding-center equations usually found in existing literature. We expand the

Chapter 2. Equilibrium Theory, Guiding-Center Orbits and Neoclassical Theory with Flows

perpendicular particle drifts and provide an explanation as to how the $\mathbf{E}_0 \times \mathbf{B}$ flow term cancels out in the expressions for the particle motion, as is usually the form in current literature [Brizard, 1995, Peeters et al., 2009]. We first evaluate the drifts by expanding the terms in Eq. 2.80. The value of the modified electric field \mathbf{E}^* can be given by

$$\mathbf{E}^* = \mathbf{E} - \left(\frac{\mu_j}{Z_j e} + \frac{Z_j e}{m_j} \rho_{\parallel,j}^2 B \right) \nabla B - \frac{1}{2} \frac{m_j}{Z_j e} \nabla (U_{0,j}^2) - \rho_{\parallel,j} \nabla (\mathbf{U}_{0,j} \cdot \mathbf{B}) \quad (2.104)$$

which could be written as

$$\mathbf{E}^* = \mathbf{E} - \frac{\mu_j}{Z_j e} \nabla B - \frac{1}{2} \frac{m_j}{Z_j e} \nabla U_{0,j}^{*2}, \quad (2.105)$$

where we have just substituted $\mathbf{U}_{0,j} + Z_j e \rho_{\parallel,j} \mathbf{B} / m_j = \mathbf{U}_{0,j}^*$. We expand

$$\frac{1}{2} \nabla U_{0,j}^{*2} = \nabla \left(\frac{1}{2} \mathbf{U}_{0,j}^* \cdot \mathbf{U}_{0,j}^* \right) = \mathbf{U}_{0,j}^* \cdot \nabla \mathbf{U}_{0,j}^* + \mathbf{U}_{0,j}^* \times (\nabla \times \mathbf{U}_{0,j}^*). \quad (2.106)$$

Thus, $\dot{\mathbf{X}}_j$ becomes

$$\dot{\mathbf{X}}_j = (\mathbf{U}_{0,j}^* \cdot \mathbf{b}) \frac{\mathbf{B}^*}{B_{\parallel}^*} + \frac{1}{B_{\parallel}^*} \left\{ \mathbf{E} - \frac{\mu_j}{Z_j e} \nabla B - \frac{m_j}{Z_j e} \mathbf{U}_{0,j}^* \cdot \nabla \mathbf{U}_{0,j}^* - \frac{m_j}{Z_j e} \mathbf{U}_{0,j}^* \times (\nabla \times \mathbf{U}_{0,j}^*) \right\} \times \mathbf{b}. \quad (2.107)$$

We expand $\{\mathbf{U}_{0,j}^* \times (\nabla \times \mathbf{U}_{0,j}^*)\} \times \mathbf{b}$, and take it out of the parentheses,

$$\{\mathbf{U}_{0,j}^* \times (\nabla \times \mathbf{U}_{0,j}^*)\} \times \mathbf{b} = (\mathbf{U}_{0,j}^* \cdot \mathbf{b}) \nabla \times \mathbf{U}_{0,j}^* - (\nabla \times \mathbf{U}_{0,j}^* \cdot \mathbf{b}) \mathbf{U}_{0,j}^*, \quad (2.108)$$

which can then be merged with the first term on the RHS. Realizing that $\mathbf{B}^* = \mathbf{B} + m_j \nabla \times \mathbf{U}_{0,j}^* / Z_j e$, we have now

$$\begin{aligned} \dot{\mathbf{X}}_j &= \frac{\mathbf{U}_{0,j}^* \cdot \mathbf{b}}{B_{\parallel}^*} \left\{ \mathbf{B} + \frac{m_j}{Z_j e} \nabla \times \mathbf{U}_{0,j}^* \right\} - \frac{m_j}{Z_j e} \frac{\mathbf{U}_{0,j}^* \cdot \mathbf{b}}{B_{\parallel}^*} \nabla \times \mathbf{U}_{0,j}^* + \frac{m_j}{Z_j e} \frac{\mathbf{U}_{0,j}^*}{B_{\parallel}^*} \mathbf{b} \cdot \nabla \times \mathbf{U}_{0,j}^* \\ &\quad - \frac{\mathbf{b}}{B_{\parallel}^*} \times \left\{ \mathbf{E} - \frac{\mu_j}{Z_j e} \nabla B - \frac{m_j}{Z_j e} \mathbf{U}_{0,j}^* \cdot \nabla \mathbf{U}_{0,j}^* \right\}. \end{aligned} \quad (2.109)$$

We can see that a part of the first and the complete second term cancel out. We can now obtain $\mathbf{b} \cdot \nabla \times \mathbf{U}_{0,j}^*$ from:

$$B_{\parallel}^* = B + \frac{m_j}{Z_j e} \mathbf{b} \cdot \nabla \times \mathbf{U}_{0,j}^*, \quad (2.110)$$

and on substituting, we get

$$\dot{\mathbf{X}}_j = \mathbf{U}_{0,j}^* - \frac{B}{B_{\parallel}^*} \left\{ \mathbf{U}_{0,j}^* - (\mathbf{U}_{0,j}^* \cdot \mathbf{b}) \mathbf{b} \right\} - \frac{\mathbf{b}}{B_{\parallel}^*} \times \left\{ \mathbf{E} - \frac{\mu_j}{Z_j e} \nabla B - \frac{m_j}{Z_j e} \mathbf{U}_{0,j}^* \cdot \nabla \mathbf{U}_{0,j}^* \right\}. \quad (2.111)$$

Now, $\mathbf{U}_{0,j}^* - (\mathbf{U}_{0,j}^* \cdot \mathbf{b}) \mathbf{b}$ is just $\mathbf{U}_{0\perp,j}^*$ and that $\mathbf{U}_{0\perp,j}^* B = \mathbf{b} \times (\mathbf{U}_{0\perp,j}^* \times \mathbf{B})$. We also substitute the electric field $\mathbf{E} = -\nabla\Phi_0 - \nabla\Phi_1$. Doing so, we have

$$\dot{\mathbf{X}}_j = \mathbf{U}_{0,j}^* - \frac{\mathbf{b}}{B_{\parallel}^*} \times (\mathbf{U}_{0\perp,j}^* \times \mathbf{B} - \nabla\Phi_0) - \frac{\mathbf{b}}{B_{\parallel}^*} \times \left\{ -\nabla\Phi_1 - \frac{\mu_j}{Z_j e} \nabla B - \frac{m_j}{Z_j e} \mathbf{U}_{0,j}^* \cdot \nabla \mathbf{U}_{0,j}^* \right\}. \quad (2.112)$$

From ideal Ohm's law, we know that $\mathbf{U}_{0\perp,j}^* \times \mathbf{B} - \nabla\Phi_0 = 0$, thus we have our expression finally reduced to

$$\dot{\mathbf{X}}_j = \mathbf{U}_{0,j}^* + \frac{\mathbf{b}}{B_{\parallel}^*} \times \left\{ \nabla\Phi_1 + \frac{\mu_j}{Z_j e} \nabla B + \frac{m_j}{Z_j e} \mathbf{U}_{0,j}^* \cdot \nabla \mathbf{U}_{0,j}^* \right\}. \quad (2.113)$$

And hence, the effect of the leading-order electric field is contained in $\mathbf{U}_{0,j}^*$. Notice that the term $\mathbf{U}_{0,j}^* \cdot \nabla \mathbf{U}_{0,j}^*$ contains the standard curvature drift, centrifugal drift and Coriolis drifts. From similar calculations, we obtain an expression for $\dot{\rho}_{\parallel,j}$

$$\dot{\rho}_{\parallel,j} = \frac{\mathbf{B}^*}{\mathbf{B} \cdot \mathbf{B}^*} \cdot \left\{ \nabla\Phi_1 + \frac{\mu_j}{Z_j e} \nabla B + \frac{m_j}{Z_j e} \mathbf{U}_{0,j}^* \cdot \nabla \mathbf{U}_{0,j}^* \right\} \quad (2.114)$$

We now have $(\dot{\rho}_{\parallel,j}, \dot{\mathbf{X}}_j)$ in a more familiar form where we can easily extract the $\mathbf{B} \times \nabla B$, $\mathbf{E} \times \mathbf{B}$, centrifugal and Coriolis drifts. The final expressions for the drifts are the similar to the one obtained in Ref. [Brizard, 1995] and Ref. [Peeters et al., 2009], which implicitly include the curvature, centrifugal and Coriolis drifts in the $\mathbf{U}_{0,j}^* \cdot \nabla \mathbf{U}_{0,j}^*$ term.

2.6 Introduction to bootstrap current

The self-generated current in a tokamak plasma is known as the bootstrap current. The current arises because of a small portion of trapped particles getting collisionally released into passing orbits which carry a substantially higher current as opposed to the small current carried by the toroidal drift precession of trapped particles [Hinton and Hazeltine, 1976]. In addition to the Ohmic current and the current from current drives such as ECCD, the bootstrap current is an integral part of the total toroidal current. As this current depends on collisions among the particles, it varies in different regimes of collisionality, ranging from the highest in the collisionless banana regime to virtually zero in the high-collision Pfirsch-Schlüter regime [Shaing et al., 2015].

Chapter 2. Equilibrium Theory, Guiding-Center Orbits and Neoclassical Theory with Flows

Our aim is to calculate the bootstrap-current and a magnetic equilibrium consistently with one another in the collisionless banana regime. This is to say that if the initial current profile used for the magnetic equilibrium calculation included the bootstrap current, the equilibrium thus generated would extract the same bootstrap current density profile as the one we began with. In order to establish this iteratively, we need a magnetic equilibrium and an interface for calculating the bootstrap current. The equilibrium for the iterative process is provided by the Variational Moments Equilibrium Code (VMEC)[Hirshman and Whitson, 1983]. VMEC is a versatile ideal free-boundary MHD equilibrium code which generates equilibrium by minimizing the variations in the equilibrium energy functional. Using the free-boundary version of VMEC[Hirshman et al., 1986], we generate equilibria for the desired current and pressure profiles. We also vary the equilibrium by specifying an initial guess of a skewed magnetic axis of 1/1 helicity with axisymmetric boundary conditions that leads to the formation of a helical core, thereby allowing the representation of a 1/1 internal kink mode. One can include the effect of external fields in VMEC by prescribing the coil positions and coil currents. A package within the VMEC-Suite, MAKEGRID allows us to calculate the magnetic field generated by the specified coils. Including this external magnetic field in the equilibrium calculations allows us to generate equilibria with the ideal response of the equilibrium to the external fields. One element of this study is to analyse the variation in the equilibrium and the bootstrap currents due to the varying number of toroidal field coils (TF-coils), and due to the Resonant Magnetic Perturbation (RMP) coils. In addition to the externally produced 3D effects, VMEC can also generate a realistic representation of a saturated 1/1 internal kink mode[Brunetti et al., 2014]. Of special interest will be to examine and contrast the 3D helical core state and the axisymmetric sister-state and thus isolate the 3D effect of the bootstrap current.

2.7 Bootstrap Current Models and Approach to Simulation

For calculating the bootstrap current, we consider two models. First, the *Sauter* model [Sauter et al., 1999], which is an axisymmetric 2D model, and the second is the *Shaing-Callen* model [Shaing and Callen, 1983, Shaing et al., 1986a] which is quasi-analytic and valid for 3D equilibria. The 2D model for the bootstrap current is written in terms of coefficients that can, as will be seen later, be still calculated for 3D magnetic equilibria. In contrast, the Shaing-Callen model, which is fully 3D, should be more robust for 3D equilibria. They should as a benchmark, however, agree in the axisymmetric limit.

The subsections are organized as follows: First, we describe the *Sauter* bootstrap current model in subsection 2.7.1. Then we elaborate upon the *Shaing-Callen* bootstrap current model in subsection 2.7.2. Further, we explain the resonance effects which arise in the 3D model, and the mitigation of the resonances through the resonance detuning scheme in subsection 2.7.4. Finally, we describe the iterative scheme used for the self-consistent bootstrap current calculation in subsection 2.7.5.

2.7.1 Sauter Model

The expression given by Sauter et al, in which the parallel bootstrap current density $\langle \mathbf{J}_{bs} \cdot \mathbf{B} \rangle$, is given by

$$\langle \mathbf{J}_{bs} \cdot \mathbf{B} \rangle = -\frac{I(\psi)}{\psi'} p_e \left[L_{31} \frac{p}{p_e} \frac{\partial \ln p}{\partial \psi} + L_{32} \frac{\partial \ln T_e}{\partial \psi} + L_{34} \alpha_0 \frac{\partial \ln T_i}{\partial \psi} \right] \quad (2.115)$$

where $\mu_0 I(\psi) = -B_\psi$ in Boozer coordinates. Throughout the current work, we work in S. I. units for the sake of consistency through all our simulations. Following usual conventions, ψ is the flux-surface label, p is the pressure and T_j is the temperature of the species j in the plasma. The dimensionless factor α_0 is a coefficient for correctly accounting for the contribution of each species towards the bootstrap current in the collisionless limit.

The coefficients L_{31} , L_{32} , L_{34} and α_0 are described in Ref. [Sauter et al., 1999] where these are determined as fits of functions of the trapped fraction of particles and collisionalities. After the fit to the previously computed results in Ref. [Sauter et al., 1999], these have the following expressions in terms of the trapped particle fraction f_t in the $1/\nu$ collisionless regime:

$$L_{31} = \left(1 + \frac{1.4}{Z+1} \right) f_t - \frac{1.9}{Z+1} f_t^2 + \frac{0.3}{Z+1} f_t^3 + \frac{0.2}{Z+1} f_t^4 \quad (2.116)$$

$$L_{32} = \left[\frac{0.05 + 0.62Z}{Z(1 + 0.44Z)} (f_t - f_t^4) + \frac{1}{1 + 0.22Z} (f_t^2 - f_t^4 - 1.2(f_t^3 - f_t^4)) + \frac{1.2}{1 + 0.5Z} f_t^4 \right] \\ + \left[-\frac{0.56 + 1.93Z}{Z(1 + 0.44Z)} (f_t - f_t^4) + \frac{4.95}{1 + 0.44Z} (f_t^2 - f_t^4 - 0.55(f_t^3 - f_t^4)) - \frac{1.2}{1 + 0.5Z} f_t^4 \right] \quad (2.117)$$

$$L_{34} \approx L_{31} \quad (2.118)$$

$$\alpha_0 = \frac{1.17(1 - f_t)}{1 - 0.22f_t - 0.19f_t^2} \quad (2.119)$$

where in L_{32} , the two terms in their respective square brackets represent the electron and ion contributions to L_{32} respectively. Z refers to the effective screened charge of the ions. In accordance to previous work, we set $Z = 1$ throughout our simulations neglecting any screening effect. The trapped fraction of particles f_t is computed as

$$f_t = 1 - \frac{3}{4} \frac{\langle B^2 \rangle}{B_{max}^2} \int_0^1 \frac{\lambda}{\langle g_1 \rangle} d\lambda. \quad (2.120)$$

g_1 is given by

$$g_1 = \sqrt{1 - \lambda \frac{B}{B_{max}}} \quad (2.121)$$

Chapter 2. Equilibrium Theory, Guiding-Center Orbits and Neoclassical Theory with Flows

and the angle brackets $\langle x \rangle$ represent the quantity x averaged over a flux-surface. Heretofore, we refer to equations (2.115-2.119) as the *Sauter formula*.

2.7.2 Shaing-Callen Model

The *Shaing-Callen formulation* for the bootstrap current in the zero-collisionality banana regime is given by

$$\langle \mathbf{J}_{\mathbf{bs}, \mathbf{B}} \rangle = -G_b(\psi) \left[L_{31} \frac{\partial p}{\partial \psi} + L_{32}^e n_e \frac{\partial T_e}{\partial \psi} + L_{32}^i n_i \frac{\partial T_i}{\partial \psi} \right] \quad (2.122)$$

where $G_b \equiv G_b(\psi)$ is a geometrical factor in the banana regime, calculated through averaging over the entire 3D field. The coefficients L_{31} and $L_{32}^{i,e}$ are analytically determined in terms of the neoclassical viscosity coefficients and the trapped particle fractions. The formulae are as follows:

$$L_{31} = \{\mu_{e1}(L_{22}^{ee} + \mu_{e3}) - \mu_{e2}(L_{12}^{ee} + \mu_{e2})\} / D \quad (2.123)$$

$$L_{32}^e = (\mu_{e3} l_{12}^{ee} - \mu_{e2} l_{22}^{ee}) / D \quad (2.124)$$

$$L_{32}^i = -L_{31} \mu_{i2} l_{22}^{ii} / \{\mu_{i1}(l_{22}^{ii} + \mu_{i3} - \mu_{i2}^2)\} \quad (2.125)$$

$$D = (l_{11}^{ee} + \mu_{e1})(l_{22}^{ee} + \mu_{e3}) - (l_{12}^{ee} + \mu_{e2})^2 \quad (2.126)$$

and where,

$$\mu_{a1} = \frac{f_t}{f_c} \left\{ \sqrt{2} - \ln(1 + \sqrt{2}) + Z \delta_{ae} \right\} \quad (2.127)$$

$$\mu_{a2} = \frac{f_t}{f_c} \left\{ 2\sqrt{2} - \frac{5}{2} \ln(1 + \sqrt{2}) + \frac{3}{2} Z \delta_{ae} \right\} \quad (2.128)$$

$$\mu_{a3} = \frac{f_t}{f_c} \left\{ \frac{39}{8} \sqrt{2} - \frac{25}{4} \ln(1 + \sqrt{2}) + \frac{13}{4} Z \delta_{ae} \right\} \quad (2.129)$$

where δ_{ij} is the Krönecker delta, $f_c = 1 - f_t$ the fraction of circulating particles, and

$$l_{11}^{ee} = Z, \quad l_{12}^{ee} = \frac{3}{2} Z, \quad l_{21}^{ee} = \sqrt{2} + \frac{13}{4} Z, \quad l_{22}^{ee} = Z. \quad (2.130)$$

Physically, the μ -coefficients are related to the friction coefficients among various species and the l -coefficients are the proportionality of the contribution by each species. The expressions for the L -coefficients can also be found in Ref. [Johnson et al., 1999]. In this sense, the Shaing-Callen formulation can be considered to be a analytic approximation to determining the bootstrap current.

The geometrical factor $G_b(\psi)$ is computed in the $1/\nu$ (collisionless) regime as

$$G_b(\psi) = \frac{1}{f_t} \left\{ \langle g_2 \rangle - \frac{3}{4} \frac{\langle B^2 \rangle}{B_{max}^2} \int_0^1 \frac{\langle g_4 \rangle}{\langle g_1 \rangle} \lambda d\lambda \right\} \quad (2.131)$$

where again,

$$\begin{aligned} f_t &= 1 - \frac{3}{4} \frac{\langle B^2 \rangle}{B_{max}^2} \int_0^1 \frac{\lambda}{\langle g_1 \rangle} d\lambda, \\ g_1 &= \sqrt{1 - \lambda \frac{B}{B_{max}}}. \end{aligned}$$

The quantities g_2 and g_4 , in turn, must also satisfy the following expressions.

$$\mathbf{B} \cdot \nabla \left(\frac{g_2}{B^2} \right) = \mathbf{B} \times \nabla \psi \cdot \nabla \left(\frac{1}{B^2} \right) \quad (2.132)$$

$$\mathbf{B} \cdot \nabla \left(\frac{g_4}{g_1} \right) = \mathbf{B} \times \nabla \psi \cdot \nabla \left(\frac{1}{g_1} \right) \quad (2.133)$$

$$g_2(B_{max}) = 0 \quad (2.134)$$

$$g_4(B_{max}) = 0 \quad (2.135)$$

where ψ is the radial variable in Boozer coordinates. We integrate these equations by transforming them into Fourier-space, where the gradients can be realized simply as coefficients multiplying the Fourier-transformed integrand.

2.7.3 Axisymmetric Comparison of the Sauter and the Shaing-Callen Formulations

It is necessary to compare the Sauter and Shaing-Callen formulations because they must agree in the axisymmetric limit, as they derive from different approaches. On assuming the magnetic field in axisymmetry to have the form

$$\mathbf{B} = I(\psi) \nabla \phi + \nabla \psi \times \nabla \phi \quad (2.136)$$

one can solve the equations for g_2 in axisymmetry in Boozer coordinates and obtain

$$g_2 = \frac{I(\psi)}{\psi'} \left(1 - \frac{B^2}{B_{max}^2} \right) \quad (2.137)$$

and therefore the flux-surface average becomes

$$\langle g_2 \rangle = \frac{I(\psi)}{\psi'} \left(1 - \frac{\langle B^2 \rangle}{B_{max}^2} \right). \quad (2.138)$$

Chapter 2. Equilibrium Theory, Guiding-Center Orbits and Neoclassical Theory with Flows

Similarly, g_4 in axisymmetry[Nakajima and Okamoto, 1992] becomes

$$g_4 = \frac{I(\psi)}{\psi'} \left(1 - \frac{g_1}{\sqrt{1-\lambda}} \right) \quad (2.139)$$

with its corresponding flux-surface average

$$\langle g_4 \rangle = \frac{I(\psi)}{\psi'} \left(1 - \frac{\langle g_1 \rangle}{\sqrt{1-\lambda}} \right) \quad (2.140)$$

Since geometric factor in the banana regime is

$$G_b(\psi) = \frac{1}{f_t} \left\{ \langle g_2 \rangle - \frac{3}{4} \frac{\langle B^2 \rangle}{B_{max}^2} \int_0^1 \frac{\langle g_4 \rangle}{\langle g_1 \rangle} \lambda d\lambda \right\}, \quad (2.141)$$

we replace the values of $\langle g_2 \rangle$ and $\langle g_4 \rangle$ and obtain

$$G_b(\psi) = \frac{1}{f_t} \frac{I(\psi)}{\psi'} \left\{ 1 - \frac{\langle B^2 \rangle}{B_{max}^2} - \frac{3}{4} \frac{\langle B^2 \rangle}{B_{max}^2} \int_0^1 \left(\frac{1}{\langle g_1 \rangle} - \frac{1}{\sqrt{1-\lambda}} \right) \lambda d\lambda \right\}, \quad (2.142)$$

The last term in the parentheses integrates to 4/3, therefore we have

$$G_b(\psi) = \frac{1}{f_t} \frac{I(\psi)}{\psi'} \left\{ 1 - \frac{3}{4} \frac{\langle B^2 \rangle}{B_{max}^2} \int_0^1 \frac{\lambda d\lambda}{\langle g_1 \rangle} \right\}. \quad (2.143)$$

Recalling that the term in the parentheses is equal to f_t , we finally have

$$G_b(\psi) = \frac{I(\psi)}{\psi'}, \quad (2.144)$$

which is the same as the Sauter expression. Furthermore, the L -factors are similar to the order of $(f_t/f_c)^2$ [Watanabe et al., 1995]. Thus the two formulations are identical in axisymmetry, which will be used as a benchmark to test the numerical agreement of the two schemes in axisymmetric and approximately axisymmetric (E.g. with weak RMPs) conditions.

2.7.4 Numerical resonance mitigation

The mitigation of numerical resonances at rational q -surfaces is of particular importance to the *Shaing-Callen* model[Cooper et al., 2004]. For solving the equations in the Shaing-Callen model, we use a Fourier-decomposition scheme to simplify the equations in Fourier space. However, the $\mathbf{B} \cdot \nabla$ operator becomes $(m\Psi' - n\Phi')$, which is zero at rational $q = m/n$ surfaces, which raises singularities at rational surfaces during the inversion. This has been mitigated in previous work by the inclusion of a resonance detuning operator Δ_{mn} , which numerically prevents the singularities from occurring. The detuning operator is defined as follows:

$$\Delta_{mn} = \Delta[(m+1)\Psi' - n\Phi'] \quad (2.145)$$

2.7. Bootstrap Current Models and Approach to Simulation

where Δ is a dimensionless detuning factor. The singularity itself is prevented by the transformation

$$\frac{1}{m\Psi' - n\Phi'} \rightarrow \frac{m\Psi' - n\Phi'}{(m\Psi' - n\Phi')^2 + \Delta_{mn}^2}. \quad (2.146)$$

It is important to note that this scheme is purely a numerical correction on the resonant $q = m/n$ surfaces. In reality, these resonances represent parallel current sheets which would create islands and local pressure flattening (and thus reduction of the local bootstrap current density) in a resistive MHD model. However, this cannot be accounted for by an ideal MHD equilibrium code like VMEC, and hence is unphysical under the VMEC equilibrium model. As will be seen, the 1/1 non-resonant internal kink mode is a particularly interesting application because the core 3D structure avoids resonance and hence, the need of the resonance detuning here.

In the bootstrap current density profile, the resonant contributions appear as sharp spikes at the values of s corresponding to the resonant q -values. These spikes are very sensitive to the choice of the detuning factor Δ . Choosing too large a value of Δ makes the current density profile globally distorted to a significant order, and the choice of too small Δ leads to the presence of large spikes at rational q surfaces. We will explore this in more detail in the next section.

2.7.5 Self-Consistent Computation of The Toroidally-Averaged Bootstrap Current

In order to calculate the flux-surface averaged toroidal bootstrap current density $\langle \mathbf{J}_{bs} \cdot \nabla \phi \rangle(\psi)$, we must average over the toroidal and poloidal angles as follows

$$\langle \mathbf{J}_{bs} \cdot \nabla \phi \rangle(\psi) = \int_0^s \frac{\langle \mathbf{J}_{bs} \cdot \mathbf{B} \rangle(\psi)}{B^2} \Phi'(\psi) du dv. \quad (2.147)$$

where again the angled brackets $\langle x \rangle$ are used to represent the flux-surface average of the parameter x . In VMEC coordinates, this is computationally difficult to perform on account of coordinate system used. In the VMEC (s, u, v) coordinate system, the integrand is not a flux-surface quantity, which makes an additional averaging necessary. The toroidal current density $\langle \mathbf{J}_{bs} \cdot \nabla \phi \rangle$ in VMEC coordinates is given by

$$\langle \mathbf{J}_{bs} \cdot \nabla \phi \rangle(\psi) = \langle \mathbf{J}_{bs} \cdot \mathbf{B} \rangle(\psi) \int \int \frac{du dv \sqrt{g} \left(\Phi' - \frac{\partial \lambda}{\partial u} \right) g^{\nu\nu}}{\left(\Psi' + \frac{\partial \lambda}{\partial v} \right)^2 g_{uu} + \left(\Phi' - \frac{\partial \lambda}{\partial u} \right)^2 g_{vv} + 2 \left(\Psi' + \frac{\partial \lambda}{\partial v} \right) \left(\Phi' - \frac{\partial \lambda}{\partial u} \right) g_{uv}}. \quad (2.148)$$

This is computationally expensive to calculate over each flux-surface and over each iteration of the scheme, as the double integral would have to be performed for every point of the defined grid in u and v with sufficient precision. Instead, we convert the obtained equilibrium to Boozer coordinates using TERPSICHOE[Cooper, 1992]. On multiplying the numerator and

Chapter 2. Equilibrium Theory, Guiding-Center Orbits and Neoclassical Theory with Flows

the denominator by the Jacobian \sqrt{g} , we find that they both reduce to flux-surface functions, which reduces the averaging to

$$\langle \mathbf{J}_{bs} \cdot \nabla \phi \rangle(\psi) = \langle \mathbf{J}_{bs} \cdot \mathbf{B} \rangle(\psi) \frac{\Phi'(s) V'(s)}{\Psi'(s) J(s) - \Phi'(s) I(s)}. \quad (2.149)$$

It is immediately noticeable that the computation required to perform the integral has been reduced by a factor of $n_u \times n_v$, where n_u and n_v are the grid sizes chosen over the VMEC coordinates u and v . Now one can integrate over the value of $\langle \mathbf{J}_{bs} \cdot \nabla \phi \rangle$ to arrive at the value of bootstrap current profile $\mathcal{J}_{bs}(\psi)$ as follows:

$$\mathcal{J}_{bs}(\psi) = \int_0^\psi \langle \mathbf{J}_{bs} \cdot \nabla \phi \rangle(\psi) d\psi \quad (2.150)$$

where \mathcal{J}_{bs} is the total bootstrap current obtained in amperes. In addition, the net toroidal current density has to be adjusted for the bootstrap current for the next iteration of the scheme in order to keep the total toroidal plasma current \mathcal{J}_p constant. $\langle \mathbf{J}_{Ohm} \cdot \nabla \phi \rangle(\psi)$ is the purely Ohmic current density profile over the first iteration of the equilibrium, chosen as per typical current profiles in MAST experiments. The bootstrap current and the Ohmic current profiles are then merged so as to preserve the total toroidal current as follows:

$$\langle \mathbf{J} \cdot \nabla \phi \rangle(\psi) = \left(\frac{\mathcal{J}_p - \mathcal{J}_{bs}}{\mathcal{J}_{Ohm}} \right) \langle \mathbf{J}_{Ohm} \cdot \nabla \phi \rangle(\psi) + \langle \mathbf{J}_{bs} \cdot \nabla \phi \rangle(\psi) \quad (2.151)$$

The coefficient of $\langle \mathbf{J}_{Ohm} \cdot \nabla \phi \rangle(\psi)$ is the new Ohmic current fraction $\mathcal{J}_{Ohm}/\mathcal{J}_p = (\mathcal{J}_p - \mathcal{J}_{bs})/\mathcal{J}_p$. Integration of current density over ψ at each step will conserve the total current to the chosen value of \mathcal{J}_p . At each iteration, the form of the Ohmic current is kept the same, but the overall current profile changes with respect to the form of the bootstrap current obtained in the last equilibrium. For the next iteration, VMEC takes the profile $2\pi \langle \mathbf{J} \cdot \nabla \phi \rangle(\psi)$ and creates a new equilibrium satisfying that profile.

In order for the iterative scheme to end, we stop it after an iteration where the bootstrap current converges to a sufficient precision. To that effect, we define the tolerance ‘ tol ’ as the relative difference between the current density profiles between successive iterations. Therefore, we have for the n^{th} iteration

$$tol = \frac{\mathcal{J}^{(n)}(\psi) - \mathcal{J}^{(n-1)}(\psi)}{\mathcal{J}^{(n-1)}(\psi)} \quad (2.152)$$

where the superscript n represents the total toroidal current at the n^{th} iteration. We declare the bootstrap current density as having being ‘saturated’ when the specified tolerance is reached.

2.8 Neoclassical Physics of the Background Plasma and Impurities

We now describe the inclusion of the parallel dynamics in the collision operator which are crucial to the friction force experienced by the impurity particles. The general force balance equations for the impurity, main ion and electron species can be written as:

$$-m_W n_W \Omega^2 R \mathbf{e}_R = -\nabla p_W - n_W Z_W (-\nabla \Phi_0 + \mathbf{U}_0 \times \mathbf{B} - \nabla \Phi_1 + \mathbf{U}_{1,W} \times \mathbf{B}) - \mathcal{F} \quad (2.153)$$

$$-m_i n_i \Omega^2 R \mathbf{e}_R = -\nabla p_i - n_i e (-\nabla \Phi_0 + \mathbf{U}_0 \times \mathbf{B} - \nabla \Phi_1 + \mathbf{U}_{1,i} \times \mathbf{B}) + \mathcal{F} \quad (2.154)$$

$$0 = -\nabla p_e - n_i e (-\nabla \Phi_0 + \mathbf{U}_0 \times \mathbf{B} + \mathbf{U}_{1,e} \times \mathbf{B}), \quad (2.155)$$

where, as before, \mathbf{U}_0 denotes the $\mathbf{E} \times \mathbf{B}$ flow velocity which is independent of the species, and $\mathbf{U}_{i,j}$ is the diamagnetic flow velocity which is different for each species j . The force \mathcal{F} is the friction force acting on each species. Now, according to ideal Ohm's law, the leading order $\nabla \Phi_0$ will cancel out with the $\mathbf{U}_0 \times \mathbf{B}$ terms. Therefore, only the diamagnetic flow components will remain in the equation for the impurities. In the trace impurity limit, we neglect the pressure of the impurities. Thus, the equations reduce to:

$$-m_W n_W \Omega^2 R \mathbf{e}_R = -n_W Z_W (-\nabla \Phi_1 + \mathbf{U}_{1,W} \times \mathbf{B}) - \mathcal{F} \quad (2.156)$$

$$-m_i n_i \Omega^2 R \mathbf{e}_R = -\nabla P_i - n_i e (-\nabla \Phi_1 + \mathbf{U}_{1,i} \times \mathbf{B}) + \mathcal{F} \quad (2.157)$$

$$0 = -\nabla P_e - n_e e (-\nabla \Phi_1 + \mathbf{U}_{1,e} \times \mathbf{B}). \quad (2.158)$$

The friction force acting between two species is equal to the collisional drag felt by each species, and is proportional to the difference in the flow velocity of each species (including the parallel flow). It has the form

$$\mathcal{F}_{ab} = -m_a n_a v^{a/b} (\mathbf{U}_{1,a} - \mathbf{U}_{1,b}) - \frac{2}{5} m_a n_a v^{a/b} \left(\frac{\mathbf{Q}_a}{p_a} - \frac{\mathbf{Q}_b}{p_b} \right), \quad (2.159)$$

where \mathbf{U}_j represents the flow velocity of species j , and \mathbf{Q}_j represents the heat flux of species j . The heat flux \mathbf{Q} depends solely on the temperature gradient of the species, whereas the flow depends on pressure and temperature gradients and the higher-order potentials. The perpendicular component of the friction force \mathcal{F}_\perp is responsible for the classical diffusion, whereas the parallel component \mathcal{F}_\parallel is responsible for the neoclassical diffusion. Also, the general expression for the collision frequency of two species is given [Huba, 2004] by

$$v_0^{a/b} = \frac{4\sqrt{2\pi}}{3} \frac{n_b}{m_a} \left(\frac{1}{m_a} + \frac{1}{m_b} \right) \frac{Z_a^2 Z_b^2 e^4 \ln \Lambda}{(4\pi\epsilon_0)^2} \frac{1}{(V_{T,a}^2 + V_{T,b}^2)^{3/2}} \quad (2.160)$$

where m_i and Z_i are the mass and charge of the species i , Λ is the Coulomb logarithm, V_i is the velocity of the particle of species i , and T_i is the temperature of the species i . From this expression firstly, one can notice that the self-collisions of tungsten particles can be neglected

Chapter 2. Equilibrium Theory, Guiding-Center Orbits and Neoclassical Theory with Flows

if the impurity is in trace quantities as compared to the bulk ions, i.e. $n_W \ll n_i$. One can also notice that the dominant collisions present are those between the trace heavy tungsten particles and the background ions. These simplifications in the neoclassical physics faced by the heavy impurity ions leads to the idea that the impurity particles can be treated by a PIC approach in the trace density limit.

We know that the friction force \mathcal{F} for the impurities arises solely out of collisions with the background ions moving at a different flow velocity as compared to the impurities. Therefore, in PIC simulations, we can simulate the friction force by resolving the impurity particle velocities correctly in the frame of the flow velocity of the background ions in the collision operator of VENUS-LEVIS. The collision operator in VENUS-LEVIS is a Monte-Carlo collision operator implementation which simulates single-particle collisions with a thermal background plasma, i.e. a Maxwellian background that is at rest. The Monte-Carlo kicks are provided in Energy E and pitch λ . Given that, for a background plasma with flow, the distribution function is a Maxwellian shifted by the value of the flow velocity, the energy and pitch of the impurity particle supplied to the collision operator should include the change in frame corresponding to the flow of the background. A simplification arises from the fact that the flows driven by the electric potentials Φ_0 and Φ_1 remain the same for all species, and therefore both the impurity and background plasma distributions are shifted by the same velocity values for these flows. The only flow that differs is the flow that arises due to the pressure gradients $\mathbf{U}_{1,j}$ as the pressure gradients for the impurity and background species will be different. Calculating the background flow as explained in Section 2.3, we shift the impurity particle velocities by $\mathbf{U}_{1,j}$ and provide it to the collision operator to obtain the frictional dynamics. This is sufficient to simulate impurity collisional dynamics equivalent to the neoclassical dynamics described above, which is used as a benchmark.

2.8.1 Recovery of Known Neoclassical Results in a Rotating Axisymmetric Equilibrium

An important part of this work will be the recovery of known impurity steady-state profiles in a rotating axisymmetric equilibrium with the Monte-Carlo approach just described. The equations (2.156)-(2.159) can be solved, as in Ref. [Romanelli and Ottaviani, 1998] following a method similar to Ref. [Rutherford, 1974], to obtain the surface-averaged radial impurity flux $\langle \Gamma_W \cdot \nabla r \rangle$, under large aspect ratio conditions, and in the absence of temperature gradient effects, it is found to be

$$\begin{aligned} \langle \Gamma_W \cdot \nabla r \rangle_\psi = & -D_{PS}(1 + \mathcal{M}_*^2)^2 \langle n_W \rangle \times \left\{ \partial_r \ln \langle n_W \rangle - \left(1 - \frac{\mathcal{M}_*^2}{1 + \mathcal{M}_*^2} \frac{Z_i e n_i}{p'} \langle U_{1,i\theta} \rangle \right) \frac{Z_W}{Z_i} \partial_r \ln p_i \right. \\ & \left. - \frac{\tilde{m}}{m_*} \left(\frac{\mathcal{M}_*^2 (1 + 3\epsilon \mathcal{M}_*^2 + 2\epsilon \mathcal{M}_*^4) - R_0 \partial_r \epsilon \mathcal{M}_*^2}{R_0 \epsilon (1 + \mathcal{M}_*^2)^2} \right) \right\}, \end{aligned} \quad (2.161)$$

2.9. Summary of the General Theory Background

where D_{PS} is the stationary Pfirsch-Schlüter diffusion coefficient, $D_{PS} = 2e^2(T_i/Z_W e B_{\theta 0})^2$, and the angle brackets $\langle \rangle$ indicate surface-averaged quantities. The effective Mach number \mathcal{M}_* , and the masses \tilde{m} and m_* are defined as

$$\mathcal{M}_*^2 = \mathcal{M}_{0,W}^2 \left(1 - \frac{m_i T_e}{m_W (T_i + T_e)} \right), \quad \tilde{m} = m_W - Z_W m_i, \quad m_* = m_W - \frac{T_e}{(T_i + T_e)} m_i.$$

The averaged poloidal velocity $\langle U_{1\theta,i} \rangle$ in the absence of temperature gradients is

$$\langle U_{1,i\theta} \rangle = \left\langle \left\{ \left(\frac{g_2}{B^2} - \frac{\langle g_2 \rangle}{\langle B^2 \rangle} \right) + \frac{G_{PS}(\psi)}{\langle B^2 \rangle} \right\} \mathbf{B} \cdot \nabla \theta + \frac{\mathbf{B} \times \nabla \psi \cdot \nabla \theta}{B^2} \right\rangle \frac{p'_i}{Z_i e n_i}. \quad (2.162)$$

This value goes to zero for axisymmetry in all collisional regimes. For 3D, this may not be the case and will contribute to neoclassical effects.

The steady-state of the density profile can be obtained by setting the expression for radial flux to zero $\langle \Gamma \cdot \nabla r \rangle = 0$ and choosing a flat rotation profile, and we arrive at [Romanelli and Ottaviani, 1998]

$$\frac{\langle n_W(r) \rangle}{\langle n_W(0) \rangle} = \left(\frac{n_i(r)}{n_i(0)} \right)^{\left(1 - \frac{\mathcal{M}_*^2}{1 + \mathcal{M}_*^2} \frac{Z_i e n_i}{p'_i} \langle U_{1,i\theta} \rangle \right) Z_W / Z_i} \times \exp \left\{ \frac{\tilde{m}}{m_*} \frac{(3 + 2\mathcal{M}_*^2) \mathcal{M}_*^4}{(1 + \mathcal{M}_*^2)^2} \frac{r}{R_0} \right\}. \quad (2.163)$$

Thus, the steady state profile crucially depends on two factors: the presence of a poloidal flow, and the centrifugal effects of rotation.

In the absence of rotation with $\mathcal{M}_0 = 0$, we can arrive at an impurity density profile that has the form

$$\frac{\langle n_W(r) \rangle}{\langle n_W(0) \rangle} = \left(\frac{n_i(r)}{n_i(0)} \right)^{Z_W / Z_i}. \quad (2.164)$$

This implies that there is a very peaked impurity density even without rotation. One can see that the pressure dependent term in the RHS is the main contributor to the inward flux of the impurities. We use these expressions to benchmark impurity profiles in Chapter 4.

2.9 Summary of the General Theory Background

We have presented the aspects of various physics that will be used in the current thesis for application to calculation of the bootstrap current and the impurity accumulation. The next two chapters will focus on numerical results for various 3D applications, specifically on the bootstrap current with a saturated 1/1 internal kink mode, and on impurity transport with a toroidally rotating saturated 1/1 internal kink mode.

3 Effects of 3D on Bootstrap Current

The bootstrap current plays an important role in the steady-state function of future fusion devices, especially tokamaks such as ITER, as it reduces the dependence on external current drive, leading to savings in the input energy. Thus, it is of great interest to study the bootstrap current in existing fusion devices, under operational conditions similar to ITER. ‘

For tokamaks with steep edge pedestals, similar to those found in H-mode operations, the bootstrap current near the edge acquires a large value, significantly reducing the dependence on current drive. In TCV, operation of the tokamak with nearly 100% bootstrap current fraction due to bootstrap effect with ECCD has been demonstrated[Coda et al., 2007], leading to hopes that future tokamaks can achieve high bootstrap-current fractions. At the same time, plasma behaviour at and near the edge is crucial for the operation of a tokamak. The toroidal field ripple caused by the discretization of the toroidal magnetic field is a 3D effect that can play an important role in confinement of particles near the edge. Another example of such 3D effect on the edge is the Edge Localized Mode (ELM), which in short bursts, causes large degradation to the confinement of the plasma[Wingen et al., 2015]. Recently, the effort towards mitigating ELMs has concentrated on using Resonant Magnetic Perturbations (RMPs), to mitigate and control ELMs. However, large density pump-outs associated with ELM mitigation can cause a change in the edge bootstrap current. In addition to the 3D effects caused by externally imposed magnetic fields, the saturated 1/1 internal kink mode, also known in experimental plasma physics as Long Lived Modes (LLMs), is an intrinsic MHD instability in toroidally confined hybrid-type plasmas. The pressure barrier around the helical-core region can contribute significantly to the bootstrap current, and therefore, it is important to see to what extent the helical core affects the bootstrap current ordinarily associated with core localised pressure gradients.

In the current chapter, we attempt to undertake such self-consistent calculations of the bootstrap current in the 3D applications mentioned above. We use a self-consistent iterative scheme for the bootstrap current and employ two contrasting models to compute the bootstrap current. In particular, we wish to compare the performance of an axisymmetric model and a 3D model, as opposed to previous works which have only compared the validity compar-

isons of axisymmetric schemes[Belli et al., 2014b]. The iterative scheme yields the bootstrap current self-consistently starting from an ideal (2D and 3D) MHD equilibrium obtained from the VMEC code[Hirshman and Whitson, 1983]. The two distinctive models of bootstrap current we use are as follows: First, the *Sauter* model[Sauter et al., 1999] and second the *Shaing-Callen* model[Shaing and Callen, 1983, Shaing et al., 1986a], as described in Sec. 2.7. Both bootstrap current calculation models are applied to both 2D and 3D equilibria in this chapter, even though the *Sauter* model was originally derived for axisymmetric equilibrium calculations, and the *Shaing-Callen* is a neoclassical model valid for 3D equilibria. In the current work, we compare the performance of the two models for a variety of cases ranging from axisymmetric equilibria, to 3D equilibria incorporating the ideal response of RMPs to 3D equilibria with a helical core. This resultant bootstrap current is incorporated into the original toroidal current density profile, and iterated through VMEC again to generate a new equilibrium. The scheme is iterated until the bootstrap current profiles are sufficiently converged, resulting in a self-consistent magnetic equilibrium and its resultant bootstrap current profile. There have been apparently similar attempts to simulate bootstrap current using an iterative scheme on tokamaks and stellarators[Watanabe et al., 1992, Watanabe et al., 1995, Isaev et al., 2003]. However, each work has usually limited itself to using either an axisymmetric model or solely using a 3D model. The current work will compare and contrast the two bootstrap current models on 2D and 3D equilibria, obtaining novel, realistic bootstrap current calculations in tokamaks with field ripple, RMPs and helical cores.

This chapter is organised as follows: In section 3.1, we benchmark the bootstrap current formulations in the axisymmetric limit then proceed to consider weakly 3D equilibria, i.e. equilibria with toroidal field ripple and RMPs which pose a weak ideal equilibrium response, with an edge pressure pedestal. Next, in section 3.2, we consider a weak internal pressure barrier in the core region, however accompanied by a strongly 3D equilibrium. In the last section, Sec. 3.3, we summarise the results we observe and explain possible future works.

3.1 Edge Pedestal with Weak 3D effects: Toroidal Field Ripple and RMPs

In this section, we examine three distinct topics. Firstly, we benchmark the Sauter and Shaing-Callen formulations in the limit of axisymmetry. As shown in Sec. 2.7.3, the schemes must agree for axisymmetric equilibria and in Sec. 3.1.1 we will demonstrate the numerical agreement. Then we proceed to consider weakly 3D equilibria with Toroidal Field Ripple in Sec. 3.1.2 and Resonant Magnetic Perturbations (RMPs) in Sec. 3.1.3.

We begin by generating equilibria with an input pressure profile. We choose the pressure profile in a manner so as to represent the steep edge pedestals observed in H-modes in tokamaks (alternatively referred to as edge pressure barrier, as such steep profiles near the edge provide an edge transport barrier increasing the confinement of the plasma). In terms of

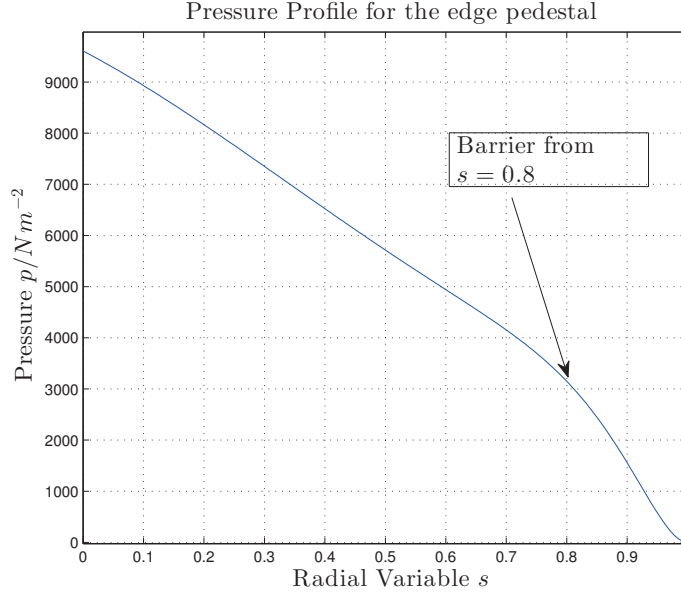


Figure 3.1 – The pressure profile is chosen so as to generate a VMEC equilibrium a steep edge pressure pedestal. Notice the pressure barrier starting at $s = 0.8$.

the radial variable s , the pressure and the density profiles are chosen to be:

$$p(s) = 10^4 \{0.6105(1-s)(1-s^2) + 0.3105(1-s^{10})^2\} Nm^{-3} \quad (3.1)$$

$$n(s) = 1.06 \cdot 10^{20} \{0.3105(1-s)(1-s^2) + 0.6333(1-s^{10})^2\} m^{-3} \quad (3.2)$$

respectively. The pressure profile succinctly allows for an edge pressure pedestal beyond $s = 0.8$, which can be seen in Fig. (3.1). Further, the density profile is deliberately chosen to be a similar form so as to obtain a smooth and relatively flat temperature profile near the edge. The temperature profile is calculated as $T(s) = p(s)/(2(n(s)))$, and as can be observed from Fig. (3.2), is relatively flattened in the edge region beyond $s = 0.8$. Additionally, we fix the density on the axis as $n_0 = 10^{20} m^{-3}$ and the temperature on the axis to be $T_0 = 0.6 keV$. These values ensure faithful representation of the kind of equilibria seen in MAST reasonably (Figs. 3.1,3.2).

We begin the first iteration of the iterative scheme by setting solely the Ohmic part as the total toroidal current I . The initial Ohmic current profile is chosen as

$$\langle \mathbf{J}_{\text{Ohm}} \cdot \nabla \phi \rangle(s) = I_{\text{total}} \frac{5}{12} (1-s-s^2+s^3) Am^{-2} \quad (3.3)$$

and we fix the total toroidal plasma current to $I_{\text{total}} = 0.48 MA$ (where the $5/12$ is the normalization factor for the chosen s polynomial). This prescription of pressure, density and temperature profiles is the initial condition for the calculation of the first equilibrium. The

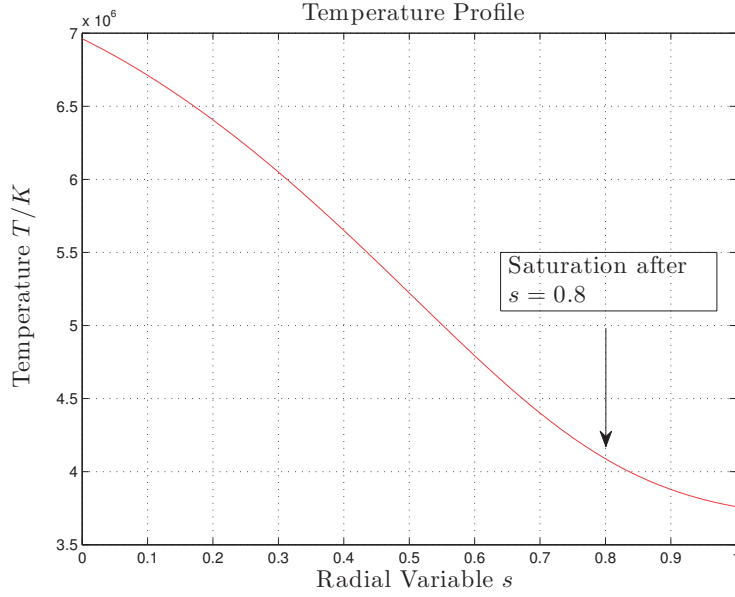


Figure 3.2 – The temperature profile is chosen so as to generate a VMEC equilibrium a steep edge pressure pedestal. The temperature profile flattens at $s > 0.8$ corresponding to the pedestal in pressure.

choice of our current density and pressure profiles determines the q -profile which plays an important role in the determination of the resonant rational surfaces which affects the bootstrap current densities calculated from 3D approaches. The associated q -profile can be seen in Fig. 3.3. With these profiles and axis parameters, we generate an equilibrium using VMEC. It is important to point out that the (s, u, v) coordinates of VMEC make calculations easy wherever harmonic decomposition is necessary. However, for the calculation of the bootstrap current, these coordinates necessitate additional averaging loops because of the fact that these are not field-aligned coordinates. This is computationally expensive as compared to using field-aligned coordinates for the averaging process. Therefore, as alluded to in the previous section, we convert the equilibrium to Boozer coordinates through the use of the TERPSICHOE package[Anderson et al., 1990].

The bootstrap current is then calculated through the use of the *Sauter* and *Shaing-Callen* formulae. The key idea, after this step is to scale and incorporate the bootstrap-current into the Ohmic current, thus prescribing the new current profile for the next iteration. This is subsequently iterated over with VMEC in order to generate a new equilibrium. The iterations are performed until convergence is reached to a required tolerance.

3.1.1 Benchmark with an axisymmetric MAST equilibrium

In order to benchmark the scheme, we first confine ourselves to axisymmetry. The VMEC free-boundary version[Hirshman et al., 1986] is used to generate an axisymmetric equilibrium

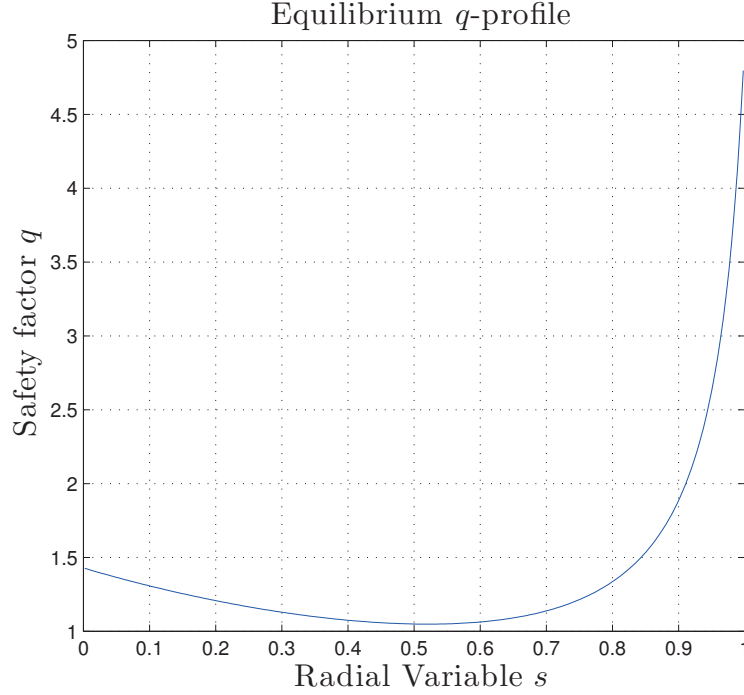


Figure 3.3 – The safety factor q -profile for the simulations for the chosen initial current and pressure profiles.

by allowing no toroidal modes except $n = 0$. This also makes sure that there are no resonant surfaces on which there can be singularities. Thus, we have the advantage of being able to examine the two bootstrap current models without the numerical effects of 3D magnetic equilibria. This allows us to compare the forms and magnitudes of the bootstrap current generated by each model.

In Fig. 3.4, we have plotted the bootstrap current density curves obtained from the Sauter formula from equations (2.115-2.119) described in Sec. 2.7.1, and the curve obtained from the Shaing-Callen formulation, described by equations (2.122-2.126) in Sec. 2.7.2. One can notice in Fig. 3.4 that even just after the first iteration, the Sauter and Shaing-Callen formulations prescribe bootstrap current density profiles which lie very close to each other, and follow the overall same shapes (which depend on the initial profiles we specified). In fact, the Shaing-Callen bootstrap current density agrees very well with the Sauter bootstrap current density. Therefore, we see that despite being prescribed by different schemes, the profiles lie very close to each other, as is expected from the axisymmetric agreement described in Sec. 2.7.3.

Further, it is of some interest to study the convergence of this scheme. In order to do so, as seen in Figs. (3.5,3.6), we iterate the scheme several times until a convergence is reached to a required tolerance. In general, as the Shaing-Callen scheme follows the Sauter scheme very closely in the axisymmetric limit, it is usually enough to seek convergence with respect to one of the prescriptions for the bootstrap current. The tolerance is defined as the relative

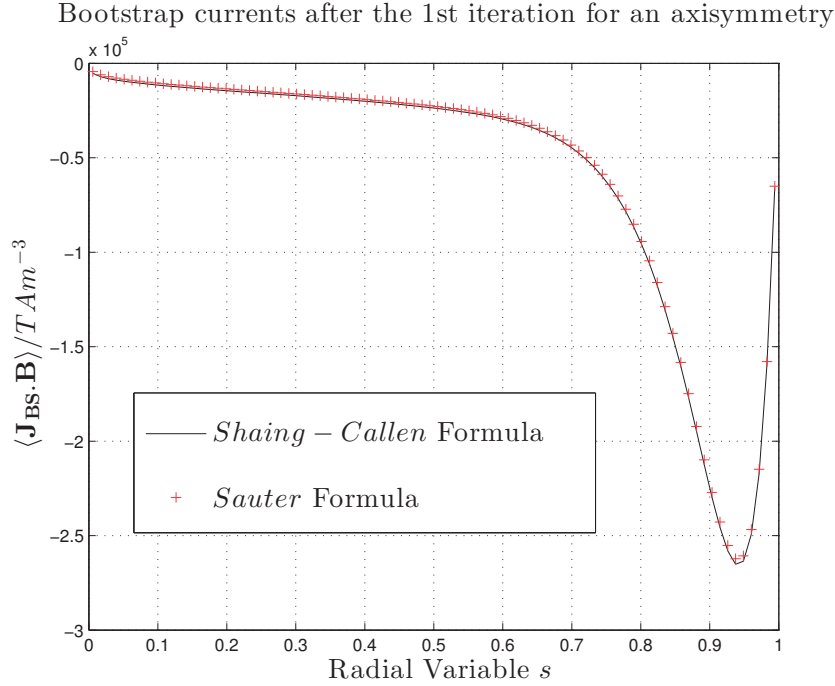


Figure 3.4 – Profiles of the parallel bootstrap current density $\langle \mathbf{J}_{BS} \cdot \mathbf{B} \rangle$ obtained according to the Sauter formula (the black curve) and the Shaing-Callen formula (red ‘+’ points).

difference between the current and the previous iteration. Unless otherwise mentioned, we fix a tolerance of 10^{-3} . We observe that, with each iteration, the bootstrap current approaches saturation. Beyond the fourth iteration, the tolerance is achieved, and the current profile can be considered to be sufficiently converged.

Another point which is very useful to consider is that even just after the second iteration, the form for the bootstrap current lies very close to the final form of the bootstrap current density profile. For computation of the bootstrap current density for 3D equilibria which are computationally expensive, one can use this fact as a heuristic to estimate the form of the bootstrap current profile, before proceeding to iterate and obtaining the profile more precisely.

3.1.2 Bootstrap Current for a 3D Equilibrium with Toroidal Field Ripple

In order to look at 3D effects on the bootstrap current density (and the total current), we generate MAST-like 3D equilibria using VMEC under free-boundary conditions, keeping the same pressure, temperature, Ohmic current and rotational-transform ι profiles. We generate equilibria, first to examine the effect of the number of toroidal field coils (the rectangular orange coils in Fig. 3.10) and hence the effect of varying toroidal field ripple near the edge (by changing coil currents), and then with varying current density in the RMP coils (the red discrete coils in Fig. 3.10) to simulate the ideal response to RMPs. For the following 3D cases with possible resonant q surfaces, there must be numerical resonance detuning performed, as

3.1. Edge Pedestal with Weak 3D effects: Toroidal Field Ripple and RMPs

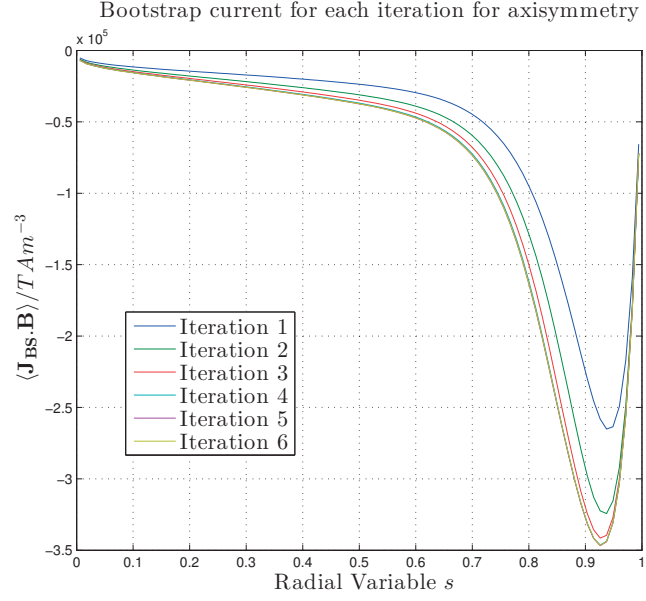


Figure 3.5 – Plot of *Sauter* parallel bootstrap current density $\langle \mathbf{J}_{BS} \cdot \mathbf{B} \rangle$ for each iteration of the bootstrap procedure. The profile for each n^{th} iteration is the input for the VMEC equilibrium calculation of the $(n+1)^{th}$ iteration.

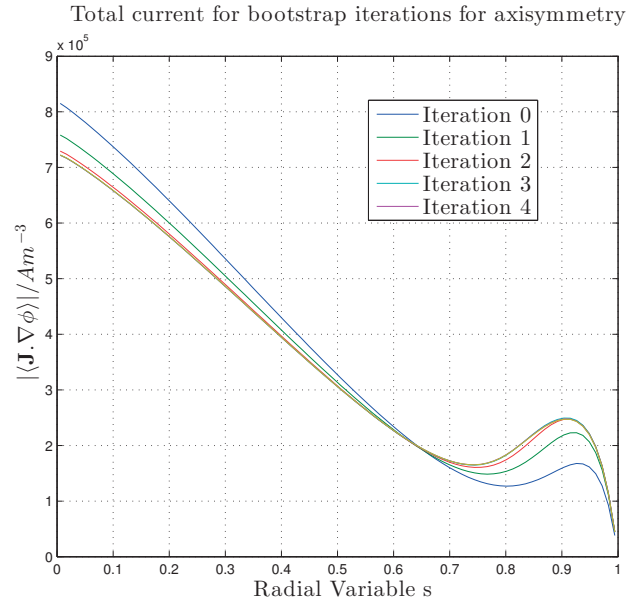


Figure 3.6 – Plot of the total current profile $\langle \mathbf{J} \cdot \nabla \Phi \rangle$ for each iteration of the bootstrap procedure. The profile for each n^{th} iteration is the input for the VMEC equilibrium calculation of the $(n+1)^{th}$ iteration.

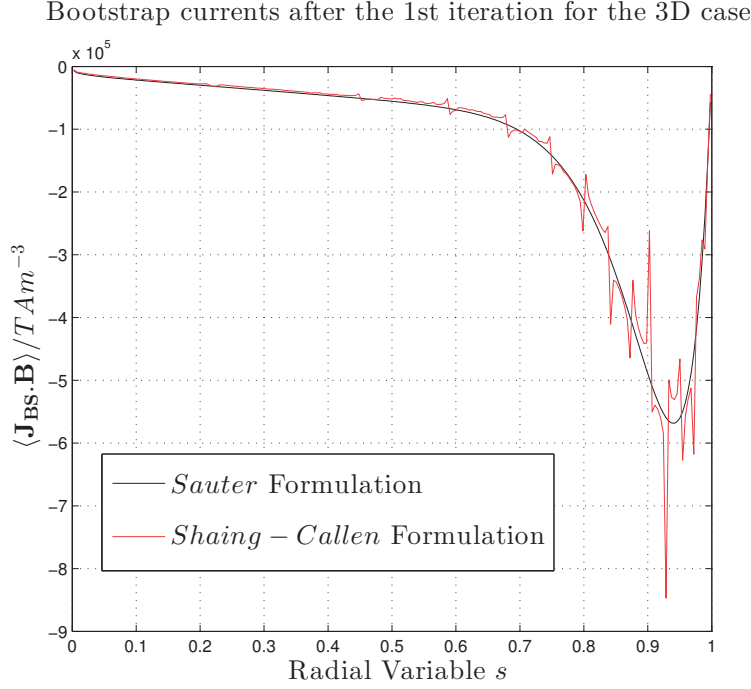


Figure 3.7 – Comparison of the *Shaing-Callen* formula and the *Sauter* formula for bootstrap current densities after the first iteration.

explained in Sec. 2.7.4 to numerically correct the resonances near the rational- q flux-surfaces. We proceed to fix the detuning factor to $\Delta = 10^{-4}$, unless mentioned otherwise. We can see in Fig. 3.7 that the Shaing-Callen derived bootstrap current now carries deviations from the axisymmetric Sauter model, as is expected from the 3D nature of the magnetic field. However, these deviations present themselves chiefly in forms of resonant spikes in the bootstrap current density profile. These spikes are caused by resonant rational q -surfaces, and in reality, represent parallel sheet currents, as seen in the side-by-side comparison in Fig. (3.8). It can be immediately noticed that there are major resonances distorting the edge bootstrap current profile at and around the $q = 2/1$ and $q = 3/1$ surfaces. These resonances are not avoidable because of the choice of the mode numbers and the effectively attained q -profile. (Additionally, we mention that the choice of the grid for averaging over the pitch λ in Eq. 2.131 plays little to no effect on the resonant spikes. We chose to implement several forms (linear, sinusoidal, hyperbolic) pitch grid between s , λ so as to concentrate a high sampling density near the trapped-passing λ for the pitch λ . We observe virtually no mitigation of the resonances with the change in the density of the pitch grid. The resonances are also not mitigated by increasing the resolution in the (θ, ϕ) physical grid used in equilibrium generation.)

However, we would still like to see whether these spikes can be removed by adequately adjusting the detuning factor Δ . In Fig. (3.9), where the value of Δ is varied, we see that above $\Delta = 10^{-4}$, the detuning causes the whole current density profile to change, distorting the current density profile itself. We observe, that the change in the profile becomes worse at

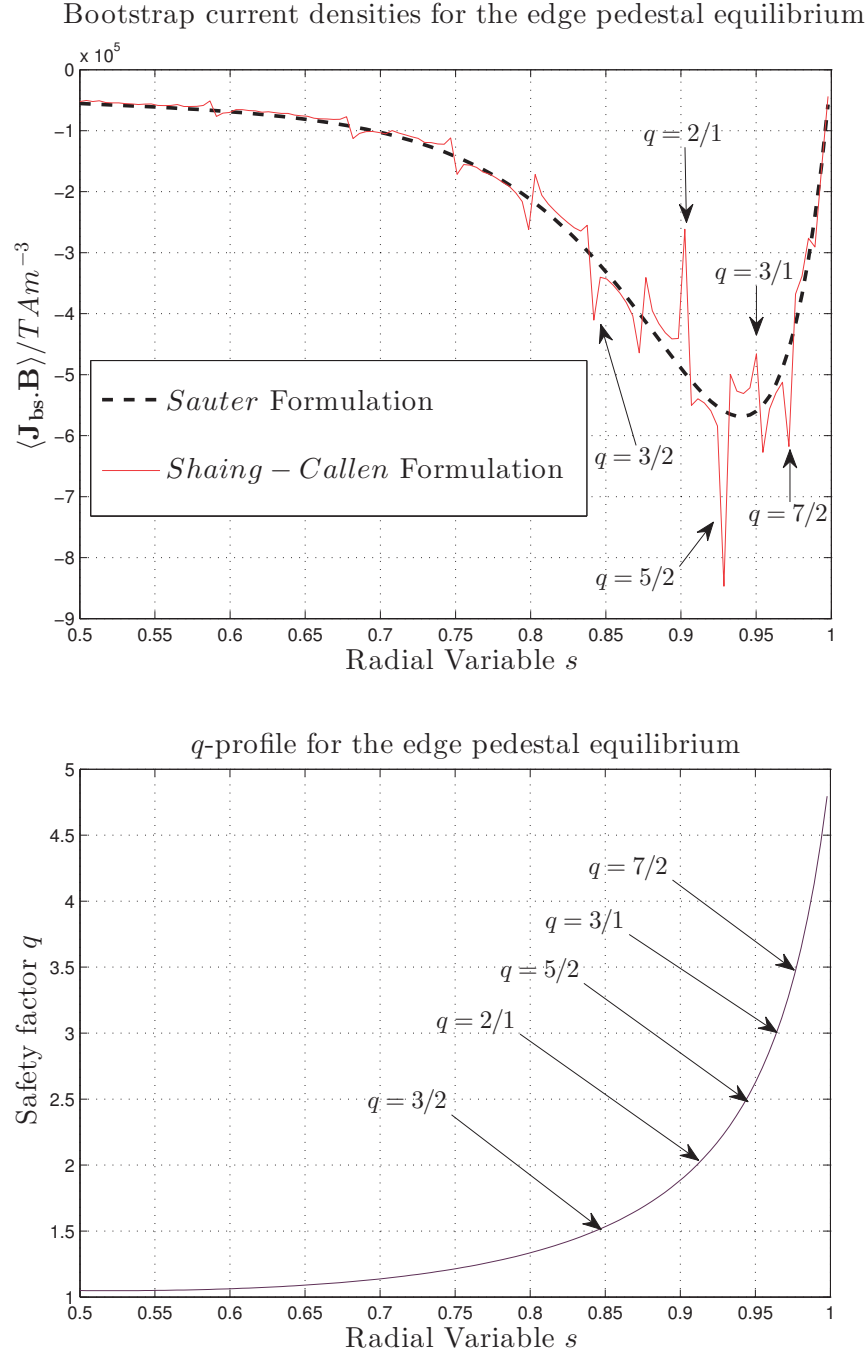


Figure 3.8 – A side-by-side comparison of the *Sauter* and *Shaing-Callen* bootstrap current densities with the q -profile. It can be seen that the spikes on the edge bootstrap current correspond to rational values of q on the profile.

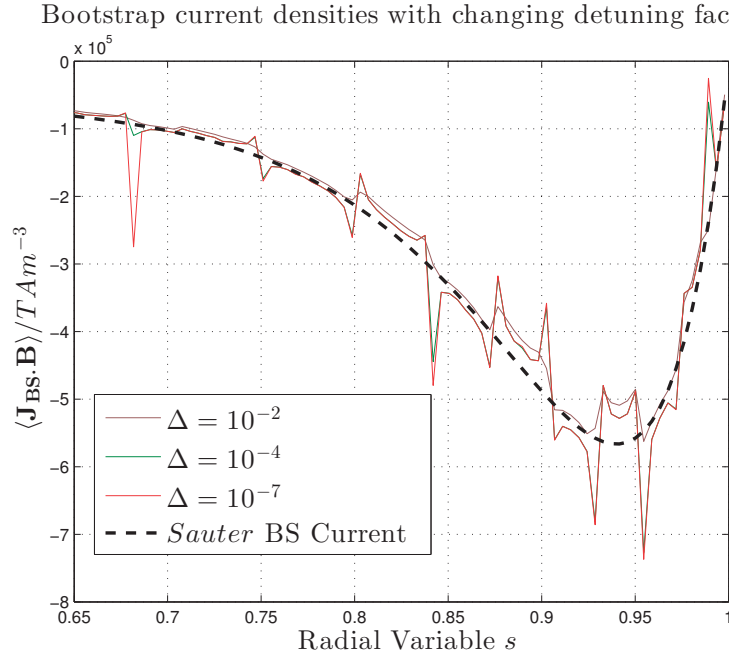


Figure 3.9 – The parallel *Shaing-Callen* bootstrap current density $\langle \mathbf{J}_{BS} \cdot \mathbf{B} \rangle$ for different values of detuning factor Δ . The dashed black line in the background is the *Sauter* bootstrap current. The bootstrap current density curve for $\Delta = 10^{-7}$ overlaps with the curve for $\Delta = 10^{-4}$.

Coil placement in MAST

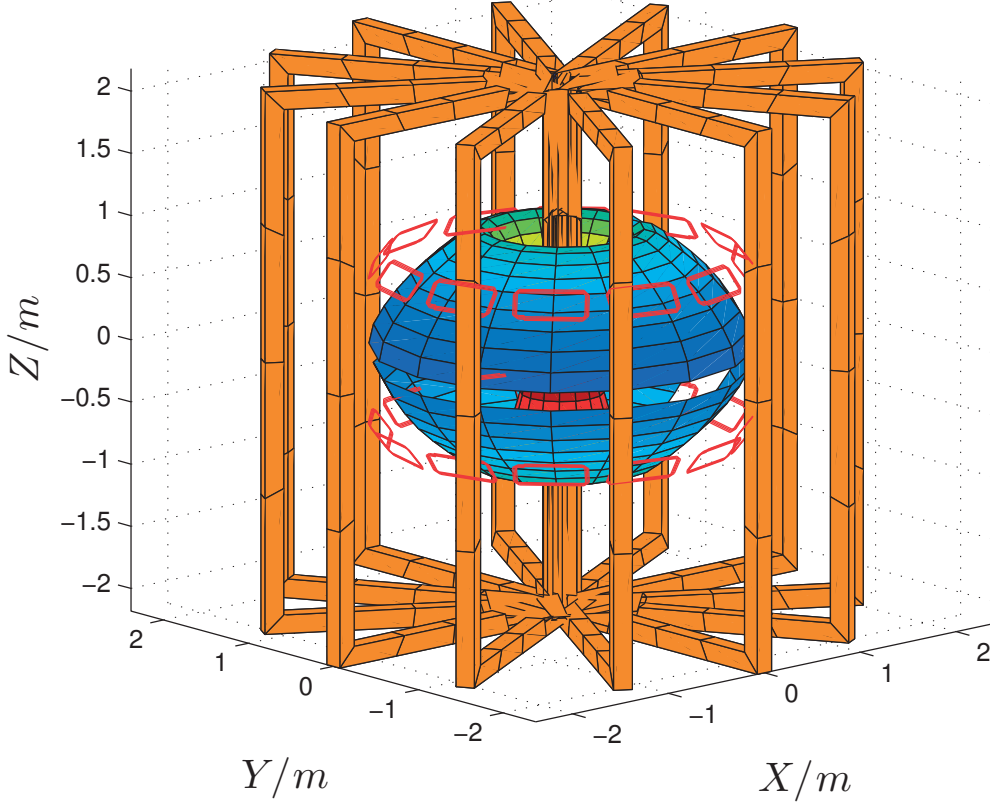


Figure 3.10 – Diagram depicting coil placement in MAST. The doughnut shaped figure is a plot of the magnetic field strength the last closed flux-surface of the equilibrium. The toroidal field coils are shown in orange, and the RMP coils are shown in red.

$\Delta = 10^{-2}$. And as we decrease below $\Delta = 10^{-4}$, we observe that the profile remains the same. Thus, the optimal value of the detuning factor seems to be 10^{-4} , as has been observed in previous literature[Turnbull et al., 2011]. However, even within the optimal range for the resonance detuning, the resonances are still present to the same order as the current.

It is hoped as we increase the number of toroidal field coils (referred to as ‘TF-coils’ from here onwards), we approach an equilibrium closest to an axisymmetric equilibrium, avoiding some large q resonances. In order to investigate whether some resonance stemming from the toroidal field ripple can be suppressed, we choose to change the number of toroidal field coils (TF-coils), modeled in VMEC, in order to observe the change in the bootstrap current density profile. In MAST, there are 12 TF-coils (seen in Fig. 3.10), which in itself presents a considerably small field ripple. In order to increase the ripple, we decrease the number of TF-coils to 6, and

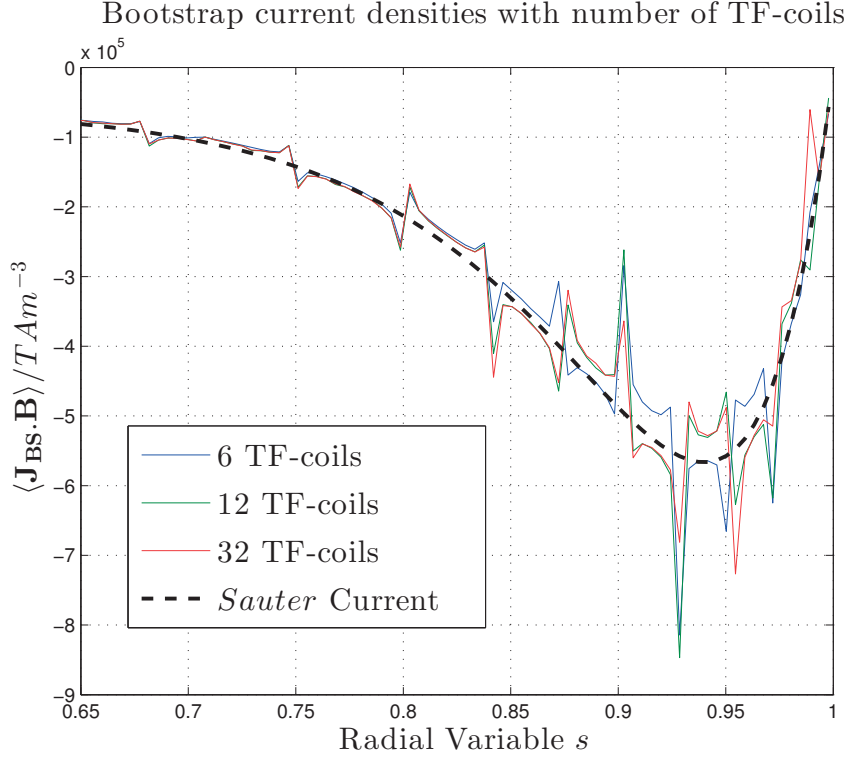


Figure 3.11 – The effect of increasing TF-coil numbers on the parallel *Shaing-Callen* bootstrap current densities. The resonance detuning factor is fixed at $\Delta = 10^{-4}$. The black dashed curve represents the *Sauter* bootstrap current density for the same Δ .

in order to decrease the ripple to get as an axisymmetric toroidal field as possible, we increase the number of TF-coils to 24 and 32. This allows us to examine the effect of the toroidal field ripple on the bootstrap current, and the particular resonances it undergoes.

The coil positions can be specified to VMEC using another package in the VMEC-Suite called MAKEGRID. MAKEGRID can define the magnetic-field strength of the TF-coils to any specified precision and to any specified number of modes. This is an important point to keep in mind, as increasing the number of coils would subsequently require an increase in the number of required toroidal modes, in order to maintain the same order of accuracy as in the tests with a lower number of TF-coils. Also, the current in the coil has to be proportionally compensated corresponding to the number of coils being used in order to maintain the same field strength.

We notice from Fig. 3.11 that when the number of TF-coils is decreased to 6, there is a change in the bootstrap current profile, though the net difference from the axisymmetric value does not significantly increase. In addition, we can see more spikes for the case with 6 TF-coils, which implies that a larger ripple causes more resonances, and hence more spikes. However, as can be seen in the figure, these additional spikes appear at mid-radius region, where the bootstrap

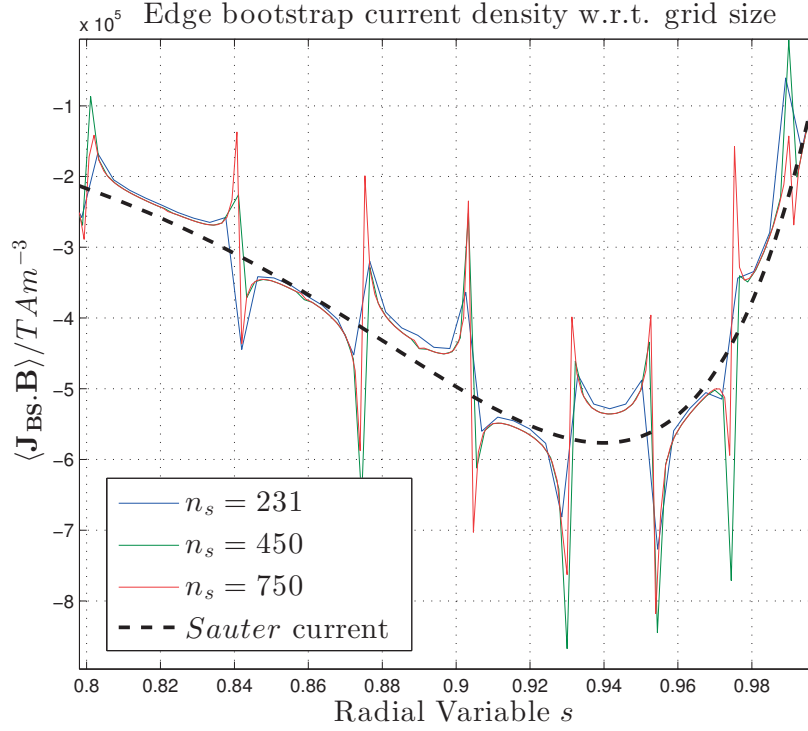


Figure 3.12 – A plot of the bootstrap current density, for the case of 32 TF coils, for increasing sampling in radial variable s . We have especially zoomed in between the near-edge region $s = 0.8 - 1.0$. It is immediately noticeable that the increase in the sampling produces neither a significant amelioration of the numerical resonance, nor do the non-resonant portions differ significantly.

current is weak. However, the increase in the number of TF-coils beyond 12 does neither affect the bootstrap current density curve, nor the particular spikes observed in the density profile. Thus, we conclude that the number of TF-coils does not play any significant role on the form or order of the bootstrap current. In all the cases beyond 12 TF-coils, we do not see a difference in the bootstrap current density curve. For all the cases considered, including the case with 6 TF-coils where a strong ripple ensues at the edge of the plasma, the *Shaing-Callen* bootstrap current density curve closely follows the axisymmetric *Sauter* bootstrap-current density curve, except for the spikes observed at the resonant q -rational surfaces. It is reasonable to hypothesize that if these spikes were not present, the curves agree closely with the axisymmetric case. It is therefore reasonable to conclude that the 3D *Shaing-Callen* model is as good as the axisymmetric *Sauter* model, for the cases with a steep edge pedestal and toroidal field ripple.

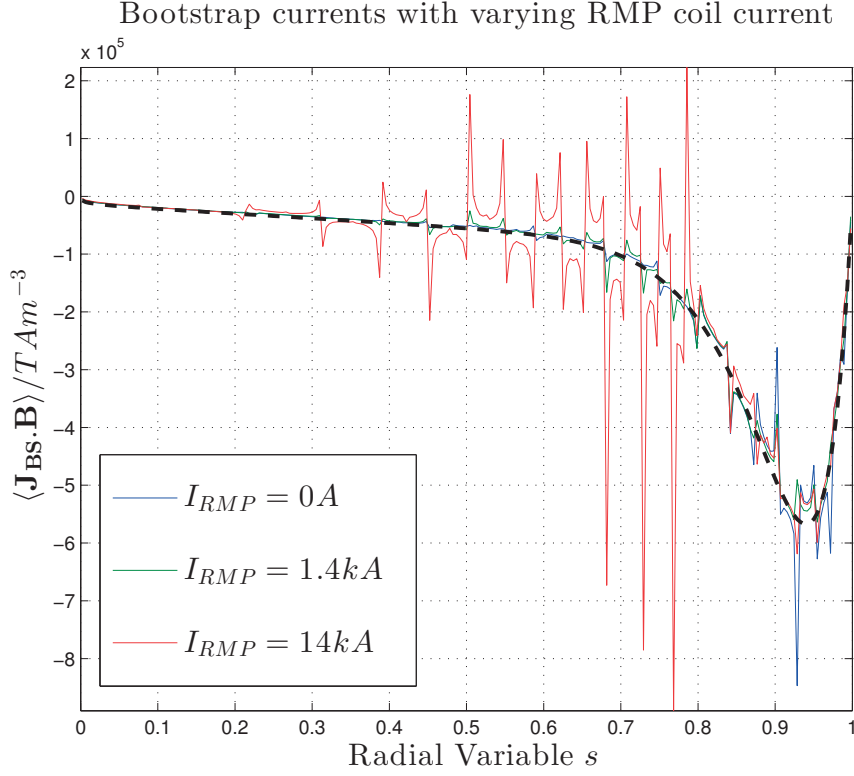


Figure 3.13 – The parallel *Shaing-Callen* bootstrap current density $\langle \mathbf{J}_{BS} \cdot \mathbf{B} \rangle$ as calculated for 12 TF-coils for a MAST 3D equilibrium with varying RMP currents. The black dashed curve represents the *Sauter* bootstrap current. The resonance detuning factor is set to $\Delta = 10^{-4}$. Note in particular the higher (m, n) mode number resonances caused in the mid-radius.

3.1.3 Bootstrap Current for a 3D Equilibrium with RMPs

Additionally now, we would like to learn if any relevant physics can be extracted under the same weak 3D conditions. RMPs play an important role in mitigating ELMs, and therefore the effects of ideal RMP fields on the bootstrap current are important to examine. We apply RMPs to the same VMEC equilibrium and get equilibria corresponding to the ideal response of the RMP fields. The RMP coils, again, are specified through the MAKEGRID package. Now, in order to check the effect of the RMP fields on the bootstrap current, we progressively increase the value of the bootstrap current from $0 kA$ to $14 kA$. In MAST, the order of currents used in the RMP coils is usually $1 kA$. In our scan, the value closest to realistic values would be around $1.4 kA$. It is worth mentioning that the $14 kA$ case is purely academic, in order to examine an extreme-case ideal RMP response might cause to the edge bootstrap current. The RMP coils, as seen in Fig. 3.10, are chosen so as to create an $n = 3$ perturbation.

We notice that beyond a certain value of the RMP current, there is virtually no difference in the bootstrap current at the edge, and that the bootstrap current remains virtually unchanged between the RMP-coil current values of $I_{RMP} = 0 A$ and $I_{RMP} = 1.4 kA$. The RMP-coil current

3.2. Internal Pressure Barriers with Strong 3D effects: Saturated 1/1 internal kink

values lying in between these values correspond to a bootstrap current curve that lies in between the blue and green curves in Fig. 3.13.

We notice that the bootstrap current therefore is not significantly different at the edge. However, in the $s = 0.3 - s = 0.8$ region, there is a significant effect on the 3D *Shaing-Callen* bootstrap current. This is expected of an $n = 3$ perturbation to penetrate more deeply towards the axis. Therefore, we conclude a negative result, that RMPs do not affect the edge bootstrap current significantly. However, when we assume (an unrealistic) value of RMP-coil current at $I_{RMP} = 14 \text{ kA}$, we see that the parallel current spikes in the region between the edge and the axis are more strongly affected than the edge itself. We see, in general, that the parallel current spikes grow with the increasing RMP-coil current, therefore distorting the bootstrap current profile significantly and preventing us from extracting any significant results in this region of interest. Again, the 3D model does not offer any insight here. Thus the axisymmetric model is as good as the 3D model for the 3D equilibria with steep edge pressure barrier.

3.1.4 Summary of Bootstrap Current in Axisymmetry with RMPs and Toroidal Ripple

The conclusions of the previous section can be summarised as follows. There is an excellent agreement between the Sauter and Shaing-Callen formulations under the limit of axisymmetry, as is expected from standard neoclassical theory. Furthermore, it can be confidently stated that the axisymmetric Sauter model is robust to weak 3D ideal perturbations, like toroidal field ripple and resonant magnetic perturbations, when the 3D equilibrium is near axisymmetry, where the Shaing-Callen model can undergo multiple resonances near the edge. The resonance detuning has a limited effect on the bootstrap current profile and has a favourable range ($\Delta = 10^{-4} - \Delta = 10^{-6}$) where enough resonance damping is provided without affecting the overall profile. Therefore, for equilibria with weak 3D ideal response, it is prudent to use the Sauter model and reduce computational time. Hence, the Shaing-Callen model is desirable with 3D modes that do not undergo rational- q resonances, which is considered in the next section where we examine the non-resonant 1/1 internal kink mode.

3.2 Internal Pressure Barriers with Strong 3D effects: Saturated 1/1 internal kink

A saturated 1/1 internal kink is known in experimental plasma physics as a long-lived mode (LLM) MAST[Chapman et al., 2010, Chapman et al., 2014] or informally as a helical-core. The deformation of the flux-surfaces near the core twist around helically with the toroidal angle. The helical core extends up to the point where the safety factor q is the minimum (q_{min}) or alternatively till where the rotational transform is maximum (t_{max})[Brunetti et al., 2014]. Beyond that, the flux-surfaces are quickly assume axisymmetry, and the region enclosing the helical core is termed here as the axisymmetric mantle. They play an important role

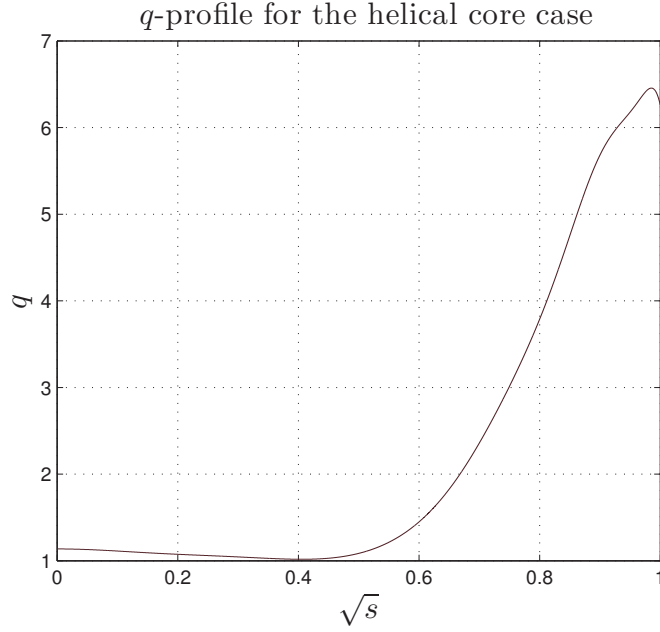


Figure 3.14 – The rotational transform ι profile chosen to generate a helical core.

in the functioning of machines such as MAST and JET, and future fusion devices like ITER. Helical-core equilibria can be generated in VMEC[Cooper et al., 2010] by providing an initial $n = 1$ distortion on the magnetic-axis which leads to the formation of an appropriate helical core.

3.2.1 Bootstrap Current for a Saturated 1/1 Internal Kink

We begin by fixing the rotational transform $\iota = 1/q$ profile, and letting the current profile free in VMEC. In order to avoid resonance, we choose a ι -profile which avoids major resonant surfaces in the helical-core region and peaks slightly below $\iota = 1$. Additionally, the pressure profile is chosen so as to provide a weak internal pressure barrier in the helical core region. Having fixed the q -profile, and not the current density profile $2\pi\langle\mathbf{J}\cdot\nabla\Phi\rangle$, we only perform the first step of the iteration to obtain the form of the bootstrap current profile. Following from benchmarks in the superseding section, we can safely assume that the first iteration itself will bring the bootstrap current current density profile sufficiently close to the converged value.

The ι -profile is chosen to peak around $s = 0.2$ with a low shear region between $s = 0 - 0.2$ (seen in Fig. 3.14). The edge of the helical core extends up to the point at which q -profile transitions from a low-shear to a high-shear region, indicating that the helical core extends until $s \sim 0.2$, seen from Fig. 3.14. Beyond that, the equilibrium is effectively axisymmetric. Further the pressure profile in the helical core-region is chosen to be reasonably steep, thereby providing a weak pressure gradient in the helical-core region, as seen in Fig. 3.15 The temperature profile is chosen to be constant at $T = 640\text{keV}$, thus making the pressure profile of the same form as

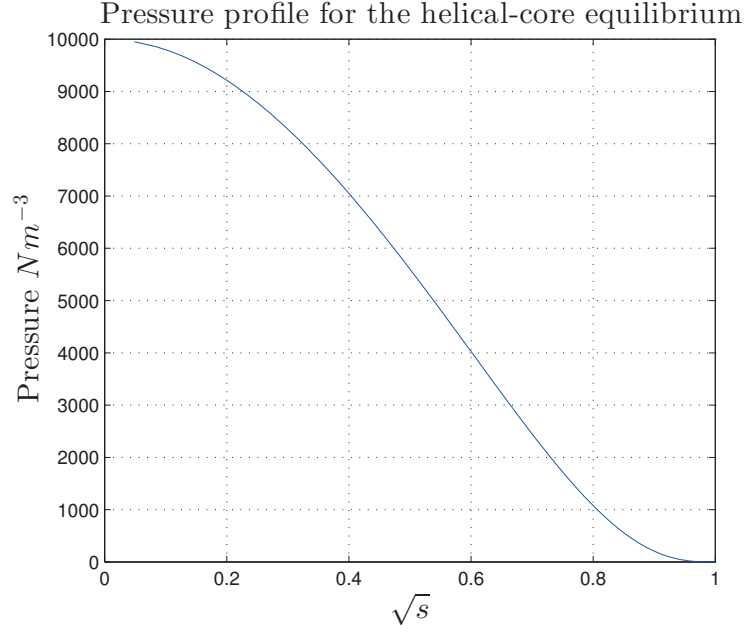


Figure 3.15 – The chosen density profile in order to produce a helical core equilibrium. We can see that in the helical core-region up to $s = 0.2$, there is a steep density (and hence, pressure) gradient, providing a weak internal pressure barrier.

the density profile. With these, we generate a 3D equilibrium with a helical core, which can be seen in Fig. (3.16).

Using the above-mentioned profiles, we start by benchmarking the case against a 2D axisymmetric sister equilibrium. In order to create this axisymmetric analogue equilibrium, we force only one toroidal mode $n = 0$, which forces VMEC to have an axisymmetric magnetic axis around which to form an equilibrium. This axisymmetric equilibrium is similar in all aspects with its helical core sister-state except for the presence of a helical skew in the core till $s = 0.2$, which can be seen in Fig.3.18. We perform our bootstrap current density calculations on this axisymmetric equilibrium using the *Sauter* and *Shaing-Callen* models. One can see in the Fig. (3.18), that again, we see an excellent agreement between the two models to within 5%. It can be observed that the form of the *Sauter* bootstrap current density is modulated chiefly from the pressure gradient dp/ds and the trapped fraction f_t . In the helical core region $s < 0.2$, the trapped fraction f_t is the chief contributor to the form of the bootstrap current, taking it abruptly towards zero as it approaches the magnetic axis. Again, the *Shaing-Callen* bootstrap current density also closely follows the *Sauter* bootstrap current density. We observe no resonant contributions because of the lack of $n \neq 0$ modes in the computation of the geometrical factor G_b .

Having found a similar agreement as the previous edge pressure barrier case for axisymmetry, we move on to compute the 3D helical core equilibrium with a skewed magnetic axis and an axisymmetric free boundary. With the finely chosen q -profile to avoid major resonances in

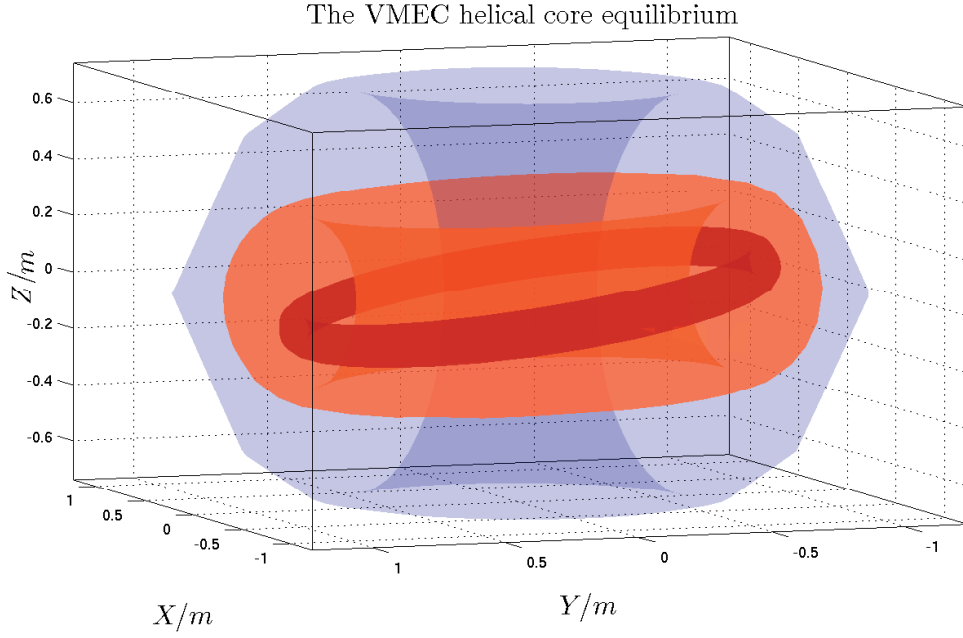


Figure 3.16 – The helical core equilibrium obtained from VMEC for the specified ι -profile and pressure profile. One surface from inside the helical core ($s = 0.1$), one from near the internal axisymmetric boundary ($s = 0.25$) and the last from the edge ($s = 1$) are shown here for reference.

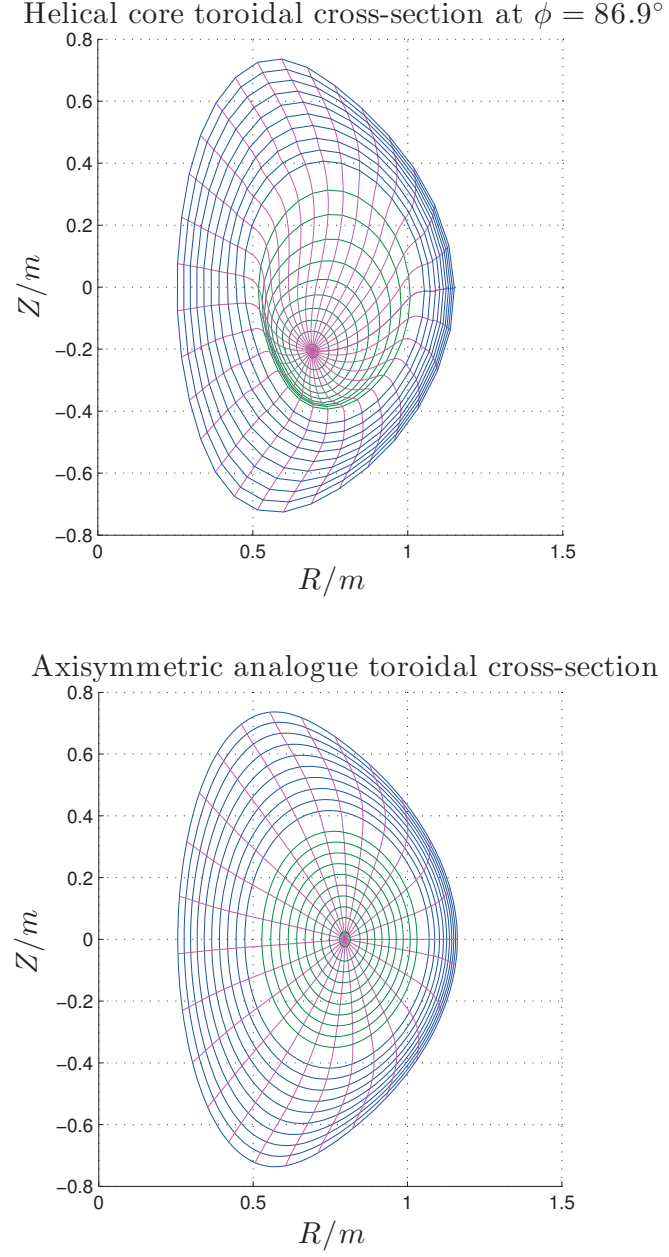


Figure 3.17 – A comparison of toroidal cross-sections of (s, u, v) coordinate grids for the helical core equilibrium and its axisymmetric sister-state. The magenta coloured lines are lines of constant poloidal angle variable u . The helical core region is represented by green coloured lines of constant s , and the axisymmetric mantle is represented by blue coloured lines of constant s .

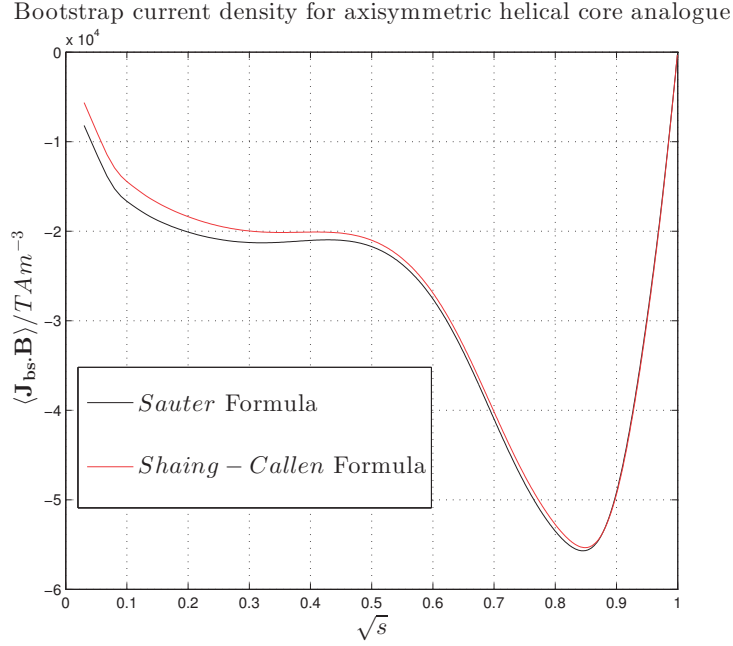


Figure 3.18 – The bootstrap current densities calculated for the axisymmetric analogue equilibrium for the chosen helical core parameters.

the helical core region, we compute the *Sauter* and *Shaing-Callen* bootstrap current densities. The resonance detuning parameter is set at $\Delta = 10^{-4}$, as per the optimal detuning parameter value obtained in the previous case. We notice from Fig. 3.19, that in the helical core region, there are no major resonance contributions, leading to a smooth bootstrap current density curve with the *Shaing-Callen* prescription. However, even as we move a small distance outside of the helical core, at the beginning of the axisymmetric mantle, we notice spikes caused by the ι -profile crossing major resonant surfaces despite the fact that in this domain the 3D deformations are very weak. In the axisymmetric mantle, there is an agreement between the two formulations similar to what was seen for the edge pressure pedestal case, rife with major resonance contributions.

Crucially, the bootstrap current densities prescribed by the *Sauter* formulation and the *Shaing-Callen* formulation in the helical-core region are visibly different. In particular, we notice that the current prescribed by the Sauter formulation is non-zero on the magnetic-axis whereas it tends to zero as prescribed by the Shaing-Callen formulation. We proceed to investigate the origins of the difference between the two bootstrap current prescriptions in the helical core region.

3.2. Internal Pressure Barriers with Strong 3D effects: Saturated 1/1 internal kink

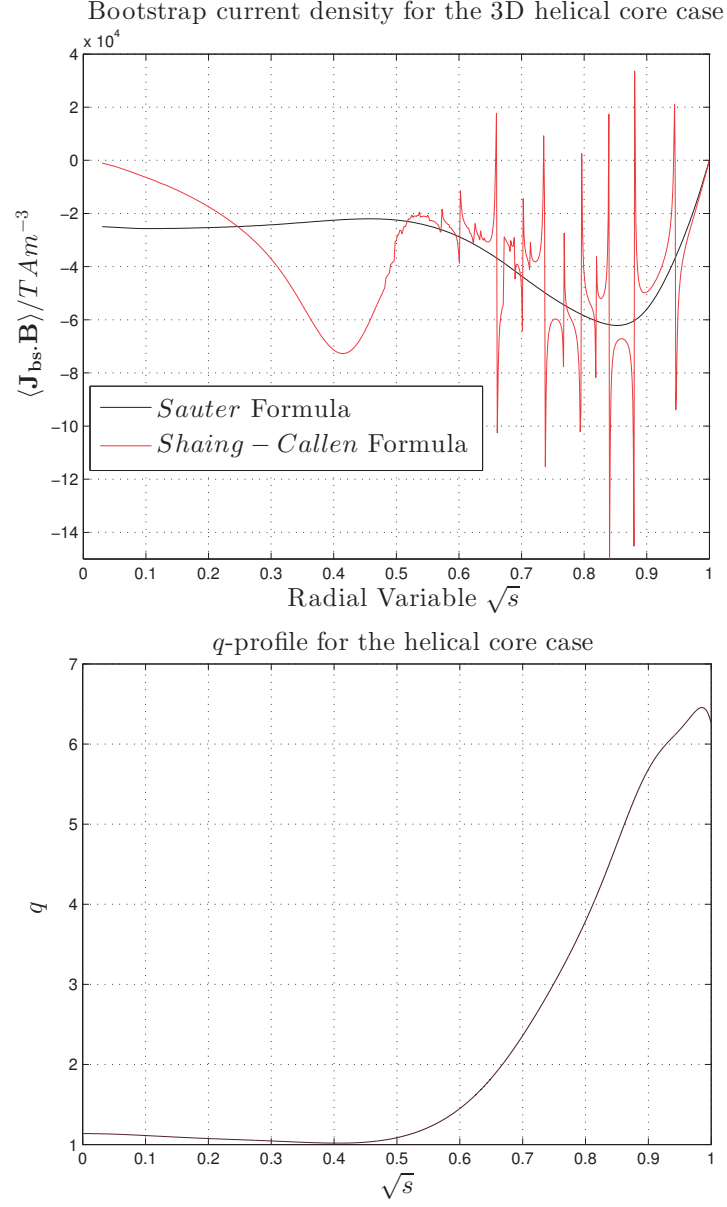


Figure 3.19 – We choose a q -profile which avoids major resonant surfaces in the helical-core region. The figure above represents the bootstrap current profiles specified by the *Sauter* and *Shaing-Callen* formulations respectively and the figure below shows the chosen ι -profile.

3.2.2 Comparison of the Sauter and Shaing-Callen Formulations: Particle Trapping and Geometry

The *Sauter* bootstrap current density depends on the values of I/ψ' , and the coefficients L_{31} , L_{32} and L_{34} . From the Eqs. (2.116)-(2.119), it can be immediately noticed that the L -coefficients are dependent on the trapped fraction f_t . An approximation for the trapped fraction [Sauter, 2016] in terms of the triangularity δ , the inverse aspect-ratio ϵ is given by

$$\epsilon_{eff} = 0.67 (1 - 1.4 \delta |\delta|) \epsilon, \quad (3.4)$$

$$f_{t,approx} = 1 - \frac{1 - \epsilon_{eff}}{1 + 2\sqrt{\epsilon_{eff}}} \sqrt{\frac{1 - \epsilon}{1 + \epsilon}}, \quad (3.5)$$

$$f_{t,approx} = \min(1, f_{t,approx}(\text{Eq. (3.5)})). \quad (3.6)$$

Now since $s = (r/a)^2$, r and a being the minor radius and maximum minor radius respectively, and thus r/R being the inverse aspect-ratio of the flux-surface in concern, we compute the approximate axisymmetric trapped fraction $f_{t,approx}$, through the values of ϵ and δ obtained from the VMEC equilibria. In addition, it is also possible to calculate the exact flux-surface averaged trapped fraction for the given axisymmetric VMEC equilibrium using Eq. 2.120. A comparison between the exact trapped fraction and the approximate trapped fraction can be seen in Fig. (3.20). The two axisymmetric trapped fractions follow each other quite closely as expected. Importantly, the exact trapped fraction f_t for the 3D helical core (Fig. (3.20)), f_t does not approach zero towards the magnetic axis, and it is for this reason that the *Sauter* model yields non-zero bootstrap current on the axis (see Fig. (3.18)).

For the 3D VMEC helical core equilibrium, the skewed magnetic axis has a variation in the radial R and azimuthal Z directions. This causes a variation in the absolute magnetic field $|B|$, and therefore allows for the formation of a local magnetic well on the magnetic axis where the particles can get trapped. By following a similar approach as in Ref. [Wesson and Campbell, 2011], the particle gets trapped when its parallel velocity vanishes $w_{\parallel} = 0$. Therefore,

$$w_{\parallel}(x)^2 + w_{\perp}(x)^2 = w_{\perp}(x_{bounce})^2, \quad (3.7)$$

where w_{\parallel} is the parallel velocity of the particle, and the subscript 'bounce' refers to the bounce point on the arbitrary coordinate x . From the conservation of the magnetic moment, we have

$$\frac{w_{\perp}(x)^2}{B(x)} = \frac{w_{\perp}(x_{bounce})^2}{B(x_{bounce})}. \quad (3.8)$$

Now, at the trapped-passing boundary of the particles, the bounce point is the point with the maximum magnetic field intensity. Therefore, at the trapped-passing boundary, we have

$$w_{\parallel}(x_0) = w_{\perp}(x_0) \left(\frac{B_{max}}{B(x)} - 1 \right)^{1/2} \quad (3.9)$$

3.2. Internal Pressure Barriers with Strong 3D effects: Saturated 1/1 internal kink

where subscripts 0 and max refer to the initial position and position of maximum magnetic fields respectively. A particle would be trapped for a value of $w_{\parallel}(x_0)$ less than the RHS, and vice-versa for a passing particle. Assuming a distribution F in $(w_{\parallel}, w_{\perp})$, the density of trapped particles n_t would be given by

$$n_t = 4\pi \int_0^{\infty} dw_{\perp} w_{\perp} \int_0^{w_{\parallel}(x_0)} dw_{\parallel} F(w_{\parallel}, w_{\perp}), \quad (3.10)$$

where the trapped fraction now becomes $f_t = n_t/n$. Assuming a Maxwellian distribution in $(w_{\parallel}, w_{\perp})$, the trapped fraction becomes

$$f_t = \frac{n_t}{n} = 4\pi \left(\frac{m}{2\pi T}\right)^{3/2} \int_0^{\infty} dw_{\perp} w_{\perp} \exp\left\{-\frac{mw_{\perp}^2}{2T}\right\} \int_0^{w_{\parallel}(x_0)} dw_{\parallel} \exp\left\{-\frac{mw_{\parallel}^2}{2T}\right\} \quad (3.11)$$

which is a nested integral. In the limit of small $w_{\parallel}(x_0)$, the integral in w_{\parallel} integrates to a value of $w_{\parallel}(x_0)$. The trapped fraction can then be integrated to

$$f_t(x_0) = \left[\frac{B(x_0)}{B_{max}} \left(\frac{B_{max}}{B(x_0)} - 1 \right) \right]^{1/2}. \quad (3.12)$$

If the arbitrary variable x is the helical angle $\chi = (\theta - \phi)$, and consider a skewed magnetic axis with a magnetic field of the form

$$B \sim B_0 - \frac{\delta r_{hel}}{R_0} \cos \chi, \quad (3.13)$$

then the local trapped fraction can be averaged over χ to obtain the trapped fraction on the magnetic axis $f_{t,approx,hel}$

$$f_{t,approx,hel} = \frac{2}{\pi} \left(\frac{2\delta r_{hel}}{R_0} \right)^{1/2} \quad (3.14)$$

where δr_{hel} is the displacement of the magnetic axis. From the equilibrium data, we find $\delta r_{hel} \approx 0.18$, which makes the trapped fraction on the axis $f_{t,approx,hel} \approx 0.6$, which is consistent with what we observe in Fig. 3.20. The disparity in the 2D and 3D exact trapped fractions is very low in the axisymmetric mantle and therefore the agreement between the *Sauter* and *Shaing-Callen* formulations outside of the helical core region still remains of the order observed in Figures (3.18) and (3.19). It must also be mentioned that the collisionality towards the magnetic axis is typically not negligible, and the trapped fractions are reduced by the order of the collision frequency of the species [Sauter et al., 1999]. This helps drive the trapped fraction to a lower value near the magnetic axis for the 3D case, which would in turn modulate the *Sauter* bootstrap current density to a lower value at the axis. However, this wouldn't affect the shape of the current density curve away from the magnetic axis, and the difference observed among the two bootstrap models will remain significant.

As for the *Shaing-Callen* bootstrap current density formulation, the coefficients again depend

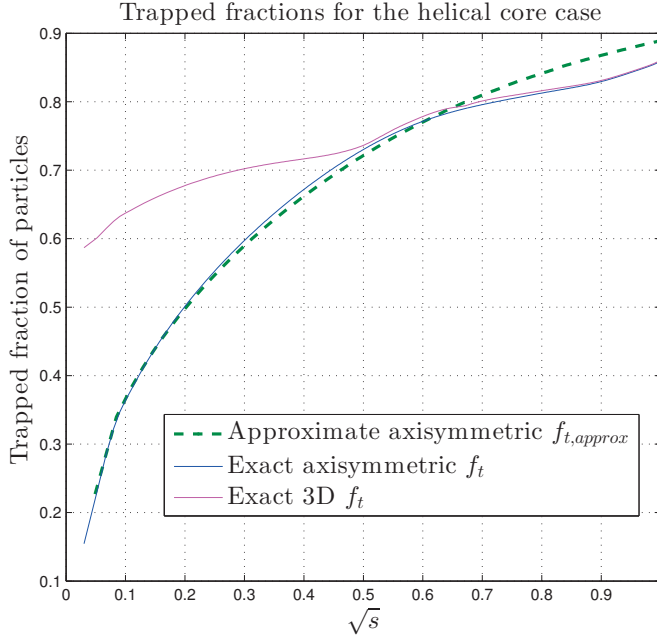


Figure 3.20 – A comparison between the exactly calculated trapped fraction f_t and the trapped fraction calculated under axisymmetric conditions for the vacuum form of the magnetic field $f_{t,approx}$ for the helical core case.

on the neoclassical viscosity coefficients and the trapped fractions. However, as we have seen earlier, the trapped fractions do not approach zero, and from Ref.[Johnson et al., 1999], the viscosity coefficients are constants. Therefore, the key contribution to the modulation of the form of the bootstrap current density curve arises from the geometrical factor G_b . Firstly, because of the $q \gtrsim 1$ low-shear region in the helical core, there is an augmentation in the geometrical factor because of the parallel gradients $\mathbf{B} \cdot \nabla$ approaching, but never reaching, zero. This near-resonance causes the helical-core bootstrap current to be augmented in the helical core region as compared to the axisymmetric version, as seen in Fig. 3.22.

We observe, from Fig. (3.21), that the geometrical factor for the helical core approaches zero towards the magnetic axis. The geometrical factor G_b , as evidenced from Eqns. (2.131) and (2.132)-(2.135), depends on the flux-surface averaged coefficients $\langle g_2 \rangle$ and $\langle g_4 \rangle$, which subsequently depend on $\mathbf{B} \cdot \nabla \mathbf{B}$ and $\mathbf{B} \cdot \nabla g_1$ respectively. For axisymmetry, on the magnetic axis throughout which the value of $|B|$ remains the same, makes $B_{max} = |B_0|$. Therefore, g_2 , g_4 and therefore their flux-surface averages on the axis remain zero, leading the geometrical factor G_b to a null value. In the 3D case, exploiting the symmetry in θ , the RHS of Eq. (2.132) and Eq. (2.133) on the magnetic axis can be written as

$$\mathbf{B} \times \nabla \Psi \cdot \nabla \rightarrow -\frac{B_\theta}{\sqrt{g}} \frac{\partial}{\partial \phi} + \frac{B_\phi}{\sqrt{g}} \frac{\partial}{\partial \theta} \quad (3.15)$$

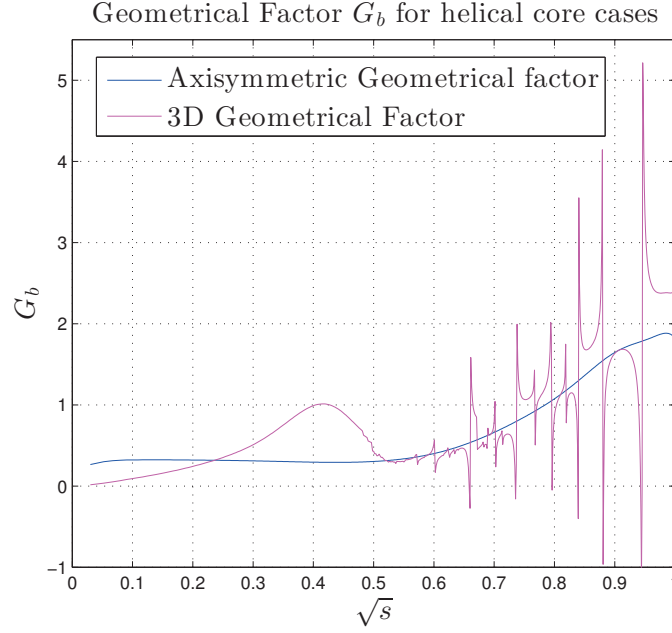


Figure 3.21 – The geometrical factor G_b for the *Shaing-Callen* model. The geometrical factor goes to zero on the magnetic axis, and it exhibits the resonances observed in the axisymmetric mantle.

where \sqrt{g} is the Jacobian, B_θ, B_ϕ are the covariant θ, ϕ components of the magnetic field. For helical symmetry, this expression is anti-symmetric along the field-line, and thus integrates to zero along the field-line, leading to the integral for g_2 , and consequently its flux-surface average $\langle g_2 \rangle = 0$. Assuming a small contribution from the second term of G_b , the geometrical factor G_b will be close to zero on the magnetic axis. Thus, the geometrical factor G_b for the *Shaing-Callen* model in the banana regime will always approach zero at the magnetic axis for a 1/1 saturated internal kink mode, giving a significantly different result from the *Sauter* model, seen in Fig. (3.22).

3.2.3 Summary of Bootstrap Current in 1/1 Helical Geometry

To summarise our conclusions about the bootstrap current in a strongly 3D equilibrium with a saturated 1/1 internal kink, we refer to Fig. (3.22), where it becomes evident that drastic drop in the *Sauter* bootstrap current density in between $s = 0$ and $s = 0.1$ follows the trapped fraction f_t profile, however the *Shaing-Callen* bootstrap current density follows the modulation offered by the geometrical factor more faithfully. Thus the 3D model provides a physical resolution that the axisymmetric model falls short of. We can thus conclude that, for a helical-core case which avoids resonant surfaces, it would be of interest to study the behaviour of the bootstrap current profiles in the case of a weak internal transport barrier. The difference amongst the *Sauter* and *Shaing-Callen* models, along with the possibility to choose non-resonant ι -profiles, make it a useful case in which the *Sauter* and *Shaing-Callen* models can show significantly

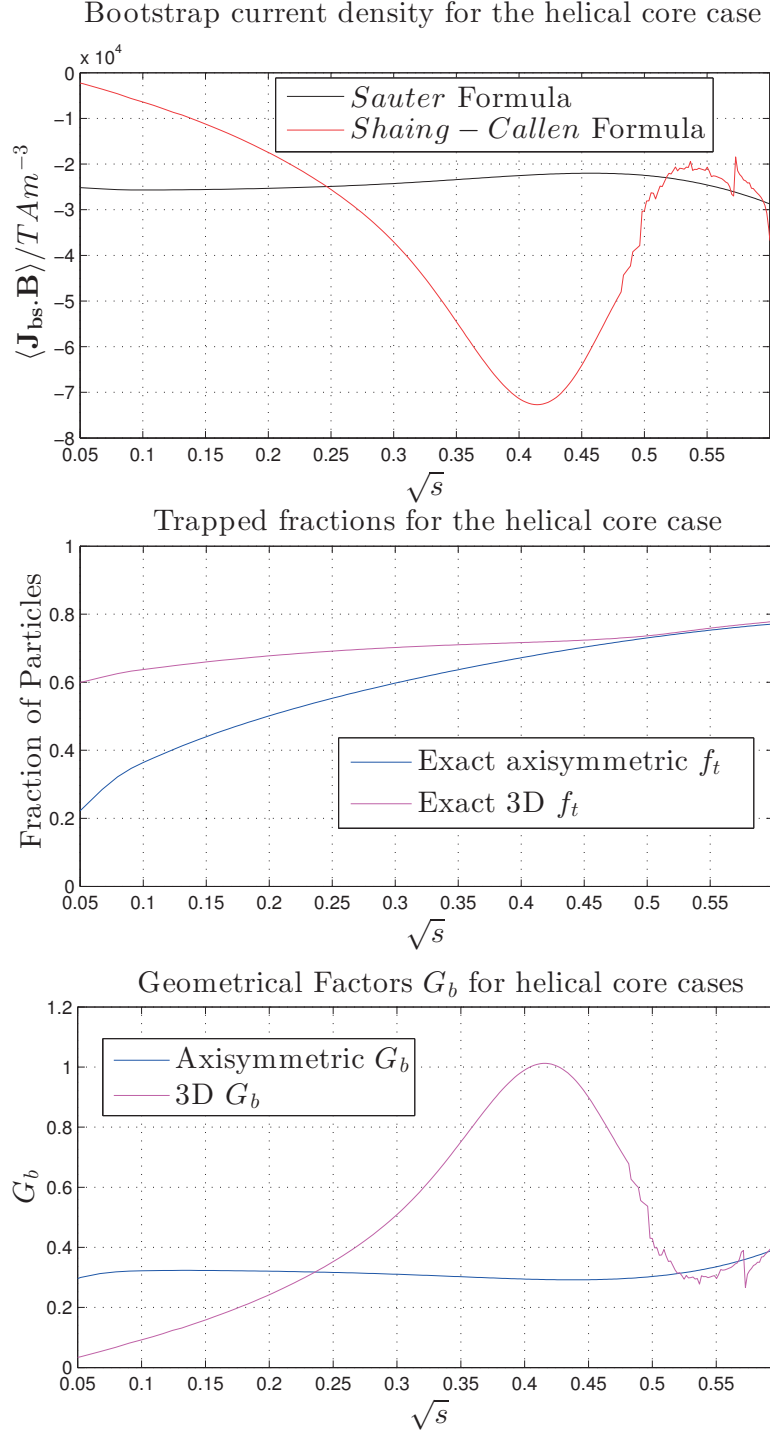


Figure 3.22 – A focus on the bootstrap current density in the helical core region. Also plotted are the trapped fractions and the geometrical factor in order to compare the variations of the *Sauter* and *Shaing–Callen* bootstrap current prescriptions against the causal factors.

different bootstrap current density profiles in the helical core region, a strong intrinsic 3D effect. Thus the 3D *Shaing-Callen* model, and the additional computational effort exerted, is significant for an accurate numerical analysis of the helical core case. This result will assume a central importance in the next chapter, where we examine the background ion parallel flow velocity in presence of a saturated 1/1 internal kink equilibrium.

3.3 Summary and Outlook

In the chapter, we have studied the bootstrap current in MAST-like equilibria with an iterative self-consistent procedure in which the total current and the Ohmic current profiles are kept fixed. The bootstrap current calculations were performed from a given VMEC equilibrium and merged into the toroidal current profile while keeping the total current constant. The procedure is iterated until convergence to a specified tolerance. The bootstrap current profile was evaluated using two known models: the *Sauter* and the *Shaing-Callen* models. We first began with a MAST equilibrium presenting a steep edge pressure pedestal as is observed in H-modes. For the axisymmetric test case considered, we observed a rapid convergence. Having being satisfied with the convergence and the self-consistency of the scheme in axisymmetry, we proceeded to examine 3D equilibrium for the edge pressure barrier with the two models. The 3D equilibrium was seen to present severe current sheets at q -rational flux-surfaces, prompting an investigation into methods to minimize these resonances. First, when applying resonance detuning, it was noticed that the resonance detuning parameter has a very narrow range of optimal values where the resonant q -rational surface currents are minimized without affecting the overall bootstrap current density. But the minimization of the parallel current was still not enough to extract any useful physics from this case. In order to investigate ways to externally minimize the q -rational resonances, we proceeded to reduce the toroidal field ripple by increasing the number of TF-coils. It was observed that toroidal ripple plays little effect beyond 12 toroidal-field coils, implying that the axisymmetric model performs as well as the 3D model, without the burden of parallel sheet currents that emerge on q -rational flux surfaces. In addition, sampling in the radial direction was increased in order to minimize the width of the resonant current spikes. However, it was seen that the increased sampling provides no significant improvement to the values of the resonances observed, leading to another negative result. In order to see whether some useful physical effects would still be salvageable from this particular 3D case, we further applied RMPs, varying the current in the RMP coils. At the edge, where bootstrap current is the maximum for the edge pressure barrier based equilibrium, virtually no change was observed. Therefore, the bootstrap current does not change significantly under equilibria with ideal response to RMPs. Furthermore, any possible effects that could have been observed in the mid-radius region are masked by severe current spikes, making such observations statistically weak. Therefore, very little physical insight could be derived for the 3D edge pressure barrier case.

Therefore, we chose to focus on the choice of a q -profile along with a strong 3D effect that prevents major resonances in the domain of interest. We generated through VMEC, a finely

Chapter 3. Effects of 3D on Bootstrap Current

tuned equilibrium with a saturated 1/1 internal kink helical core, by imposing a q -profile that avoids low order resonances in the helical core region. In the helical core region, we observed a significant difference between the *Sauter* and *Shaing-Callen* formulations. In particular, it was noticed that there is an augmentation in the bootstrap current density in the helical region of the 1/1 internal kink. We conclude that these differences occur on the account of the differences in the physical model, and that the 2D and 3D models do indeed present significantly distinguished results without resonance effects, making helical core studies an ideal candidate for bootstrap current research using the self-consistent iterative method.

4 Effect of 3D on Impurities

4.1 Introduction

In beam injected plasmas exhibiting strong toroidal flow, an important area of concern is the mitigation of confinement of heavy impurities. Unfortunately, beam injected experiments in JET and ASDEX upgrade, both with tungsten divertors, often exhibit rapid inward transport of tungsten impurities, leading to poor performance, and occasionally radiative collapse[Pütterich et al., 2010]. These poor plasma conditions can be mitigated by using auxiliary heating to peak the core temperature[Sertoli et al., 2015b] shielding inward impurity transport, verified via fluid-based neoclassical[Ahn et al., 2016] and turbulent gyrokinetic approaches[Casson et al., 2015]. Such techniques, however, have limited success during strong core MHD phenomena, such as neoclassical tearing modes (NTMs) and sawteeth[Sertoli et al., 2015a], where the parallel transport associated with resistive islands is probably important. In JET, it has been stated that $n = 2, m = 3$ NTMs are now intolerable due to the massive influx of impurities associated with long-living core islands[Hender et al., 2016]. Scenario development is concerned with avoiding core magnetic islands.

The presence of strong toroidal flow leads to a significant modification of the particle confinement in the plasma. Because of their low thermal velocity, tungsten particles possess supersonic flow and are strongly trapped even in plasmas where the bulk-ion flow is strongly subsonic. In the axisymmetric limit, it has been shown that the centrifugal trapping leads to a strong enhancement of diffusivity[Wong and Cheng, 1989, Fülöp and Helander, 1999]. One way to model the distribution of impurities is to follow the full 6D gyromotion of the impurity marker distribution (a so-called PIC approach) which is necessary when the electric and magnetic field variation is of the order of the gyroradius of the particle. When such scale-length variations (including time-varying fluctuations[Romanelli et al., 2011]) are not present and the fields are smooth to the scale of the gyroradius, one may follow the guiding-centre orbits, which greatly reduces the computational cost. Proper accounting of centrifugal and neoclassical effects leads to the well-known impurity flux distribution[Romanelli and Ottaviani, 1998] in axisymmetry, though little has been done so far using a PIC approach. Modelling attempts

using PIC methods in the past have reproduced the strong diffusivity without reproducing the impurity peaking seen in experiments [McKay et al., 2008, McClements and McKay, 2009, Romanelli et al., 2011] essentially because the neoclassical transport arising from collisions of the trapped impurity particles with the passing particles background ions was neglected. This is the first area addressed by this manuscript, in which we follow a guiding-centre based PIC approach with a neoclassical collision operator.

In addition to plasma rotation and neoclassical effects, the presence of MHD modes can also have a significant effect on the particle orbits. Here, and in contrast to previous works involving resistive saturated structures associated with NTMs and sawteeth, we concentrate on plasma scenarios with $q > 1$ in the presence of a continuous $m = 1, n = 1$ 3D ideal MHD mode. In MAST and JET hybrid scenario experiments, where the q -profile has an extended region of low magnetic shear near the axis and stays above unity, experiments can exhibit long-lived continuous $n = 1$ helical structures [Chapman et al., 2010, Chapman et al., 2014]. These continuous modes, accompanied by toroidal rotation of the plasma and the mode, are surmised to be manifestations of a saturated and stable 1/1 internal kink. While 1/1 ideal internal kinks (without magnetic islands), degrade the confinement of fast ions [Pfefferlé et al., 2014b], there is also increasing evidence of enhanced heavy impurity accumulation in the core region. We aim at a better understanding of the neoclassical impurity pinch (and other geometric effects) under such conditions in the plasma.

In order to compare impurity transport for kinked and unkinked magnetic fields with the neoclassical transport, turbulent transport is out of the scope of the thesis. We use the 3D ideal MHD equilibrium code VMEC to obtain our stationary 1/1 kinked magnetic fields [Hirshman and Whitson, 1983, Hirshman et al., 1986]. One of the features of VMEC, is that one may obtain bifurcated solutions for an equilibrium with a helically distorted axis [Cooper et al., 2010], which agrees with saturated initial value calculations of the internal kink mode [Brunetti et al., 2014]. This allows us to obtain accurate magnetic equilibria representing modes which are observed experimentally. Using the obtained equilibrium, one can use the guiding-center orbit-following PIC code VENUS-LEVIS [Pfefferlé et al., 2014a] to observe the behaviour of different kinds of particles facing different equilibrium scenarios [Pfefferlé et al., 2014b]. In addition, we have incorporated centrifugal and electric field effects in VENUS-LEVIS in the current work, allowing us to test particle behaviour under strong rotation. Furthermore, in order to develop an accurate model, it is of utmost importance to include neoclassical effects arising because of the collisions. We consider only the collisions between the impurity particles and the background ions [Helander and Sigmar, 2005, Shaing et al., 2015], and neglect impurity self-collisions. We therefore operate in the so-called trace limit. In order to account for the discontinuity in the distribution function at the trapped-passing boundary of the background ions, we calculate the background ion parallel velocity analytically using established neoclassical theory [Nakajima and Okamoto, 1992, Shaing et al., 2015]. The analytic computation of the parallel background velocity of the ions in axisymmetry is fairly simple. For cases in which a strong 3D deformation is present, we invert the continuity equation for computing the parallel flow velocity of the background ions. These calculations enable us, for the first

time, to compute tungsten accumulation in realistic rotating hybrid plasma scenarios with continuous modes using a PIC approach.

This chapter is organized as follows. In Section 4.2, we describe the complete implementation of the flows and neoclassical effects. As the collision operator responsible for the friction force requires an accurate description of the flows of the plasma background, we proceed to describe that in Section 4.3. Then, we simulate the heavy impurity cases with VENUS-LEVIS for axisymmetry and helical core equilibria generated from VMEC in Section 4.4. In the end, we summarize our conclusions and future direction of work in Section 4.5.

4.2 Impurity Trajectories with Collisions

The standard guiding-center orbits of the impurity particles are chiefly modified by two additional factors, i.e. plasma flow and collisions. Therefore, in this section, we aim to describe the implementation of the classical orbit effects and the neoclassical collisional effects.

The problem of obtaining heavy impurity dynamics in the trace limit involves the solution of the full distribution F_W for the impurity ions evolving over time to a steady-state. In the PIC approach, this involves the sampling of particles from the impurity distribution, evolving their trajectories with time, and accounting the interaction of the impurity particles with the background through collisions. The background flow plays two major roles in the behaviour of heavy impurities. Firstly, the centrifugal force arising from the potential gradients is felt significantly by the impurity ions because of their relatively high mass and ionization state. Secondly, since the impurities and the background ions move with different flows, this will result in a drag force on the impurity distribution F_W by the background ion distribution F_i .

4.2.1 Centrifugal Effects

We consider here the centrifugal effects. We know, from Sec. 2.3, the total flow of the species j , \mathbf{U}_j , with the parallel and perpendicular components being $\mathbf{U}_{\parallel,j}$ and $\mathbf{U}_{\perp,j}$ respectively, further divided into the leading-order and higher-order flows $\mathbf{U}_j = \mathbf{U}_{0,j} + \mathbf{U}_{1,j}$. Imposition of a toroidal leading-order flow leads to simplifications in the computation of the associated centrifugal and Coriolis terms in the guiding-center formulation, and in the computation of the higher-order quasi-neutrality-preserving Φ_1 , which leads to an associated $\mathbf{E}_1 \times \mathbf{B}$ flow. The leading-order flow is the same for every species, and the centrifugal and Coriolis forces arising from the lowest-order flow are imposed on heavy impurity species through the guiding-center equations. As derived in Section 2.5, the guiding-center equations of motion are given by

Chapter 4. Effect of 3D on Impurities

Eqs. (2.80),

$$\begin{aligned}\dot{\rho}_{\parallel,j} &= \frac{\mathbf{E}^* \cdot \mathbf{B}^*}{\mathbf{B} \cdot \mathbf{B}^*} \\ \dot{\mathbf{X}}_j &= \left(U_{0\parallel,j} + \frac{Z_j e}{m_j} \rho_{\parallel,j} B \right) \frac{\mathbf{B} \mathbf{B}^*}{\mathbf{B} \cdot \mathbf{B}^*} + \frac{\mathbf{E}^* \times \mathbf{B}}{\mathbf{B} \cdot \mathbf{B}^*},\end{aligned}\tag{4.1}$$

or in the alternate form in Eqs. (2.113)-(2.114) as seen in Chapter 2,

$$\begin{aligned}\dot{\rho}_{\parallel,j} &= \frac{\mathbf{B}^*}{\mathbf{B} \cdot \mathbf{B}^*} \cdot \left\{ \nabla \Phi_1 + \frac{\mu_j}{Z_j e} \nabla B + \frac{m_j}{Z_j e} \mathbf{U}_{0,j}^* \cdot \nabla \mathbf{U}_{0,j}^* \right\} \\ \dot{\mathbf{X}}_j &= \mathbf{U}_{0,j}^* + \frac{\mathbf{B}}{\mathbf{B} \cdot \mathbf{B}^*} \times \left\{ \nabla \Phi_1 + \frac{\mu_j}{Z_j e} \nabla B + \frac{m_j}{Z_j e} \mathbf{U}_{0,j}^* \cdot \nabla \mathbf{U}_{0,j}^* \right\}.\end{aligned}$$

The leading-order flow is imposed to be purely toroidal

$$\mathbf{U}_0 = U_{\phi 0,j} \nabla \phi = \Omega(\psi) R^2 \nabla \phi,\tag{4.2}$$

where $\Omega(\psi)$ is the angular velocity, for the simplicity of expressions of gradients of the flow in Eq. (2.80) much simpler as elaborated in Sec. 2.5.1. Again, It is important to note that the leading-order flow in its most general form is not purely toroidal, but actually lies along the intersection of the contours of ψ and B [Helander, 2014]. The extension of the work to incorporate a more complete description for the flow is in progress. Next, the quasi-neutrality restoring potential is

$$\Phi_1 = \frac{T_e}{T_i + T_e} \frac{m_i}{2e} \Omega^2 R^2.\tag{4.3}$$

We again mention that we impose the axisymmetric form of Φ_1 for the simulations with 3D fields as well. Additionally, in inductively-driven plasmas, there is also a loop voltage V_{loop} induced electric field $E_{\parallel,loop}$. The parallel electric field is responsible for driving the plasma current results in an inward pinch of particles, known as the Ware pinch [Ware, 1970]. It leads to a usually very small inward velocity for the heavy impurities, which has been established to not play a significant role in heavy impurity confinement in the presence of strong plasma rotation [McClements and McKay, 2009]. With high temperatures and low loop-voltages in JET and high $\mathcal{M}_{0,W}^2$ flows for tungsten particles, this pinch will not be a significant effect to consider. This parallel electric field is very low (V_{loop} is of the order of 0.1V) for a JET pulse during the NBI-driven phase of the pulse and does not play a significant role when strong rotation is involved.

4.2.2 Neoclassical Effects

The neoclassical effects arise from the fact that the flow velocities for the background ion species and the heavy impurity species is different, therefore leading to a drag on the impurities by the background ions. Additionally, the neoclassical effects are modified in the presence of strong leading-order flow $\mathbf{U}_{0,i}$, which causes the heavy impurities to be confined in heavily trapped orbits with strong poloidal asymmetry, which leads to a magnification of the neoclassical diffusion [Wong and Cheng, 1987, Angioni and Helander, 2014]. The forces responsible for such strongly trapped particle orbits are provided by guiding-center equations described in the previous section [Wong and Cheng, 1989]. The neoclassical effects, however, come into action through collisions. The drag affects all impurities except those flowing with the same flow velocity $\mathbf{U}_{0,i}$ as the main ions.

To account for the parallel friction, we must take into account the pressure-gradient derived higher-order flow $\mathbf{U}_{1,j}$, which is different for each species and requires the solution of the continuity equation for each species. In the trace impurity limit, the higher-order flow for impurities $\mathbf{U}_{1,j}$ will arise when the impurity particle finite Larmor-radius effects are statistically averaged over. Therefore, we only need the background ion flow $\mathbf{U}_{1,j}$ description to correctly account for the flow differences. Once the higher-order flow $\mathbf{U}_{1,i}$ is computed, it must also be implemented in the collision operator in order to obtain the corresponding neoclassical effects. Thus, the particle velocity has to be provided to the collision operator such that it is in the frame of the background flow $\mathbf{U}_{0,i} + \mathbf{U}_{1,i}$. To illustrate this, in Fig. 4.1, the distribution F_i represents the background distribution with which the heavy impurities collide and the distribution F_W represents the distribution from which the heavy impurity particles are sampled for the PIC simulations. We can notice that the distributions are displaced by their respective flow velocities, and the difference in flows leads to a drag by the background species on the heavy impurity species. We would ideally like to stay in the rest frame in order to make the orbit-following simpler.

However, the Monte-Carlo collision operator assumes that the background distribution with which the collisions are simulated is at rest. There is a simple work-around to solve this issue, however. The Monte-Carlo collision operator in VENUS-LEVIS takes as inputs the kinetic energy E and pitch λ and supplies new values of these parameters E', λ' after the collision. Collisions are performed at intervals smaller than the inverse of the collision frequency or at each time-step, whichever is larger, in order to reduce computational bottlenecks. Before providing the collision operator with the values of E, λ , we transform these parameters into the flow frame of the background ions, which involves providing values E_{rest}, λ_{rest} , modified by the shift by the velocity $\mathbf{U}_{1,i}$, as seen in Fig. 4.2. In this frame, the background ion distribution is at rest. Since the flows arising from the potential gradients ($U_{0,i}$ and quasi-neutrality dependent higher-order flow) are same for all species, they cancel out and are not needed for the frame-shift. After the collision operator performs the collision, we receive as output the new energy and pitch in the moving frame $E'_{rest}, \lambda'_{rest}$. These values are now transformed back into the rest frame E', λ' by performing a velocity shift of $-\mathbf{U}_{1,i}$. This effectively implies

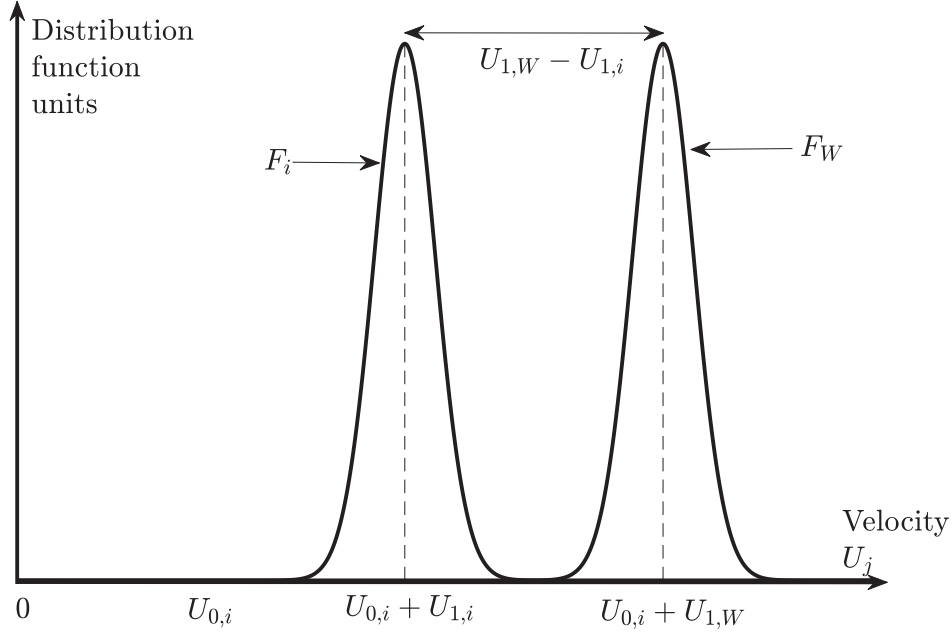


Figure 4.1 – The distributions in the rest frame.

that the collision operator takes into account the difference between the particle velocity and the background ion velocity, thus providing the relevant classical and neoclassical friction forces. However, since the impurity particles are individually sampled from a distribution, the drag on each individual impurity particle cannot be observed, but can be statistically averaged and observed over the entire distribution. With this procedure, the neoclassical effects are implemented and will be used for simulations in the next sections.

One subtlety to note, is that the impurity distribution F'_W has been shifted by the leading-order flow. Thus, the initial sampling of the particles must now take into account the flow velocity in order to produce the initial distribution in the rest frame. Then, the application of the centrifugal force by the guiding-center forces will ensure that the particle remains flowing with the leading-order flow.

4.3 Neoclassical properties of Axisymmetric and Helical-core Equilibria

The ideal MHD equilibria, both axisymmetric and those possessing a saturated 1/1 internal kink, are generated for a JET-like case with the Variational Moments Equilibrium Code (VMEC)[Hirshman and Whitson, 1983, Hirshman et al., 1986]. VMEC generates equilibria using the steepest descent method minimizing the ideal MHD energy functional:

$$\mu_0 W = \int \int \int d^3x \left(\frac{B^2}{2} + \frac{\mu_0 p(s)}{\Gamma - 1} \right). \quad (4.4)$$

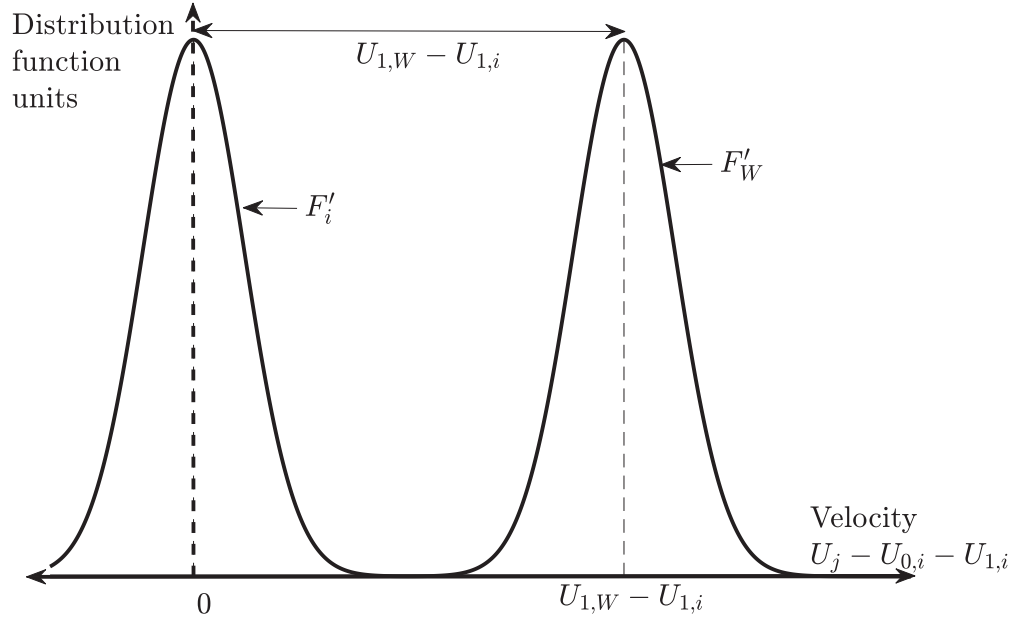


Figure 4.2 – The distributions in the frame moving with the background ions.

For axisymmetry, the minimization of Eq. 4.4 is functionally equivalent to arriving at an equilibrium by solving the Grad-Shafranov equation under the appropriate boundary conditions. For obtaining a 3D saturated 1/1 internal kink, one specifies a skewed axis with an appropriate q -profile that can effectively converge upon a saturated helical core. The flow is imposed later in the guiding-centre equations to study particle behaviour. The helical core equilibrium with $q_{min} \gtrsim 1$ has been shown to correspond to the stable 1/1 internal kink mode in hybrid scenarios [Brunetti et al., 2014]. The reason for ignoring the rotation in calculation of the equilibrium fields is that currently there is no consistent MHD model for rotation in 3D plasmas. In the limit where the bulk ions are strongly subsonic, inertial effects due to the centrifugal force are negligible, and as such we may assume that the plasma rotates toroidally in a 3D kinked plasma just as it does to leading order for an axisymmetric plasma. Indeed the Mach number for bulk ions is such that the bulk flow is strongly subsonic, and hence any empirically observed MHD non-axisymmetry would move past magnetic probes with an associated frequency $n\Omega$, where n is the toroidal mode number, and Ω is the toroidal plasma rotation frequency. The dominant MHD mode in the current work is a saturated $n = 1, m = 1$ continuous mode.

We proceed to generate the required magnetic equilibria. We choose appropriate pressure and q -profiles for the equilibria as seen in Fig. 4.3, and create a helical core equilibrium by initially prescribing an appropriate helical displacement of the magnetic axis ($\sim 0.2m$ helical skew in the radial direction). On constraining the number of toroidal modes to zero, we obtain an axisymmetric bifurcated solution. The comparison of the axisymmetric and helical core sister states can be seen in Fig. 4.4. The equilibria are low current hybrid scenario equilibria,

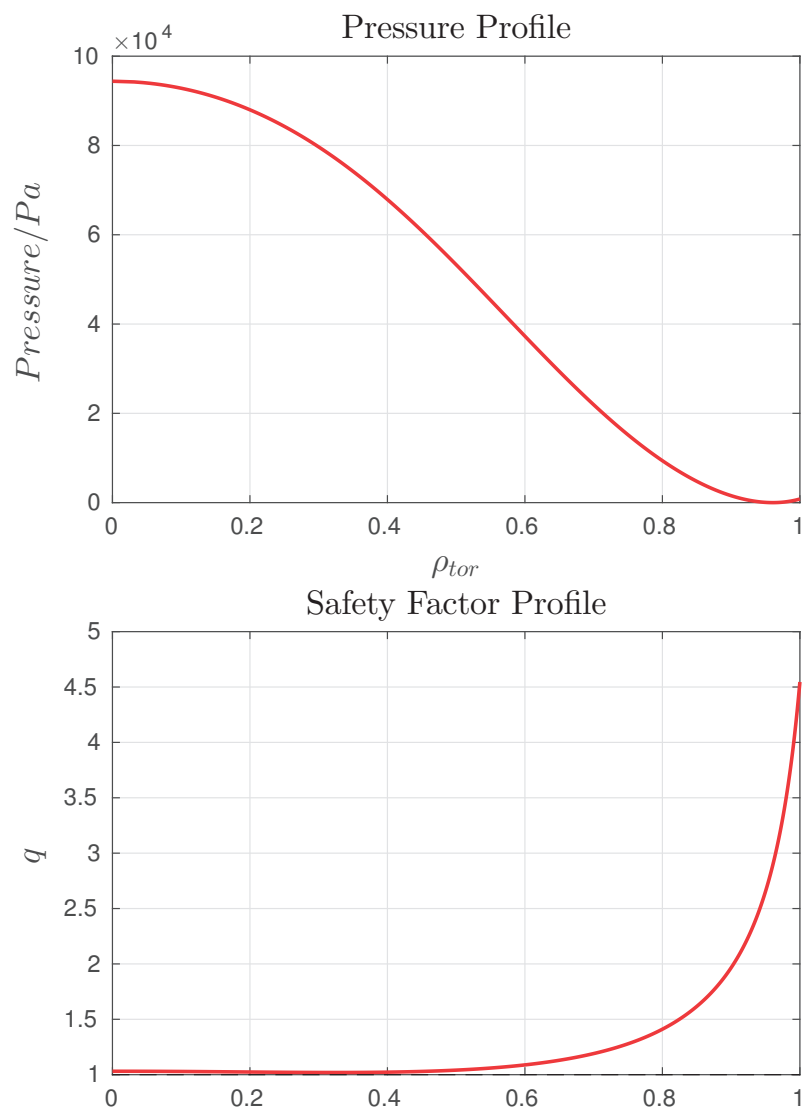


Figure 4.3 – The selected profiles used for generating the helical and axisymmetric branches of the VMEC equilibria.

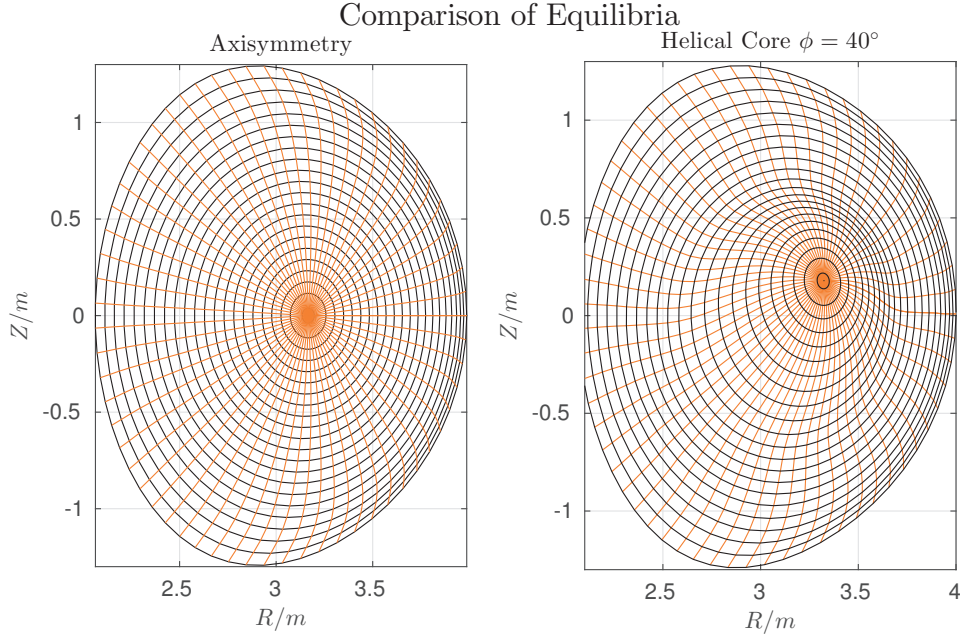


Figure 4.4 – Toroidal cuts of the VMEC equilibria for a helical core and its axisymmetric sister state. Notice how the constant pressure surfaces are shifted by the saturated internal kink.

with a normalized beta value of $\beta_N = 3.1\%$, as seen in Tab. 4.1. We use these equilibria as the basis for our electric and magnetic fields in the guiding-centre orbits.

We use the equilibrium to compute the parallel velocity $U_{1\parallel,i}$ for the background equilibria. It is fairly difficult to invert the continuity equation assuming VMEC-coordinates. Conversion to straight-field line coordinate system such as Boozer coordinates[Boozer, 1981] makes the calculation for the parallel velocity much easier. This is accomplished using TERPSICHORE[Anderson et al., 1990], a code package that also allows for a convenient mode selection so as to ensure a precise conversion of the VMEC mode spectrum into the Boozer mode spectrum. Furthermore, after having converted the magnetic equilibrium into Boozer coordinates, we integrate equation 2.132 by transforming into Fourier-space of the Boozer spectrum, where the gradients are represented as simple scalars in the direction of the magnetic field. However, this leads to the problem of numerical resonances at rational q -surfaces[Cooper et al., 2004]. These spikes occur due to the parallel gradient operator $\mathbf{B} \cdot \nabla$ being proportional to $(m\Psi' - n\Phi')^{-1}$, which is singular at rational $q = m/n$ surfaces in Fourier space. The mitigation of these numerical resonances is performed by inclusion of a resonance detuning operator Δ_{mn} , which numerically smooths over the singularities, as described in Sec. 2.7.4. Crucially, quantities in the helically-deformed region are unaffected by the value of Δ . As will be seen, the 1/1 non-resonant internal kink mode is a particularly interesting application because the core 3D structure avoids resonance, hence is independent of the details of the resonance detuning parameter, and largely the physics of resistivity, should it

Toroidal Current I_p	1.79MA
On axis pressure P_0	$1.0 \times 10^5 \text{Pa}$
On axis temperature T_0	2.1keV
Safety factors q_0, q_{95}	1.053, 4.683
Edge toroidal flux Φ_{edge}	8.27Wb
On axis field B_0	2.88T
Major and minor radii R_0, a	3.238m, 1.14m
Helical skew δ_h	0.23
Beta values β, β_N	2.56%, 3.16%
Grid Sizes (n_s, n_θ, n_ϕ)	(231, 45, 25)
Mode numbers (m, n)	(9, 5)

Table 4.1 – Values of essential parameters used in the equilibrium generation for a JET-like case

have been included.

As explained in the previous section, it is of interest to compute the surface-averaged parallel velocity, $\langle U_{1\parallel, i} \rangle$ for axisymmetric and helical cores in the Pfirsch-Schlüter regime. This gives us an insight into how the helical distortion modifies the parallel velocities, $\langle U_{1\parallel, i} \rangle$, as shown in Fig. 4.5. It is worth noting that, for the 3D equilibrium, this leads to a finite poloidal flow, as seen in Fig. 4.6, whereas it is zero for the axisymmetric case in the Pfirsch-Schlüter regime as is well-known neoclassical literature in the limit of zero temperature gradients [Helander and Sigmar, 2005, Shaing et al., 2015]. This will become important to interpret the simulation results, as will be seen.

We notice immediately that, for the 3D case, the parallel velocity $\langle U_{1\parallel, i} \rangle$ is strongly augmented in the helical core region, as compared to axisymmetry, as observed in the previous work of the authors in Ref. [Raghunathan et al., 2016]. This increase in the helical core region is due to the parallel gradient operator being very small in the core ($(m\Psi' - n\Psi')^{-1}$ being large) due to the near resonance of the 1/1 mode. The low value of $(m\Psi' - n\Psi')$ consequently causes the magnification of the geometrical factor in the helical core region. Similar enhancements to the bootstrap current due to the helical core have been reported earlier [Raghunathan et al., 2016] and in Chapter 3 in the current thesis. The enhanced parallel velocity $U_{1\parallel, i}$ is accompanied by the presence of a finite poloidal flow for the 3D case, whose importance will be explained later.

4.4 Simulations of Tungsten Neoclassical Transport

In this section, we perform full- f simulations of tungsten species in the trace limit interacting with the background plasma through collisions. The particle trajectories are evolved by the guiding-centre formulation and the collisions with the background plasma are made by the Monte-Carlo collision operator described in the preceding section. The background fields are used from the VMEC equilibria as also described earlier. The full distribution is initialized

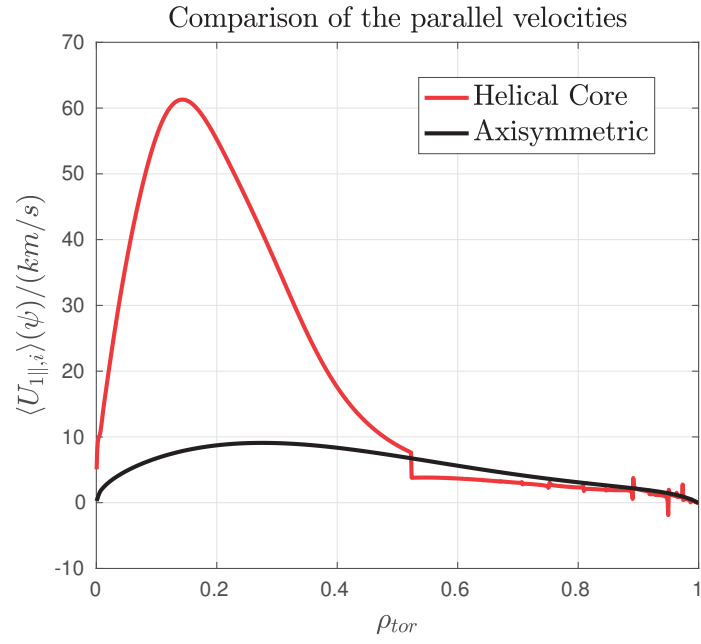


Figure 4.5 – The computed values of the parallel velocity $U_{1||,i}$.

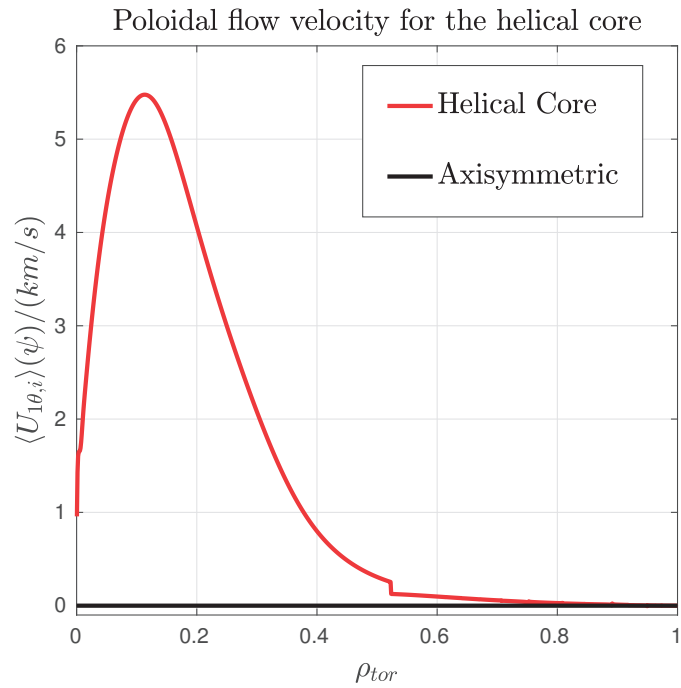


Figure 4.6 – The associated value of the poloidal flow velocity $U_{1\theta,i}$ for the helical core.

in terms of markers weighted appropriately to emulate the chosen initial distribution. The evolution of the distribution and the marker weights provides us the evolution of the distribution in time. For all our guiding-centre simulations, we choose a toroidal angular velocity $\Omega = 1.2 \times 10^5 \text{ rad/s}$ (corresponding roughly to 20kHz and Mach number $\mathcal{M}_{0,W} = 8.94$) for the toroidal ensemble flow. We initialize a full distribution of heavy tungsten impurity with an effective charge of $Z_W = 40$ and an initial Maxwellian density of the form $n_W = n_i \times 10^{-4}$, such that the impurity contributions to the plasma and the fields can be neglected. We initialize 2^{15} markers weighted appropriately to emulate the full distribution and let the particles evolve their orbits until the density profile saturates. It is necessary to resolve very finely in time because of the large angular rotation speed, and we find in the performed simulations that the final impurity density profiles converge to the precision of 10^{-7} with 2^{15} particles on 2^{10} cores. Hence this choice of the number of the particles leads to adequate precision while optimizing the overall computation time.

The initial normalised pressure and temperature profiles are chosen to be the same as those of the background ions and electrons used for the VMEC equilibria as in Fig. 4.3. We assume a flat background ion and electron temperature profiles with $T_{0,i} = 2.1 \text{ keV}$, in order to choose the most pessimistic case of inward impurity pinch without the potentially beneficial screening provided by the thermal gradient.

4.4.1 Benchmark for a Non-Rotating Axisymmetric Equilibrium

We first start with a benchmark to test whether the model has been implemented properly. In order to do so, we choose an axisymmetric equilibrium, initialise the particles as explained previously, and let the orbits evolve in the absence of flow, and let the density profile evolve to saturation. We notice that the density profiles take about $t \approx 2 \text{ s}$ to evolve to saturation. During the progression of the simulation, we see from Fig. 4.7, that the particles are drifting inwards with time, leading to density saturation at around $t = 2 \text{ s}$. Additionally, the inward drift speed can be heuristically estimated to be in the order of 1 m/s , which agrees with benchmarked values from studies performed previously [Ahn et al., 2016]. Fig. 4.9 further shows that the density of the tungsten impurities over R and Z strongly peaks near the axis.

Having performed the simulation under the simplest conditions of axisymmetry without flows, we would now like to confirm it with known results from the theory of impurity transport. From the neoclassical theory of impurities without flow for axisymmetric conditions, we would expect the saturated density profile to be as in Eq. (2.164) [Helander and Sigmar, 2005]

$$\frac{\langle n_W(r) \rangle}{\langle n_W(r=0) \rangle} = \left(\frac{n_i(r)}{n_i(r=0)} \right)^{Z_W/Z_i},$$

i.e. a very peaked density indicating that the particles have to undergo a significant inward drift leading to peaking on the axis, which is exactly what we observe in our simulations. On comparing the numerically obtained density with the peaked profile predicted by Eq. (2.164),

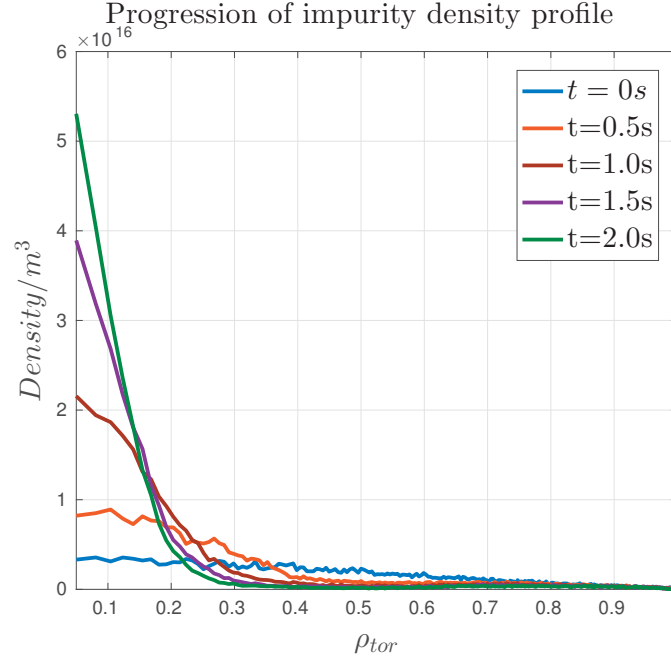


Figure 4.7 – The density profile of the impurity with time for an axisymmetric JET-like equilibrium without rotation. Notice the slow but constant inward drift of the density, leading to heavy impurity peaking on the axis.

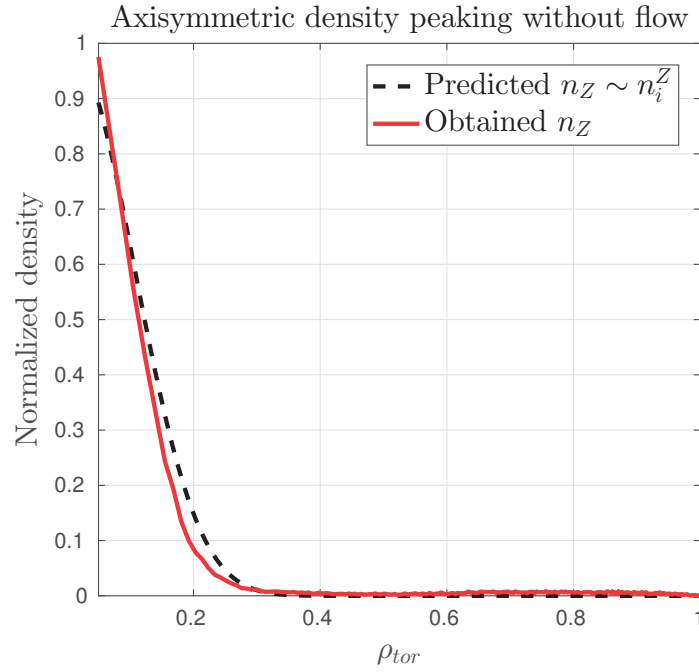


Figure 4.8 – Plot of the predicted and numerically obtained impurity density for an axisymmetric equilibrium without flow. The black dashed curve represents the one plotted from Eq. (2.164). We find that they are in good agreement.

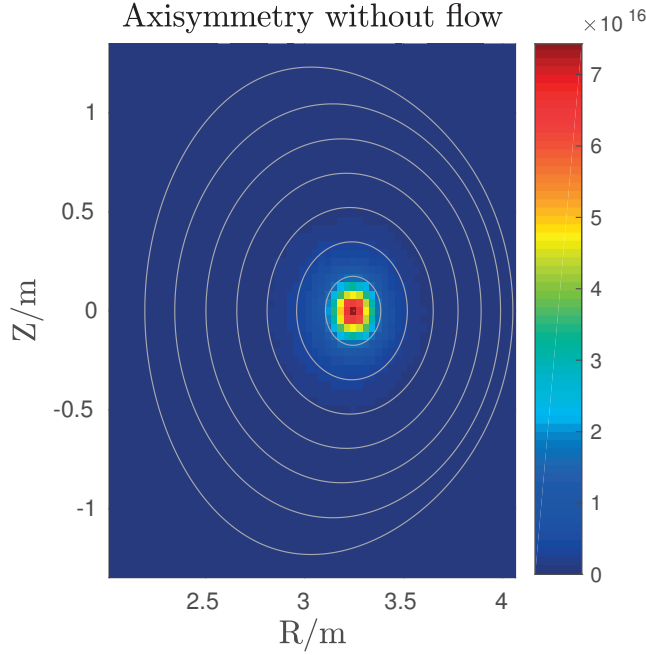


Figure 4.9 – Density plot for the axisymmetric equilibrium without flow at $t = 2s$. As we expect, the tungsten impurities concentrate on the axis with the density following the predicted density.

we can observe from Fig. 4.8 that the final normalized density profile agrees reasonably well with the predicted normalized density.

4.4.2 Benchmark for Axisymmetry with Plasma Rotation

We now perform a full- f simulation with $20kHz$ flow for axisymmetry and we find that the particles do not make it all the way into the core region, but saturate at the edge of the core region, which can be seen in Fig. 4.10. For the JET cases examined here, the effective Mach number is $\mathcal{M}_*^2 \approx 80$. Also, from the plot of the density on the toroidal plane, in Fig. 4.11, we notice that the particles are deeply trapped centrifugally, as expected, and settle off-axis. The time for the impurity density profile to saturate is reduced to the order of $t \sim 30ms$ from the $t \sim 2s$ value for the case of axisymmetry without flow.

Furthermore, if we impose a $20kHz$ flow and remove neoclassical effects by assuming that the flow velocity of heavy impurities in the flow-frame of the background ions is zero, i.e. the two species are flowing together therefore removing any frictional effects, we find a strong outward drift accompanied by a quick loss of particles, with the particle numbers depleting to zero in a very short time. If we define the impurity confinement time as the time it takes for the density to drop to $1/e$ its initial value, the confinement time is of the order of $40ms$, which agrees with the PIC simulations in Ref. [McClements and McKay, 2009, Romanelli et al., 2011], which were also performed without the inclusion of the neoclassical effects through collisions.

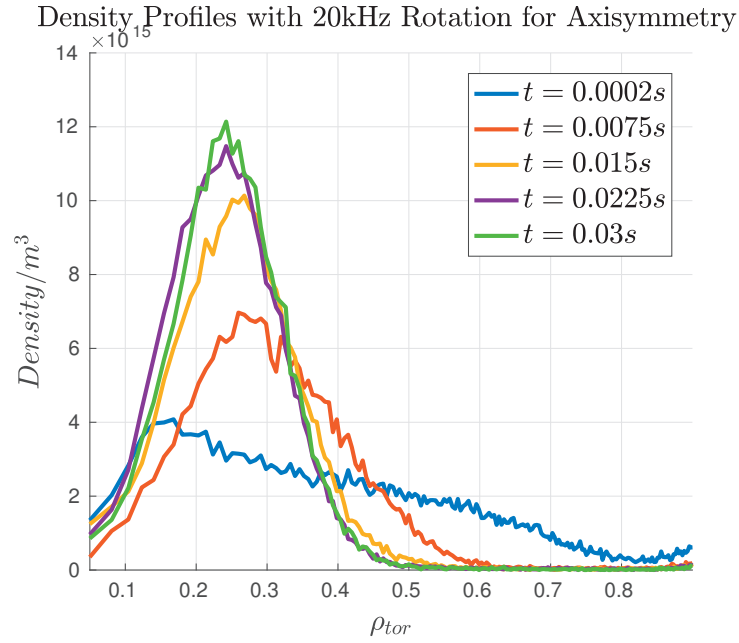


Figure 4.10 – The time progression of the density profile for an axisymmetric equilibrium case with 20kHz rotation.

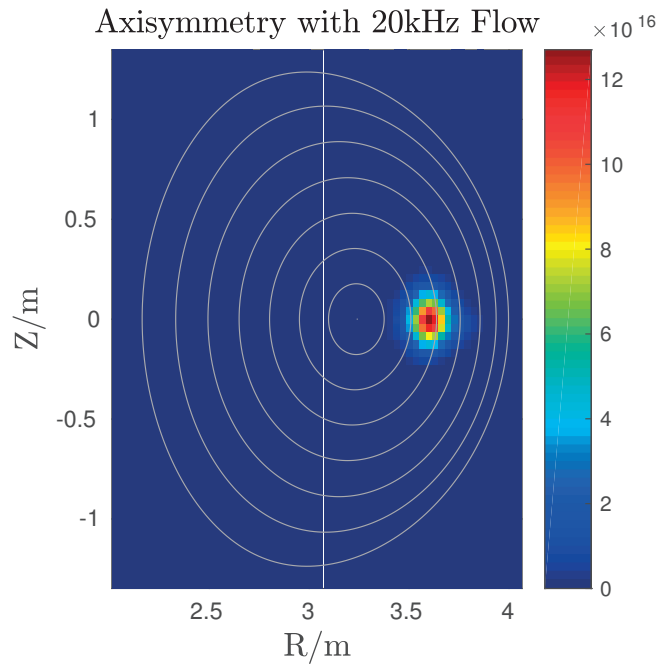


Figure 4.11 – Plots of density of tungsten for the axisymmetric equilibrium with 20kHz rotation. We notice that the impurities, deeply trapped on the low field side, saturate off-axis

Chapter 4. Effect of 3D on Impurities

These two results can be understood by recalling Eq. (2.161) for the radially averaged impurity fluxes [Romanelli and Ottaviani, 1998, Romanelli, 1998]. By assuming that the impurities have a strong poloidal asymmetry caused by the presence of the centrifugal force and the corrections for quasi-neutrality, the equations for parallel momentum balance and ambipolarity can be solved to obtain the following flux-surface averaged radial impurity flux $\langle \Gamma_W \cdot \nabla r \rangle$ as shown earlier in Eq. (2.161)

$$\begin{aligned} \langle \Gamma_W \cdot \nabla r \rangle_\psi = & -D_{PS}(1 + \mathcal{M}_*^2)^2 \langle n_W \rangle \times \left\{ \partial_r \ln \langle n_W \rangle - \left(1 - \frac{\mathcal{M}_*^2}{1 + \mathcal{M}_*^2} \frac{Z_i e n_i}{p'} \langle U_{1,i\theta} \rangle \right) \frac{Z_W}{Z_i} \partial_r \ln p_i \right. \\ & \left. - \frac{\tilde{m}}{m_*} \left(\frac{\mathcal{M}_*^2(1 + 3\epsilon \mathcal{M}_*^2 + 2\epsilon \mathcal{M}_*^4) - R_0 \partial_r \epsilon \mathcal{M}_*^2}{R_0 \epsilon (1 + \mathcal{M}_*^2)^2} \right) \right\}, \end{aligned}$$

and where $\epsilon = r/R_0$ is the inverse aspect-ratio, $D_{PS} = 2\epsilon^2(T_i/Z_W e B_{\theta 0})^2$ is the stationary Pfirsch-Schlüter diffusion coefficient, and the angle brackets $\langle \rangle$ indicate surface-averaged quantities. $\langle U_{1,i\theta} \rangle$ is the surface-averaged poloidal component of $\mathbf{U}_{1,i}$, as seen in Sec. 2.8.1. To understand Eq. (2.161), the physical contributions can be broken down term-by-term. The overall coefficient $D_{PS}(1 + \mathcal{M}_*^2)^2$ implies that the convective and diffusive processes are enhanced by the centrifugal effects by a factor of the Mach number squared. This plasma rotation dependent enhancement of the impurity flux could be simplistically understood in relation to the deep centrifugal trapping experienced by the heavy impurity particles. As trapped particles spend most of their time on their bounce-tips, the random walk step size is increased from their gyroradius to distance between their bounce tips, thus contributing to the increased diffusivity (as noticed later in the saturation times of the two cases with plasma flow.) In the fluid calculations, this can be reconciled by having impurity densities which are strongly dependent on the poloidal angle which can later be averaged out to obtain the radial impurity fluxes. The first term in the curly brackets proportional to $\partial_r \ln \langle n_W \rangle$, implies an outward flux contribution from the impurity density gradient, which remains small in the trace limit. The second term, proportional to $\partial_r \ln p_i$ is responsible for the inward flux of the particle, and is enhanced by presence of poloidal flow along with the toroidal flow. The averaged poloidal velocity remains exactly zero in axisymmetry with no temperature gradients in the Pfirsch-Schlüter regime, as seen in Fig. 4.6, and hence does not effectively amplify the peaking in the axisymmetric limit. The third term consisting of an expression in terms of the effective Mach number \mathcal{M}_* , provides an outward flux as a result of centrifugal effects.

The steady state of impurities is reached when the net flux of impurities vanishes, that is $\langle \Gamma_W \cdot \nabla r \rangle = 0$. On setting the RHS of Eq. (2.161) to zero, in the large aspect ratio limit with an unsheared \mathcal{M}_*^2 , with $\langle U_{1\theta,i} \rangle = 0$ for axisymmetry, we arrive at a steady-state impurity density profile for unsheared flows as follows

$$\frac{\langle n_W(r) \rangle}{\langle n_W(0) \rangle} = \left(\frac{n_i(r)}{n_i(0)} \right)^{Z_W/Z_i} \times \exp \left\{ \frac{\tilde{m}}{m_*} \frac{(3 + 2\mathcal{M}_*^2)\mathcal{M}_*^4}{(1 + \mathcal{M}_*^2)^2} \frac{r}{R_0} \right\}. \quad (4.5)$$

It can be immediately seen that the density profile with flow does not peak on the axis, but

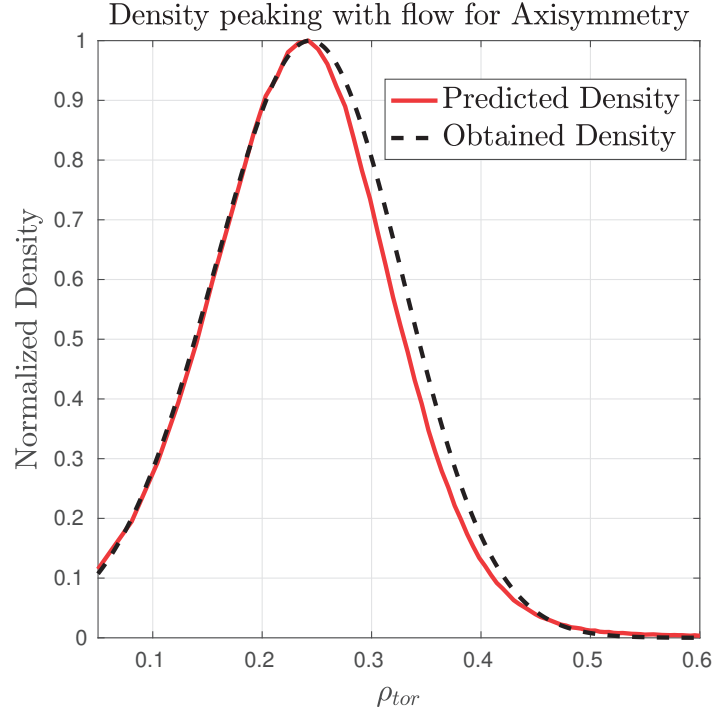


Figure 4.12 – Plot of the predicted and numerically obtained impurity density for an axisymmetric equilibrium with 20kHz plasma flow. The dashed black curve represents the saturated state obtained from Eq. (4.5). We find that they are in reasonable agreement, with the off-axis peaking reasonably predicted well.

is modulated by a flow-dependent exponential term moving the saturated density profile off-axis. We also recover Eq. 2.164 from the above expression by setting the Mach number $\mathcal{M}_* = 0$.

Ultimately, the observed spatial distribution of the impurities in Fig. 4.11 results because of the competition between the inward pinch offered by the neoclassical effects and the outward drift because of the centrifugal effects in Eq. 2.161. In the expression for steady-state density, Eq. 4.5, we see that the centrifugal effects add an exponential term that competes against the density peaking and can lead to off-axis peaking. This is also consistent with our numerical calculation of the parallel velocity $U_{1\parallel,i}$, since outward centrifugal advection starts competing with the inward pinch when the parallel velocity of the background ions is low, and hence the impurities do not feel a strong inward pinch in the low q -shear core region. Using Eq. 4.5, we evaluate the local maximum of the density distribution, by setting the derivative to zero. We find the local maximum occurs at $r/a \approx 0.23$, which agrees reasonably with the maximum of the density in Fig. 4.10. We also notice a reasonable agreement between the predicted surface-averaged density from Eq. 4.5 (setting $\mathcal{M}_*^2 \approx 80$) and our numerically obtained saturated surface-averaged density, which can be seen in Fig. 4.12. Furthermore, in absence of the friction term in Eq. (2.161), the only remaining term is the centrifugal outward diffusion,

further amplified by the $(1 + \mathcal{M}_*^2)^2$ factor. This would lead to a strong outward impurity diffusion, evidently increasing the standard non-rotating neoclassical diffusion of impurities by a factor of \mathcal{M}_*^4 , i.e. by a factor of ~ 1600 as employed in the simulations in this chapter. This also explains the quick particle loss observed for strong rotation without accounting for friction in previous literature [McClements and McKay, 2009, Romanelli et al., 2011].

4.4.3 Simulations for 1/1 Saturated Internal Kink with Rotation

In the previous subsection we saw that with strong rotation the impurities do not peak on the magnetic axis if the plasma is axisymmetric, even when there is no temperature screening. However, experiments often show strong peaking on the axis even in the presence of strong flows [Casson et al., 2015]. This section investigates the possibility of axial neoclassical peaking due to 3D effects in the core despite the presence of centrifugal effects.

For our simulations, we use the parallel flow velocity in the Pfirsch-Schlüter regime as obtained in the previous section for the helical core equilibrium. The surface-averaged parallel velocity profile $\langle U_{\parallel,i} \rangle$, as seen in the Fig. 4.5, is significantly different from that for the axisymmetric equilibrium. In particular, there is a significantly higher parallel flow for the background ions in the helical core than for the axisymmetric core. Therefore, we expect a different value of the neoclassical inward pinch for the impurity species for the helical core. We proceed to perform a full- f simulation for the helical core equilibrium rotating at 20kHz including neoclassical effects. We see, in Fig. 4.13, that the particles have made their way into the core very near the magnetic axis, and we notice saturation around $t \approx 0.015s$. Furthermore looking into the density distribution over various toroidal cuts, in Fig. 4.14, we observe that the particles stay close to the axis, following the helical core. Thus, we find that there is a strong effect of the helical core amplitude on the inward pinch faced by impurity particles, arising implicitly through the associated neoclassical effects.

We again consider the analytical radial flux expression for impurities Eq. 2.161. Strictly speaking, Eq. 2.161 is only valid for axisymmetry, however it contains an explicit dependence on the relation of the fluxes to the background ion poloidal flow $U_{1\theta,i}$, and therefore it is instructive to study the same expression using the background poloidal flow $U_{1\theta,i}$ obtained for the helical core to see its explicit effect on the saturation density peaking. Firstly, as we know from Eq. 2.161, toroidal rotation enhances the diffusivity by a factor of $(1 + \mathcal{M}_*^2)^2$, which enhances the rate of peaking for plasma rotation. This enhanced diffusivity is in accordance with our observation of the saturation times of the peaked impurity density, reducing from about $t \sim 2s$ for the non-rotating case to $t \sim 15ms$ for 20kHz rotation. We notice from the second term on the RHS of Eq. 2.161 that the inward impurity flux gets further modulated by a factor of $\langle U_{1\theta,i} \rangle$, in addition to the centrifugal enhancement. This averaged poloidal velocity is a purely geometric effect, and scales in the same manner as the parallel velocity $U_{\parallel,i}$, seen in Fig. 4.6. One can notice that $\langle U_{1\theta,i} \rangle \approx 0$ in the axisymmetric limit, as is expected from conventional neoclassical literature [Helander and Sigmar, 2005, Shaing et al., 2015], but

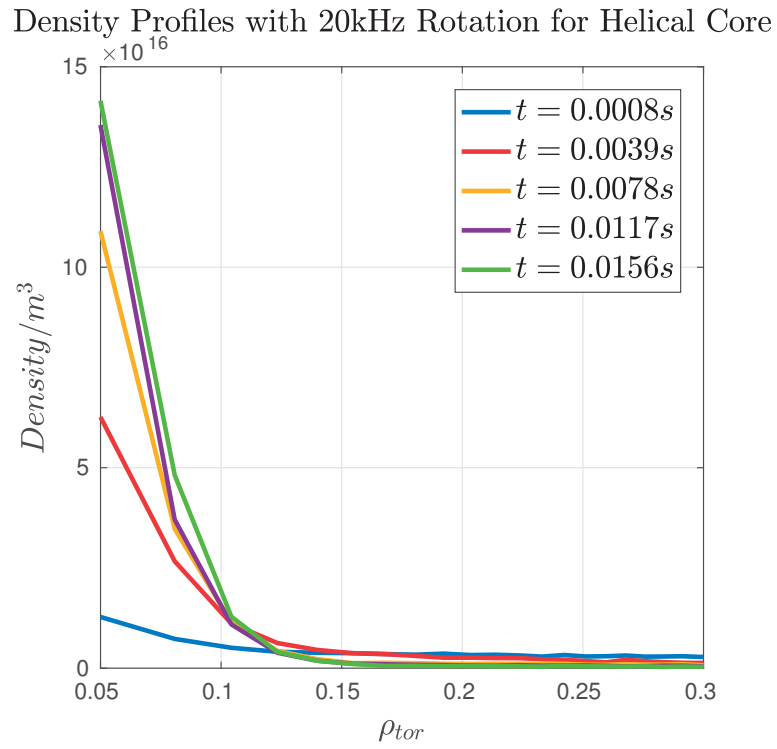


Figure 4.13 – The plots of the density profile for a helical core equilibrium with 20kHz rotation (zoomed in from $s = 0.05 - 0.3$).

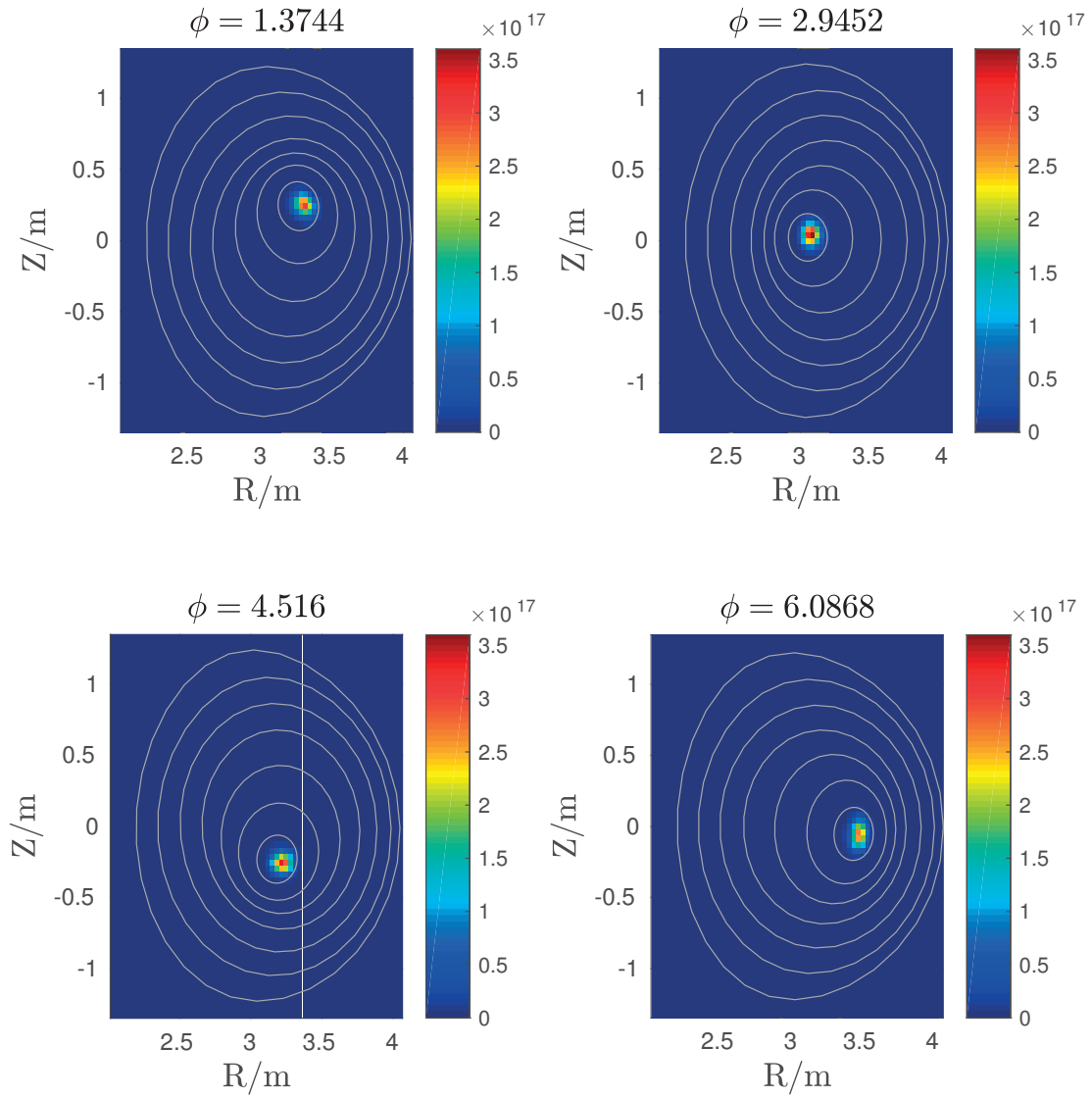


Figure 4.14 – Plots of density of tungsten on various toroidal cuts for a helical core case with 20kHz rotation, assuming a value of the geometrical factor G_b consistent with the equilibrium. One can notice that the impurities for this case are pinched much closer towards the axis, following the axis of the helical core.

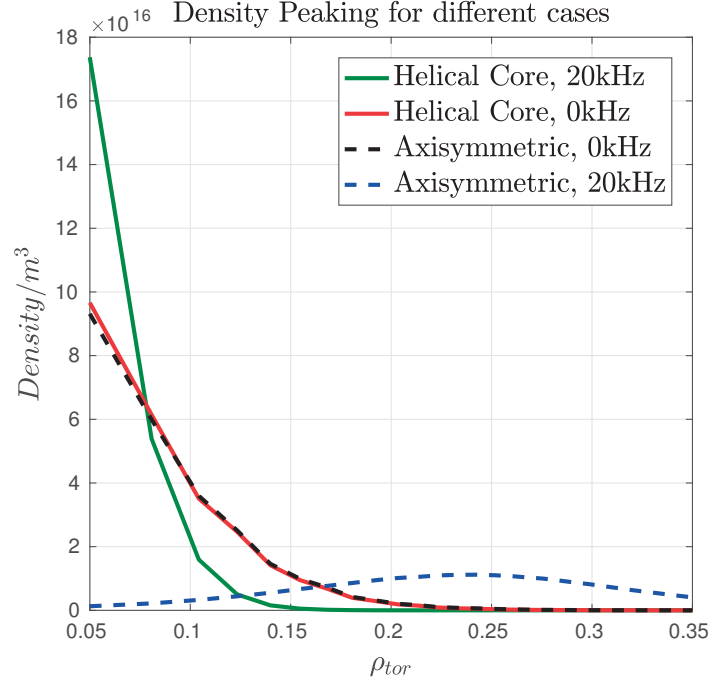


Figure 4.15 – Plot of intensity of density peaking for axisymmetry and helical core without flow and helical core with flow. The figure is zoomed to $\rho_{tor} = 0.35$ for convenience of comparison.

is enhanced by an order of magnitude for the helical core in the core region. Additionally, this geometrical enhancement only appears in the flux through a factor of $\mathcal{M}_*^2 / (1 + \mathcal{M}_*^2)$. If one neglects rotation, setting $\mathcal{M}_* = 0$, we find the density peaking to scale identically for the axisymmetric and helical core cases, irrespective of the geometry, which we recover in Fig. 4.15. Retaining \mathcal{M}_* and $\langle U_{1\theta,i} \rangle$, the saturated impurity density profile from Eq. 2.161 becomes as in Eq. 2.163

$$\begin{aligned} \frac{\langle n_W(r) \rangle}{\langle n_W(0) \rangle} &= \left(\frac{n_i(r)}{n_i(0)} \right)^{\xi Z_W / Z_i} \exp \left\{ \frac{\tilde{m}}{m_*} \frac{(3 + 2\mathcal{M}_*^2)\mathcal{M}_*^4}{(1 + \mathcal{M}_*^2)^2} \frac{r}{R_0} \right\}, \text{ where} \\ \xi &= \frac{Z_i e n_i}{p'} \left(1 - \frac{\mathcal{M}_*^2}{1 + \mathcal{M}_*^2} \langle U_{1\theta,i} \rangle \right). \end{aligned} \quad (4.6)$$

With the addition of plasma rotation, the augmentation of $\langle U_{1\theta,i} \rangle$ for the helical core leads to the strong peaking near the magnetic axis noticed earlier. In the rotating case, the saturated impurity density peaks near the axis as compared to off-axis in the axisymmetric case with rotation, as the inward pinch is enhanced by the non-zero poloidal flow for the helical core case. As also can be seen in Fig. 4.15, the peaking density for helical core is much higher with plasma rotation than for the cases without rotation, as expected. There is reasonably good agreement in the peaking density predicted by Eq. 2.163 and the obtained peaking as can be noticed in Fig. 4.16.

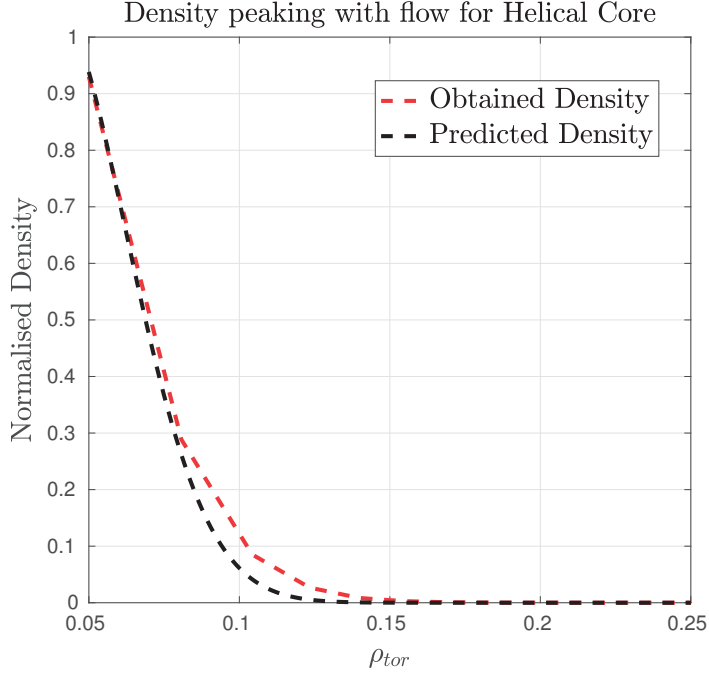


Figure 4.16 – Comparison of obtained density with density predicted from Eq. 2.163.

In order to verify the effects of presence of the poloidal flow, we increased the parallel flow $U_{1\parallel,i}$ for the axisymmetric case by a small amount, while making sure that the poloidal flow remains zero $U_{1\theta,i} = 0$. We still find a similar off-axis peaking as observed in the case of axisymmetry in the previous section. When we artificially increase the poloidal flow velocity $U_{1\theta,i}$ for axisymmetry from zero to a small finite value as in the helical core case, we observe a near-axis peaking again in the presence of finite poloidal flows with strong toroidal flow. Thus, the peaking in the helical core seems to be an effect arising from the presence of a finite poloidal velocity $U_{1\theta,i}$, due to pressure-gradient effects and strong toroidal flows. Finite poloidal flows are only geometrically possible in presence of large 3D effects such as the 1/1 saturated internal kink.

4.5 Conclusions

In this chapter, we have described the results obtained from the simulations of neoclassical transport of trace heavy impurities using a PIC-based approach. We considered ideal MHD equilibria computed with VMEC for kinked and unkinked plasmas pertaining to JET-like hybrid scenarios. In order to perform the particle-orbit following, we used the guiding-centre code VENUS-LEVIS with added modifications for plasma flow and also include the neoclassical friction force through a Monte-Carlo collision operator. The inward flux from neoclassical friction force depends on the flow velocity of the background ions, and we find that it has a strong dependence on the poloidal velocity $\langle U_{1\theta,i} \rangle$, which depends solely on the magnetic

geometry of the equilibrium.

We first benchmarked for an axisymmetric case without rotation and observed that the impurity density peaking does indeed satisfy the theoretically predicted scaling as expected from well-known neoclassical literature [Hinton and Hazeltine, 1976, Helander and Sigmar, 2005]. On doing another axisymmetric case including rotation but without neoclassical effects, we find that the outward diffusivity increase also follows the predicted scaling from the neoclassical transport of impurity species with rotation, which is similar to known results [McClements and McKay, 2009, Romanelli et al., 2011]. Having established the benchmarking of the tungsten behaviour with and without rotation, we proceed to perform simulations of tungsten transport with realistic account of the parallel flow velocity of the background ions. We find that the parallel velocity of the ions in the core region is much higher in a helical core than in axisymmetry, thus imparting an inward drift to the impurity particles, dragging them towards the axis. For the case of axisymmetry with rotation, the impurity particle densities saturate off-axis at the boundary of the core, as expected from neoclassical theory and as seen in [Casson et al., 2015]. We find that this is because of the centrifugal effects competing with the neoclassical inward pinch, where the centrifugal effects encourage a strong outward diffusion. For the strong helical core case, the inward flux is strongly enhanced by the augmented poloidal velocity $U_{\theta,j}$ of the background ions near the magnetic axis, thereby strongly increasing the impurity peaking, which has been experimentally seen with helical-core presence [Sertoli et al., 2015a, Sertoli et al., 2015b] but not previously explained before. This has been shown to occur very quickly (30ms) if the Tungsten Mach number is high, but slowly (2s) if rotation is ignored. In the absence of rotation, helical cores and their associated pressure-gradient driven flows do not introduce any additional inward transport. We thus conclude that the helical core geometry and toroidal rotation are key to the dominating inward pinch of impurities with 1/1 continuous modes in JET-like hybrid operation scenarios.

The neoclassical contribution becomes smaller and smaller as the helical core weakens to approach axisymmetry. Thus, by controlling and reducing the strength of the helical core, it is possible for the centrifugal outward advection to compete strongly with the inward neoclassical friction force, pushing the impurities further away from the magnetic axis. And given the larger trapped fractions for the helical core, the centrifugal effects will also be enhanced leading to a more efficient expulsion of impurities away from the magnetic axis. This could be very useful for impurity control in JET hybrid-scenario beam-injected plasmas.

5 Outlook and Future Work

In this chapter, we consider avenues to continue the work in the thesis. The ideas presented here either rely on extending some work within the assumptions made in the thesis, or in generalizing certain ideas in order to overcome the assumptions and extend its area of validity.

5.1 Exploring the Impurity Screening Effects of Temperature Gradients

We have neglected the effect of temperature gradients throughout the thesis in order to focus solely on geometrical effects, neglecting the additional complication produced by thermal transport. In the presence of temperature gradients, the impurities face temperature gradient shielding which offers an outward flux. Furthermore, the poloidal flow is non-zero with finite temperature gradients and is significantly different in different regimes of collisionality, changing sign while transitioning from the banana regime to the Pfirsch-Schlüter regime. This implies a significant effect on the axisymmetric plasmas with temperature gradients and flows[Belli et al., 2014a], and may also imply a similar effect for the case with the 1/1 internal kink. This is certainly worth exploring as a more realistic and less pessimistic extension of the work presented in the thesis.

5.2 More Accurate Computation of Higher-Order Potential Φ_1 and 3D Flows

In the current thesis, we assumed that the higher-order quasi-neutrality restoring potential Φ_1 calculated assuming axisymmetric flows is valid for 3D geometries as well. However, in general, the leading-order flow in 3D fields is not purely toroidal and possesses a finite poloidal flow as well. Once the flows in 3D magnetic fields are obtained accurately, it is possible to use the constraints Eqs. (2.50)-(2.54) to solve for the higher-order potential Φ_1 . This requires a neoclassical solver that is able to solve the set of equations along the field line in 3D, which

requires coding an additional module to the existing neoclassical solver that calculates the parallel flows.

5.3 Extension into Different Collisional Regimes

So far, this thesis limits itself to the collisionless banana regime for calculation of the bootstrap currents and the Pfirsch-Schlüter regime for computing impurity transport. In the $\sqrt{\nu}$ -regime, though the neoclassical formulae for the plasma flows are available [Shaing and Callen, 1983], it is difficult to perform the impurity transport calculations because we are not aware of how much of a deviation from a Maxwellian the background ion distribution undergoes. Furthermore, in case of 3D, the higher-order potential Φ_1 may play an important role in the background and impurity fluxes in the banana regime shown in recent studies [Helander et al., 2017]. To improve on the modeling in the banana regime, it is imperative to have a collision operator and a PIC scheme that faithfully takes into account the changing form of the background distribution, and it may also be important to know the exact form of Φ_1 for the 3D equilibrium, at least where the impurity densities can no longer be considered trace.

The implementation for the calculation of bootstrap current and parallel flows for the plateau regime (with moderate collisionality) is more involved computationally [Shaing et al., 1989, Shaing et al., 1986b], but could constitute a self-consistent project. That the helical core presents an augmentation of the bootstrap current or the parallel flow is still expected to hold true.

In the Pfirsch-Schlüter regime, the bootstrap current is virtually zero for 2D and 3D and does not need to be evaluated [Shaing et al., 2015].

5.4 Extending the Scope of the MHD equilibrium

With strong 3D flows, it is necessary to formulate a variational model for ideal 3D MHD with fully 3D flows. Currently, the model for an 3D MHD equilibrium with purely toroidal flows relies on severely constraining assumptions, and is only a valid model for axisymmetry as shown in Chapter 2. It may be prudent to generalize the association between the variational ideal MHD model and the ideal MHD equation model, for example with a Hamiltonian approach as in Ref. [Andreussi et al., 2010], for fully toroidal flows in order to eventually develop an equilibrium solver which can generate numerically accurate 3D MHD equilibria with fully 3D flows. Strong flows may however force the equilibrium to constrain itself to axisymmetry [Sugama et al., 2011, Helander, 2014].

5.5 Modeling of Experiments in JET

Once all the previous factors are accounted for, it would be pertinent to perform a comparison with JET cases where continuous modes are observed. This would require searching through the JET pulse archive to search for shots with an acceptable range of physical parameters which lie within the approximations of our model. It would also require a synthetic Soft X-Ray (SXR) diagnostic in VENUS-LEVIS, similar to Ref. [Pütterich et al., 2008], in order to visually compare what is observed by the actual SXR cameras installed in JET. This will require close collaboration with the maintainers of the SXR diagnostic. The modeling and comparison would be the logical culmination of this nature of work.

6 Summary and Conclusions

6.1 Summary of the Thesis

We use this chapter as an opportunity to summarize the salient points of the thesis. In this thesis, we have considered certain neoclassical phenomena in 2D and 3D magnetic geometries using accurate numerical representations of the equilibria from VMEC.

In chapter 2, we collected together all the relevant physics that explores the use of 3D fields and neoclassical effects. The chapter involves the exploration of the limitations of the 3D MHD model with toroidal flow, the nature of the plasma flows and bootstrap current for 3D geometries, and impurity behaviour in the presence of friction offered by the background flow. In outlining the limitations, we find there to be at least two neoclassical phenomena that are amenable to use with 3D equilibria obtained numerically: solution of parallel flows and bootstrap currents in various collisional regimes.

We observed that the use of 3D equilibria with certain 3D magnetic effects like RMPs and Toroidal Ripple often obscured relevant physical effects because of the presence of current sheets in the relevant region of the equilibria. This was the conclusion derived from the first part of Chapter 3. In the second part of Chapter 3, we proceeded to build a case for the 1/1 saturated internal kink as a prime candidate for studying neoclassical effects. On careful choice of the helical core with a q -profile such that it avoided the $q = 1$ resonance in the helical region, we found an augmentation of the bootstrap current in the helical core region which was not observed for the axisymmetric case. This work was published in 2016[Raghunathan et al., 2016]. We expected a similar augmentation of the parallel background ion flows in the helical core region.

In Chapter 4, having now confirmed that the parallel flows for a 1/1 internal kink in the helical-core region can be obtained without any serious numerical resonances, we proceeded to perform guiding-center simulations for heavy impurity particles facing neoclassical friction force due to the background ion flow. We first benchmarked and observed very good agreement with well-known neoclassical results in axisymmetry without flows. Then we

Chapter 6. Summary and Conclusions

used some recent results developed from Ref. [Romanelli and Ottaviani, 1998] to benchmark heavy impurity behaviour in the case of axisymmetry with flow, resulting in off-axis peaking of impurities. This off-axis peaking was also found to agree well with known neoclassical results incorporating axisymmetric rotation. Having made sure that our model reproduces known results from the neoclassical theory, we proceeded to simulate heavy impurity particles in a saturated 1/1 internal kink with flow. For this case, we observed that the helical core, because of the presence of finite background poloidal flow, causes the impurity particles to peak near-axis again. Therefore, we conclude that the presence of an ideal helical core leads to impurity accumulation in the core region, at least in the absence of temperature gradients. This work was recently published [Raghunathan et al., 2017].

In Chapter 5, we delineate possible avenues to expand the work of the thesis along the lines of overcoming the limitations posed by the assumptions in the various models used.

6.2 Final Words

This thesis explored topics bridging various physical themes together such as ideal MHD equilibrium theory, guiding-center physics and neoclassical physics with an overarching use of computational techniques. The thesis has presented results obtained by considering valid and viable domains under which these various themes overlap and has presented various avenues to extend the work and generalize it. It is hoped that the thesis can be used as a clear starting point for further exploration of relevant issues in 3D tokamak physics.

Bibliography

- [Ahn et al., 2016] Ahn, J.-H., Garbet, X., Lütjens, H., and Guirlet, R. (2016). Dynamics of heavy impurities in non-linear mhd simulations of sawtooth tokamak plasmas. *Plasma Physics and Controlled Fusion*, 58(12):125009.
- [Anderson et al., 1990] Anderson, D., Cooper, W., Gruber, R., Merazzi, S., and Schwenn, U. (1990). Methods for the efficient calculation of the (mhd) magnetohydrodynamic stability properties of magnetically confined fusion plasmas. *The International Journal of Supercomputing Applications*, 4(3):34–47.
- [Andreussi et al., 2010] Andreussi, T., Morrison, P. J., and Pegoraro, F. (2010). Mhd equilibrium variational principles with symmetry. *Plasma Physics and Controlled Fusion*, 52(5):055001.
- [Angioni and Helander, 2014] Angioni, C. and Helander, P. (2014). Neoclassical transport of heavy impurities with poloidally asymmetric density distribution in tokamaks. *Plasma Physics and Controlled Fusion*, 56(12):124001.
- [Belli et al., 2014a] Belli, E. A., Candy, J., and Angioni, C. (2014a). Pfirsch–schlüter neoclassical heavy impurity transport in a rotating plasma. *Plasma Physics and Controlled Fusion*, 56(12):124002.
- [Belli et al., 2014b] Belli, E. A., Candy, J., Meneghini, O., and Osborne, T. H. (2014b). Limitations of bootstrap current models. *Plasma Physics and Controlled Fusion*, 56(4):045006.
- [Boozer, 1981] Boozer, A. H. (1981). Plasma equilibrium with rational magnetic surfaces. *The Physics of Fluids*, 24(11):1999–2003.
- [Brizard, 1995] Brizard, A. J. (1995). Nonlinear gyrokinetic vlasov equation for toroidally rotating axisymmetric tokamaks. *Physics of Plasmas*, 2(2):459–471.
- [Brunetti et al., 2014] Brunetti, D., Graves, J., Cooper, W., and Terranova, D. (2014). Ideal saturated mhd helical structures in axisymmetric hybrid plasmas. *Nuclear Fusion*, 54(6):064017.
- [Cary and Brizard, 2009] Cary, J. R. and Brizard, A. J. (2009). Hamiltonian theory of guiding-center motion. *Reviews of Modern Physics*, 81:693–738.

Bibliography

- [Casson et al., 2015] Casson, F. J., Angioni, C., Belli, E. A., Bilato, R., Mantica, P., Odstrcil, T., Pütterich, T., Valisa, M., Garzotti, L., Giroud, C., Hobirk, J., Maggi, C. F., Mlynar, J., and Reinke, M. L. (2015). Theoretical description of heavy impurity transport and its application to the modelling of tungsten in jet and asdex upgrade. *Plasma Physics and Controlled Fusion*, 57(1):014031.
- [Chapman et al., 2014] Chapman, I., Brunetti, D., Buratti, P., Cooper, W., Graves, J., Harrison, J., Holgate, J., Jardin, S., Sabbagh, S., Tritz, K., the MAST Teams, N., and Contributors, E.-J. (2014). Three-dimensional distortions of the tokamak plasma boundary: boundary displacements in the presence of saturated mhd instabilities. *Nuclear Fusion*, 54(8):083007.
- [Chapman et al., 2010] Chapman, I., Hua, M.-D., Pinches, S., Akers, R., Field, A., Graves, J., Hastie, R., Michael, C., and the MAST Team (2010). Saturated ideal modes in advanced tokamak regimes in mast. *Nuclear Fusion*, 50(4):045007.
- [Coda et al., 2007] Coda, S., Sauter, O., Henderson, M. A., Goodman, T. P., and the TCV Team (2007). Steady-state, fully bootstrap-sustained discharges in the tcv tokamak. volume 31, page 2230. EPS.
- [Cooper et al., 2015] Cooper, W., Brunetti, D., Faustin, J., Graves, J., Pfefferlé, D., Raghunathan, M., Sauter, O., Tran, T., Chapman, I., Ham, C., Aiba, N., team, T. M., and contributors, J. (2015). Free boundary equilibrium in 3d tokamaks with toroidal rotation. *Nuclear Fusion*, 55(6):063032.
- [Cooper, 1992] Cooper, W. A. (1992). Variational formulation of the linear mhd stability of 3d plasmas with noninteracting hot electrons. *Plasma Physics and Controlled Fusion*, 34(6):1011.
- [Cooper et al., 2010] Cooper, W. A., Graves, J. P., Pochelon, A., Sauter, O., and Villard, L. (2010). Tokamak magnetohydrodynamic equilibrium states with axisymmetric boundary and a 3d helical core. *Physical Review Letters*, 105:035003.
- [Cooper et al., 2014] Cooper, W. A., Hirshman, S. P., Chapman, I. T., Brunetti, D., Faustin, J. M., Graves, J. P., Pfefferlé, D., Raghunathan, M., Sauter, O., Tran, T. M., and Aiba, N. (2014). An approximate single fluid 3-dimensional magnetohydrodynamic equilibrium model with toroidal flow. *Plasma Physics and Controlled Fusion*, 56(9):094004.
- [Cooper et al., 2004] Cooper, W. A., Margalet, S. F. i., Allfrey, S. J., Kißlinger, J., Wobig, H. F., Narushima, Y., Okamura, S., Suzuki, C., Watanabe, K. Y., Yamazaki, K., et al. (2004). Magnetohydrodynamic stability of free-boundary quasi-axisymmetric stellarator equilibria with finite bootstrap current. *Fusion Science and Technology*, 46(2):365–377.
- [Fülöp and Helander, 1999] Fülöp, T. and Helander, P. (1999). Nonlinear neoclassical transport in a rotating impure plasma with large gradients. *Physics of Plasmas*, 6(8):3066–3075.

- [Graves et al., 2000] Graves, J. P., Hastie, R. J., and Hopcraft, K. I. (2000). The effects of sheared toroidal plasma rotation on the internal kink mode in the banana regime. *Plasma Physics and Controlled Fusion*, 42(10):1049.
- [Helander, 2014] Helander, P. (2014). Theory of plasma confinement in non-axisymmetric magnetic fields. *Reports on Progress in Physics*, 77(8):087001.
- [Helander et al., 2017] Helander, P., Newton, S. L., Mollén, A., and Smith, H. M. (2017). Impurity transport in a mixed-collisionality stellarator plasma. *Physical Review Letters*, 118:155002.
- [Helander and Sigmar, 2005] Helander, P. and Sigmar, D. J. (2005). *Collisional transport in magnetized plasmas*, volume 4. Cambridge University Press.
- [Hender et al., 2016] Hender, T., Buratti, P., Casson, F., Alper, B., Baranov, Y. F., Baruzzo, M., Challis, C., Koechl, F., Lawson, K., Marchetto, C., Nave, M., Pütterich, T., Cortes, S. R., and Contributors, J. (2016). The role of mhd in causing impurity peaking in jet hybrid plasmas. *Nuclear Fusion*, 56(6):066002.
- [Hinton and Hazeltine, 1976] Hinton, F. L. and Hazeltine, R. D. (1976). Theory of plasma transport in toroidal confinement systems. *Reviews of Modern Physics*, 48:239–308.
- [Hirshman et al., 1986] Hirshman, S., van RIJ, W., and Merkel, P. (1986). Three-dimensional free boundary calculations using a spectral green’s function method. *Computer Physics Communications*, 43(1):143 – 155.
- [Hirshman and Whitson, 1983] Hirshman, S. P. and Whitson, J. C. (1983). Steepest-descent moment method for three-dimensional magnetohydrodynamic equilibria. *The Physics of Fluids*, 26(12):3553–3568.
- [Huba, 2004] Huba, J. D. (2004). Nrl: Plasma formulary. Technical report, Naval Research Laboratory, Beam Physics Branch.
- [Isaev et al., 2003] Isaev, M. Y., Cooper, W., Watanabe, K., and Nakajima, N. (2003). Spbsc-terpsichore bootstrap current benchmark for the low collisionality regime. In *Proc. 30th EPS Conf. on Controlled Fusion and Plasma Phys.(St Petersburg, Russia, 2003)*.
- [Johnson et al., 1999] Johnson, J. L., Ichiguchi, K., Nakamura, Y., Okamoto, M., Wakatani, M., and Nakajima, N. (1999). External kink modes in a large helical device (lhd) equilibrium with self-consistent bootstrap current. *Physics of Plasmas*, 6(6):2513–2522.
- [Landreman et al., 2015] Landreman, M., Smith, H., Mollén, A., and Helander, P. (2015). Sfincs: A flexible tool for advanced stellarator neoclassical computations. In *20th International Stellarator-Heliotron Workshop (ISHW)*.
- [Littlejohn, 1983] Littlejohn, R. G. (1983). Variational principles of guiding centre motion. *Journal of Plasma Physics*, 29(1):111–125.

Bibliography

- [Maschke and Perrin, 1980] Maschke, E. K. and Perrin, H. (1980). Exact solutions of the stationary mhd equations for a rotating toroidal plasma. *Plasma Physics*, 22(6):579.
- [McClements and McKay, 2009] McClements, K. G. and McKay, R. J. (2009). The orbital dynamics and collisional transport of trace massive impurity ions in rotating tokamaks. *Plasma Physics and Controlled Fusion*, 51(11):115009.
- [McKay et al., 2008] McKay, R. J., McClements, K. G., Thyagaraja, A., and Fletcher, L. (2008). Test-particle simulations of collisional impurity transport in rotating spherical tokamak plasmas. *Plasma Physics and Controlled Fusion*, 50(6):065017.
- [Mollén et al., 2014] Mollén, A., Landreman, M., and Smith, H. M. (2014). On collisional impurity transport in nonaxisymmetric plasmas. *Journal of Physics: Conference Series*, 561(1):012012.
- [Nakajima and Okamoto, 1992] Nakajima, N. and Okamoto, M. (1992). Neoclassical flow, current, and rotation in general toroidal systems. *Journal of the Physical Society of Japan*, 61(3):833–843.
- [Peeters et al., 2009] Peeters, A. G., Srintzi, D., Camenen, Y., Angioni, C., Casson, F. J., Hornsby, W. A., and Snodin, A. P. (2009). Influence of the centrifugal force and parallel dynamics on the toroidal momentum transport due to small scale turbulence in a tokamak. *Physics of Plasmas*, 16(4):042310.
- [Pfefferlé, 2015] Pfefferlé, D. (2015). *Energetic Ion Dynamics and Confinement in 3D Saturated MHD Configurations*. PhD thesis, École Polytechnique Fédérale de Lausanne, Lausanne, Switzerland.
- [Pfefferlé et al., 2014a] Pfefferlé, D., Cooper, W., Graves, J., and Misev, C. (2014a). Venus-levis and its spline-fourier interpolation of 3d toroidal magnetic field representation for guiding-centre and full-orbit simulations of charged energetic particles. *Computer Physics Communications*, 185(12):3127 – 3140.
- [Pfefferlé et al., 2014b] Pfefferlé, D., Graves, J., Cooper, W., Misev, C., Chapman, I., Turnyan-skiy, M., and Sangaroon, S. (2014b). Nbi fast ion confinement in the helical core of mast hybrid-like plasmas. *Nuclear Fusion*, 54(6):064020.
- [Pütterich et al., 2010] Pütterich, T., Neu, R., Dux, R., Whiteford, A., O’Mullane, M., Summers, H., and the ASDEX Upgrade Team (2010). Calculation and experimental test of the cooling factor of tungsten. *Nuclear Fusion*, 50(2):025012.
- [Pütterich et al., 2008] Pütterich, T., Neu, R., Dux, R., Whiteford, A. D., O’Mullane, M. G., and the ASDEX Upgrade Team (2008). Modelling of measured tungsten spectra from asdex upgrade and predictions for iter. *Plasma Physics and Controlled Fusion*, 50(8):085016.
- [Raghunathan et al., 2016] Raghunathan, M., Graves, J., Cooper, W., Pedro, M., and Sauter, O. (2016). Simulation of bootstrap current in 2d and 3d ideal magnetic fields in tokamaks. *Nuclear Fusion*, 56(9):092004.

-
- [Raghunathan et al., 2017] Raghunathan, M., Graves, J. P., Nicolas, T., Cooper, W. A., Garbet, X., and Pfefferle, D. (2017). Heavy impurity confinement in hybrid operation scenario plasmas with a rotating 1/1 continuous mode. *Plasma Physics and Controlled Fusion*.
- [Romanelli, 1998] Romanelli, M. (1998). *Study of high-Z impurity accumulation and transport in the JET Tokamak plasmas from soft X-ray tomography*. PhD thesis, University of London, Imperial College of Science, Technology and Medicine.
- [Romanelli et al., 2011] Romanelli, M., McClements, K. G., Cross, J., Knight, P. J., Thyagaraja, A., and Callaghan, J. (2011). Full orbit simulation of collisional transport of impurity ions in the mast spherical tokamak. *Plasma Physics and Controlled Fusion*, 53(5):054017.
- [Romanelli and Ottaviani, 1998] Romanelli, M. and Ottaviani, M. (1998). Effects of density asymmetries on heavy impurity transport in a rotating tokamak plasma. *Plasma Physics and Controlled Fusion*, 40(10):1767.
- [Rutherford, 1974] Rutherford, P. H. (1974). Impurity transport in the pfirsch-schlüter regime. *The Physics of Fluids*, 17(9):1782–1784.
- [Sauter, 2016] Sauter, O. (2016). Geometric formulas for system codes including the effect of negative triangularity. *Fusion Engineering and Design*, 112:633 – 645.
- [Sauter et al., 1999] Sauter, O., Angioni, C., and Lin-Liu, Y. R. (1999). Neoclassical conductivity and bootstrap current formulas for general axisymmetric equilibria and arbitrary collisionality regime. *Physics of Plasmas*, 6(7):2834–2839.
- [Sertoli et al., 2015a] Sertoli, M., Dux, R., Pütterich, T., and the ASDEX Upgrade Team (2015a). Modification of impurity transport in the presence of saturated (m,n)=(1,1) mhd activity at asdex upgrade. *Plasma Physics and Controlled Fusion*, 57(7):075004.
- [Sertoli et al., 2015b] Sertoli, M., Odstrcil, T., Angioni, C., and the ASDEX Upgrade Team (2015b). Interplay between central ecrh and saturated (m,n)=(1,1) mhd activity in mitigating tungsten accumulation at asdex upgrade. *Nuclear Fusion*, 55(11):113029.
- [Shaing et al., 2015] Shaing, K., Ida, K., and Sabbagh, S. (2015). Neoclassical plasma viscosity and transport processes in non-axisymmetric tori. *Nuclear Fusion*, 55(12):125001.
- [Shaing and Callen, 1983] Shaing, K. C. and Callen, J. D. (1983). Neoclassical flows and transport in nonaxisymmetric toroidal plasmas. *The Physics of Fluids*, 26(11):3315–3326.
- [Shaing et al., 1986a] Shaing, K. C., Hirshman, S. P., and Callen, J. D. (1986a). Neoclassical transport fluxes in the plateau regime in nonaxisymmetric toroidal plasmas. *The Physics of Fluids*, 29(2):521–526.
- [Shaing et al., 1986b] Shaing, K. C., Hirshman, S. P., and Tolliver, J. S. (1986b). Parallel viscosity-driven neoclassical fluxes in the banana regime in nonsymmetric toroidal plasmas. *The Physics of Fluids*, 29(8):2548–2555.

Bibliography

- [Shaing et al., 1989] Shaing, K. C., Jr., E. C. C., Tolliver, J. S., Hirshman, S. P., and van Rij, W. I. (1989). Bootstrap current and parallel viscosity in the low collisionality regime in toroidal plasmas. *Physics of Fluids B: Plasma Physics*, 1(1):148–152.
- [Spitzer, 1958] Spitzer, L. J. (1958). The stellarator concept. *The Physics of Fluids*, 1(4):253–264.
- [Sugama et al., 2011] Sugama, H., Watanabe, T. H., Nunami, M., and Nishimura, S. (2011). Momentum balance and radial electric fields in axisymmetric and nonaxisymmetric toroidal plasmas. *Plasma Physics and Controlled Fusion*, 53(2):024004.
- [Turnbull et al., 2011] Turnbull, A., Cooper, W., Lao, L., and Ku, L.-P. (2011). Ideal mhd spectrum calculations for the aries-cs configuration. *Nuclear Fusion*, 51(12):123011.
- [Ware, 1970] Ware, A. A. (1970). Pinch effect for trapped particles in a tokamak. *Physical Review Letters*, 25:15–17.
- [Watanabe et al., 1992] Watanabe, K., Nakajima, N., Okamoto, M., Nakamura, Y., and Wakatani, M. (1992). Three-dimensional mhd equilibrium in the presence of bootstrap current for the large helical device. *Nuclear Fusion*, 32(9):1499.
- [Watanabe et al., 1995] Watanabe, K., Nakajima, N., Okamoto, M., Yamazaki, K., Nakamura, Y., and Wakatani, M. (1995). Effect of collisionality and radial electric field on bootstrap current in the large helical device. *Nuclear Fusion*, 35(3):335.
- [Wesson and Campbell, 2011] Wesson, J. and Campbell, D. J. (2011). *Tokamaks*, volume 149. Oxford University Press.
- [Wikipedia, 2017] Wikipedia (2017). Fusion power – wikipedia, the free encyclopedia.
- [Wingen et al., 2015] Wingen, A., Ferraro, N. M., Shafer, M. W., Unterberg, E. A., Canik, J. M., Evans, T. E., Hillis, D. L., Hirshman, S. P., Seal, S. K., Snyder, P. B., and Sontag, A. C. (2015). Connection between plasma response and resonant magnetic perturbation (rmp) edge localized mode (elm) suppression in diii-d. *Plasma Physics and Controlled Fusion*, 57(10):104006.
- [Wong and Cheng, 1987] Wong, K. L. and Cheng, C. Z. (1987). Neoclassical diffusion of heavy impurities in a rotating tokamak plasma. *Physical Review Letters*, 59:2643–2646.
- [Wong and Cheng, 1989] Wong, K. L. and Cheng, C. Z. (1989). Orbit effects on impurity transport in a rotating tokamak plasma. *Physics of Fluids B: Plasma Physics*, 1(3):545–554.

Acknowledgments

The classic line to begin these long orations often starts off with the question of how one can even begin composing these things. For me, of course, that's not the case. I wouldn't have been able to go through with my PhD without my parents. They've always been here when I needed them. And my brother, Ajay, for showing me how much one person can grow and develop even in a small amount of time.

And in my professional life, I would like to thank Jon and Tony, my advisors. They've been good to me beyond the usual need. I must also mention Olivier as his kindness got me through some trying times. Among my colleagues I'd like to thank in particular Jonathan and Timothée. They've saved me days, even months, of headache over the coding and physics.

Acknowledging the things that constitute me, I'd like to thank pizza. Pizzas consist of three components chiefly: the dough, the tomato sauce and the cheese. As for the dough, the best pizzas use a mature, but fresh sourdough to start leavening the dough, then allow it to proof for several days. On forming the pizza, use your knuckles softly to keep the air inside the dough, and push the gas pockets into the edges to puff them while simultaneously trying to get as thin a centre as possible. The tomato that goes into the sauce is of the chief importance in the sauce itself. The tomato must be sweet and tart by itself without needing the addition of vinegar or sugars. Usually San Marzano (DOP), Pellini and several other cultivars satisfy this requirement very well. You would want to mash this sauce coarsely, as some small pieces of tomato will end up giving a texture to the sauce and the pizza as a whole. The cheese is a tricky question. Usually fresh *fior di latte* is necessary for a proper Neapolitan pizza. Feel free to experiment with stringy-type cheeses of varying hardness, including Mozzarella, Provolone, Scarmoza. Do keep in mind that the softer the cheese, the more liquid it will drain on the pizza, and compensate with an appropriate density of the sauce. I'd like to thank Peter, Vera and others over at NYC Slice Pizza Lausanne. Several evenings were spent there.

A second constituent of mine is beer. Beer fundamentally consists of three ingredients and two workers. They are Water, Malt and Hops, and You and the Yeast, respectively. The water needs to be at least drinkable to make beer. It can be fine-tuned as per the nature of the beer. The malt is the main source of food for the yeast, and is capable of transforming its starches into sugars under the right conditions. The hops form the chief flavouring the beer. If the yeast wasn't involved, the beer would solely taste of the malt sugars and the hop flavours.

Acknowledgments

Our job as brewers is to get the combination that's just right for us and them, the yeasts. The yeast is the second participant in the work-force of the beer. It eats the sugars and the hop constituents and converts them into an extensive assay of tastes and flavours; Alcohol is merely a by-product of yeast. Unfortunately, presently there are very few methods of obtaining the same flavour profile without producing ethanol in such quantities. This might change significantly in the years to come, with immobilized yeast bio-reactor research picking up steam in the recent years. To all the folks whom I got to know through beer, especially Siméon, Rabei and others at the π -bar.

Food and beer only go so far. These four years wouldn't have been worth spending it not for the people at SPC. In chronological order, I'd like to express my gratitude to Himank and Isha, Daniele, Claudio, Gabriele, Matteo, Jordi, Andy and Patricia, Antoine, Farah, Anna, Roger, Hamish, Chantal, Sam and Dahye, Jéréemie, Matteo and Marta, Mengdi, Eduardo and many more. Thanks in particular to Jéréemie and Andy for translating the thesis abstract into French and German as well.

Outside of the SPC but still in EPFL, there's many a soul I must mention. Some names are Anna, Filip, Sunil, Chiara and some others. And outside of EPFL, I must first thank Laura for teaching me how to walk through life as a PhD student. Then to many others who I met and formed strong friendships with along the way: Mila, David, Stefanie, Linda, Romaric, Dmitri, Corey, Joëlla, etc. They were often the first to safety-test my beers. And as always to old friends like Sahaj, Anees, Anirban, Amartya, Noaman and others...

Madhusudan Raghunathan

Avenue d'Echallens 36, CH-1004 Lausanne • +41787155011 • r.madhu.1@gmail.com



Vitals

DOB: 11-09-1990

Nationality: Indian

Marital Status: Single

Online CV

linkedin.com/in/
madhusudan-
raghunathan

Languages

Trilingual in English,
Tamil, and Hindi.
Elementary French

Courses taken

Instructional Skills
Workshop, Teaching
Skills Toolkit

Programming

C, C++, Fortran
90/95/2003
Python,
R, Matlab, Octave
HTML, \LaTeX

Key Skills

Secondary and Undergraduate Level Teaching, Physics, Computational Sciences and General Science Education, Educational Coaching, Educational Counseling

Education

- 2013-present **Ph.D. Candidate (Cleared Thesis Defence)** SPC, EPFL, Lausanne, Switzerland
On theoretical modeling of plasma physics phenomena in the core of fusion reactors.
- 2008-2013 **BS/MS Dual Degreee** IISER, Pune, India
Majoried in Physics and minor in Chemistry with a focus on computational and statistical methods.
- Till 2008 **Senior Higher Secondary Certificate** KV (SAC), Ahmedabad, India
Higher secondary training in science stream.

Core Experience

- 2013-present **Ph.D. Researcher** SPC, EPFL, Lausanne, Switzerland
Research on of plasma physics phenomena in the core of fusion reactors towards obtaining a PhD.
- 2014-2015 **Project mentor for Master's Students** Lausanne CH
Mentored EPFL Master's students' projects for three semesters which involves individual coaching and guidance towards completing Plasma Physics projects.
- 2013-2017 **Teaching Assistant for courses Physique Numérique I and II** Lausanne CH
Teaching assistant with 490 hours of logged teaching work in numerical physics for 2nd year physics students in English and French at EPFL.
- July 2010 **Instructor Assistant for a Workshop on \LaTeX , Scilab and Octave** Pune, India
Workshop geared towards introducing college-level educators to mathematical softwares held at Bhaskaracharya Institute, Pune, India

Scientific Publications

- August 2017 **Heavy impurity confinement in hybrid operation scenario plasmas with a rotating 1/1 continuous mode** Journal Article
Raghunathan, M., Graves, J. P., Nicolas, T., Cooper, W. A., Garbet, X. and Pfefferlé, D., *Plasma Physics and Controlled Fusion* **59**, 124002 (2017).
- July 2016 **Simulation of bootstrap current in 2D and 3D ideal magnetic fields in tokamaks** Journal Article
Raghunathan, M., Graves, J. P., Cooper, W. A., Pedro, M. and Sauter, O., *Nuclear Fusion* **56**, 092004 (2016).
- February 2013 **Nonlinear Landau damping and formation of Bernstein-Greene-Kruskal structures for plasmas with q-nonextensive velocity distributions** Journal Article
Raghunathan, M. and Ganesh, R., *Physics of Plasmas* **20**, 032106 (2013).

Honours

- June 2017 **Invited talk at an IAEA meeting** Vienna, Austria
Invited talk at the IAEA Technical Meeting on Theory of Plasma Instabilities
- August 2009 **Delegate to Asian Science Camp** Tsukuba, Ibaraki, Japan
The Asian Science Camp is the equivalent of the Lindau Conference with Nobel Laureates and Dignitaries from Asian and Oceanic countries.

Scientific Experience

- 2012-2013 **Masters' project in IPR, Gandhinagar** Masters' Thesis
Development of a code for and Application of the 1D plasma kinetics model developed. Resulted in a publication in early 2013.
- 2010-2011 **Research Project in IPR, Gandhinagar** Summer Research Internship
Development of a computational framework for 1D plasma kinetics
- May 2009 **Advanced BSc Summer Camp, Gandhinagar, India** Summer Camp
A summer camp geared to get students acquainted with higher-level physics.

Scholarships

- 2008-2013 **KVPY Fellow, Young Scientists' Encouragement Scheme** IISc, India
A scheme to encourage students to pursue science as a career. Consists of a scholarship and an accompanying book grant.
- 2006-2008 **Physical Research Lab (PRL) Science Scholarship.** PRL, India
A science scholarship awarded through Year 11 and Year 12 of high school students by the Physical Research Laboratory (PRL), Ahmedabad, India.

Popular publications

Hobbies

Reading, SF Writing,
Contemporary Jazz
Music, South Indian
Cuisine,
Homebrewing,
Sensory beer analysis.

- September 2011 **Kalpa, IISER Pune, India** SF short story
Deus Ex Machina: A story about a computational simulation of a possible universe and how it consumes three scientists working on it
- June 2009 **Science Reporter, NISCAIR** SF short story
Survival: A science-fiction short story (about 10,000 words) about radiation dependent fungi wrecking havoc in a space-elevator system

